1997

Computational prediction of airfoil dynamic stall

Ekaterinaris, John A.

Elsevier

Progress in Aerospace Science, v.33, 1997, pp. 759-846.

Pergamon

Prog. Aerospace Sci. Vol. 33, pp. 759–846, 1997

0376–0421/97 $32.00

PII: S0376-0421(97)00012-2

COMPUTATIONAL PREDICTION OF AIRFOIL DYNAMIC STALL

John A. Ekaterinaris[a,*] and Max F. Platzer[b]

[a] *RISOE National Laboratory, The Test Station for Wind Turbines, 4000-Roskilde, Denmark*
[b] *Naval Postgraduate School, Department of Aeronautics and Astronautics, Monterey, CA 94943, U.S.A.*

Abstract—The term dynamic stall refers to unsteady flow separation occurring on aerodynamic bodies, such as airfoils and wings, which execute an unsteady motion. The prediction of dynamic stall is important for flight vehicle, turbomachinery, and wind turbine applications. Due to the complicated flow physics of the dynamic stall phenomenon the industry has been forced to use empirical methods for its prediction. However, recent progress in computational methods and the tremendous increase in computing power has made possible the use of the full fluid dynamic governing equations for dynamic stall investigation and prediction in the design process. It is the objective of this review to present the major approaches and results obtained in recent years and to point out existing deficiencies and possibilities for improvements. To this end, potential flow, boundary layer, viscous–inviscid interaction, and Navier–Stokes methods are described. The most commonly used numerical schemes for their solution are briefly described. Turbulence models used for the computation of high Reynolds number turbulent flows, which are of primary interest to industry, are presented. The impact of transition from laminar to turbulent flow on the dynamic stall phenomenon is discussed and currently available methods for its prediction are summarized. The main computational results obtained for airfoil and wing dynamic stall and comparisons with available experimental measurements are presented. The review concludes with a discussion of existing deficiencies and possibilities for future improvements. © 1998 Published by Elsevier Science Ltd.

CONTENTS

* Present address: NEAR Inc., 526 Clyde Avenue, Mountain View, CA 9403-2122, USA

NOTATION

α—angle of incidence
β—pseudo-compressibility parameter
Γ— airfoil circulation
γ_w—wake panel vorticity
γ_{tr}—intermittency function
Δt—time step
δ—boundary-layer thickness
δ^*—displacement thickness
θ—momentum thickness
μ_t—eddy viscosity
ν—kinematic viscosity
ξ, η, ζ—curvilinear coordinates
ρ = fluid density
τ = shear stress
Ψ—stream function
$\boldsymbol{\Omega}$—rotational speed
$\boldsymbol{\omega}$—vorticity vector
A, B—flux Jacobian matrices
a—speed of sound
c—chord length
e—internal energy
f, g—flux vectors
k—reduced frequency ($\omega c/2U_\infty$)
M—viscous flux Jacobian matrix
p—pressure
Q—solution variable vector
Re—Reynolds number
S— viscous flux
U_e—boundary-layer edge velocity
u, v, w—Cartesian velocity components
U, V, W—contravariant velocity components
x, y, z—Cartesian coordinates

1. INTRODUCTION

Dynamic airfoil stall involves unsteady separated flows which present the experimental and computational fluid dynamicist with particular challenges. Considerable advances have been achieved in experimental methods and measuring capabilities of these flows. As a result, more detailed measurements of unsteady flows have become possible. A review of recent experimental techniques and results of dynamic stall investigations have been presented by Carr and Chandrasekhara.[11]

Dynamic stall prediction methods used by the helicopter, turbomachinery, aircraft and wind turbine industries are largely based on empirical or semi-empirical approaches. The last comprehensive review of these methods was given by Ericsson and Reding[52] in 1987 in another volume of this series. However, a more detailed knowledge of the unsteady loads caused by dynamic airfoil or blade motions, including dynamic stall effects, is needed for dynamic response, aeroelastic stability and noise generation and propagation analyses.

Fortunately, in recent decades considerable progress has been made in the computation of complex, unsteady, attached and separated flows using potential flow, boundary layer, and viscous–inviscid interaction methods and, more recently, the Euler and full unsteady Navier–Stokes equations. This progress has been made possible by advances in computational methods, computing power and improved capability in modeling turbulent and transitional flows. Detailed accounts of computational methods can be found in books by Anderson *et al.*,[1] Hirsch[80] and Fletcher.[55] The state of the art in turbulence modeling for engineering flows can be found in the book by Wilcox[163] and the review articles of this series by Bradshaw[8] and Tulapurkara.[148] These methods have the advantage of clarifying

many physical flow aspects which remain inaccessible by semi-empirical methods. For example, inviscid methods allow the computation of pressure lag effects in unsteady attached flows and thereby provide an explanation of the observed delay in dynamic stall onset. Boundary-layer methods provide an efficient way to study the boundary-layer build up in attached flows. Viscous–inviscid interaction methods extend the efficiency of the direct boundary layer methods to cases where small regions of separated flow exist. Finally, the full Reynolds-averaged Navier–Stokes equations provide a method, albeit a computationally expensive and time consuming one, to investigate massively separated unsteady flows. The efficiency of these methods critically depends on the numerical method used for their solution and their accuracy is determined in many cases by the judicious choice of proper turbulence and transition models.

It is the objective of the present review to provide the reader with an appreciation for the progress achieved in predicting dynamic stall, to summarize the major methods and results, and to indicate deficiencies which require further research.

2. THE DYNAMIC STALL PHENOMENON

For example, during the forward or maneuvering flight of helicopters, the angle of attack of the rotor blade sections periodically changes and reaches large values as the blades rotate and pass through the so-called retreating blade position. In contrast to steady-state airfoil stall, on an airfoil whose incidence is increasing rapidly, the onset of the stall can be delayed to incidences which may exceed the static stall angle by a significant amount. However, once dynamic stall occurs, the aerodynamic loads are generally more severe compared to steady stall and may cause significant increases in the blade stresses and the control system loads. Therefore, dynamic stall limits the helicopter flight envelope and methods are required to predict its occurrence. Dynamic stall also occurs on horizontal axis wind turbines, where rather complex blade incidence variations are generated by the unsteady inflow conditions due to atmospheric turbulence and during operation in yaw. Dynamic stall also may be encountered on propeller and turbomachinery blades and on the wings of rapidly maneuvering fighter aircraft and missiles.

Numerous experiments have revealed the sequence of flow events depicted in Fig. 1 taken from Ref. (10). First, a vortex starts to develop near the airfoil leading edge as the angle of attack is rapidly increased past the static stall angle. This vortex then is convected downstream near the airfoil surface which causes an increase in lift due to the suction induced by the vortex. The magnitude of the lift increase depends on the strength of the vortex and its distance from the surface. The streamwise movement of the vortex depends on the airfoil shape and the pitch rate. As the vortex is convected past the trailing edge, the pitching moment briefly attains its maximum negative value and then both lift and pitching moment start to drop rapidly. The flow over the airfoil remains stalled until the angle of attack has decreased sufficiently to enable flow reattachment. As a result of this sequence of flow events, the unsteady lift, drag, and pitching moment coefficients show a large degree of flow hysteresis when plotted as a function of incidence angle. The amount of hysteresis and the shape of the hysteresis loops vary in a highly non-linear fashion with the amplitude of oscillation, mean angle of attack, and reduced frequency of oscillation. For a more detailed presentation of the physics of the dynamic stall process we refer to the recent review paper by Carr and Chandrasekhara[11] and to the references cited therein.

3. SEMI–EMPIRICAL PREDICTION METHODS

Due to the extremely complicated nature of the dynamic stall phenomena, the helicopter industry was forced to resort to the development of empirical or semi-empirical methods for the prediction of the dynamic stall loads. These methods are based on force and pitching

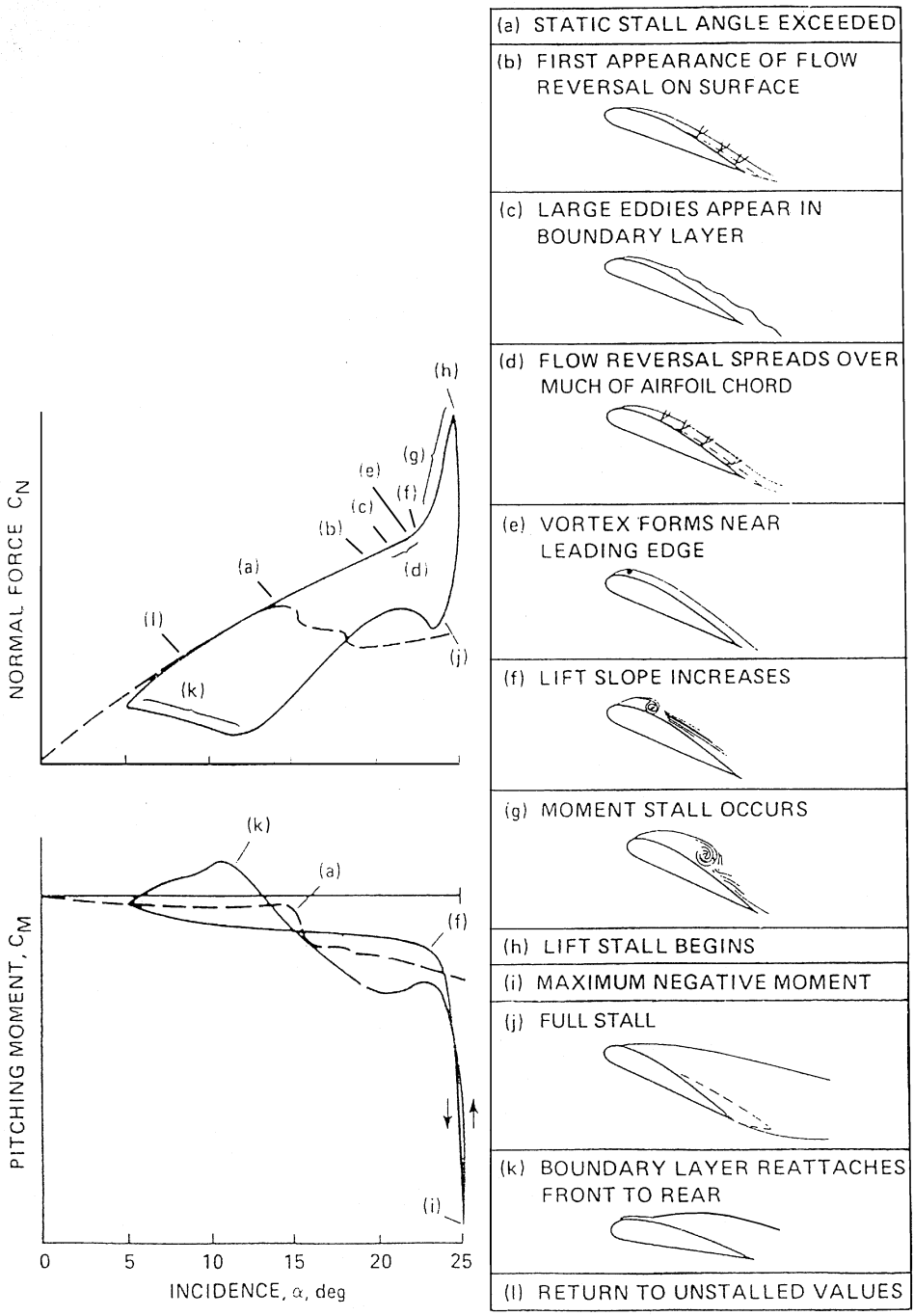

Fig. 1. Dynamic stall events on a NACA-0012 airfoil at low free-stream Mach number [from Ref. (10)].

moment data obtained from various wind tunnel tests. They are used as the main design information in the industry.

For example, Boeing–Vertol[74,69] developed the so-called gamma function method, where the gamma function is an empirical function, which depends on airfoil geometry and Mach number and is different for lift and moment stall. The United Technologies Research Center (UTRC)[61] developed a time domain unsteady aerodynamic model, based on oscillating airfoil tests. The parameters selected for use in this method are the instantaneous angle of attack or geometric angle of attack, the non-dimensional pitch rate, and an

additional parameter which represents the difference between the instantaneous angle of attack and the effective angle of attack. This parameter therefore accounts for the time history effects of the change in angle of attack. Further details of this approach are documented by Gangwani.[61] At Lockheed, Ericsson and Reding[49] developed a combined analytical/empirical model of dynamic stall which incorporates several time-lag effects. One effect is the delay of stall due to time lag and boundary-layer improvement effects and is assumed to be quasi-steady, i.e. the separation-induced unsteady characteristics are represented by the static aerodynamic characteristics, but modified to account for unsteady flow effects. This time-lag effect is assumed to be composed of the circulation lag, the boundary-layer convection time lag, and the moving wall or leading-edge jet effect. The other flow phenomena are regarded as transient and assumed to consist of the moving separation point effect and of the spilled vortex effect. For further details concerning the quantification of these lag effects and the incorporation of compressibility corrections we refer to Ericsson and Reding's survey.[52] At ONERA, a method was developed which uses a system of ordinary differential equations to fit the experimental force and pitching moment data.[148] More recently, Leishman and Beddoes[96] presented a semi-empirical model which consists of three distinct subsystems, namely an attached flow solution for the unsteady linear airloads, a separated flow solution for the non-linear airloads, and a dynamic stall solution for the vortex-induced airloads. Further work along this line was presented by Tyler and Leishman.[152]

4. COMPUTATION OF UNSTEADY AIRFOIL FLOWS

It is our purpose here to describe numerical methods which are used to compute attached and separated flows over airfoils in unsteady motion. To this end we start with the purely inviscid incompressible flow analyses in Section 4.1. The boundary-layer, viscous–inviscid interaction, and Navier–Stokes methods for incompressible and compressible flow are presented in Sections 4.2, 4.3 and 4.4, respectively.

4.1. UNSTEADY INCOMPRESSIBLE INVISCID AIRFOIL FLOWS

The governing equation of unsteady, inviscid, incompressible airfoil flows is the Laplace equation. The airfoil loads are obtained from the solution of this equation subject to the proper boundary and edge conditions. This is generally being done by distributing singularities (sources and vortices) along the airfoil surface. This approach is usually referred to as the panel method. Panel methods yield quick answers and they are used for inviscid flow analyses or in combination with boundary-layer methods.

4.1.1. Panel method

Solutions for unsteady, inviscid, incompressible flow over airfoils of arbitrary geometry undergoing defined pitching or plunging motions or being subjected to defined angle of attack changes have been pioneered by Giesing.[66] Basu and Hancock[5] and Kim and Mook[93] presented additional results using the paneling approach. At the Naval Postgraduate School, an unsteady panel code was developed by Teng.[146] The code follows closely the original method of Hess and Smith,[79] while with regard to the modeling of the unsteady wake it adopts the procedure of Basu and Hancock.[5] Uniform source and vorticity distributions are placed on each panel at time t. The wake consists of a single vorticity panel attached as an additional element on the airfoil through which discrete vortices are shed into the wake and convected downstream with the fluid. A uniform vorticity distribution is placed on the wake panel, and it is further characterized by its length and inclination with respect to the local frame of reference. After each time step, the vorticity of the wake panel is concentrated into a single point vortex and convected downstream. Simultaneously, a new wake panel is formed.

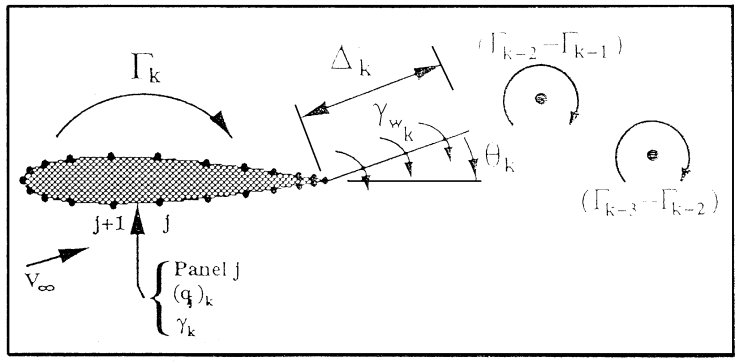

Fig. 2. Schematic of the airfoil panels and the wake model.

The flow tangency conditions are satisfied at the exterior mid-points (control points) of each panel. The Kutta trailing-edge condition postulates that the pressure difference between the upper and the lower surface vanishes at the trailing edge. The wake panel is formed with a length and inclination to the local frame of reference that satisfies the Helmholtz theorem

$$(\Delta l)_k(\gamma_w)_k + \Gamma_k = \Gamma_{k-1} \tag{1}$$

where (Δl) is the wake panel length, γ is the wake panel vorticity, Γ is the airfoil circulation and k denotes the timestep. Equation (1) introduces an additional condition, the conservation of vorticity. However, the introduction of the wake panel creates three additional unknowns; the vorticity of the wake panel, its length, and its inclination. Therefore, the following two additional conditions are required:

1. The wake panel is oriented in the direction of the local resultant velocity at the panel mid-point.
2. The length of the wake panel is proportional to the magnitude of the local resultant velocity at the panel mid-point and the size of the time step.

The essential elements of this scheme are summarized in Fig. 2. Note that the implementation of this approach requires an iterative scheme, since the velocity direction and magnitude used to define the wake panel are not initially known. A somewhat similar panel method was also developed by Yao *et al.*[171]

4.1.2. Lag effects due to unsteady airfoil motion

It is instructive to study first the purely inviscid incompressible, unsteady flow effects because the unsteady panel code has made it possible to compute detailed pressure distributions in a matter of seconds. Therefore, there is no need any longer to resort to quasi-steady lumped time history estimates of the time-lag effects, as described by Ericsson and Reding[52] or to use Theodorsen's flat plate theory, as applied by Tyler and Leishman.[152] Instead, the pressure-lag effects can be determined quite accurately and rapidly, within the limitations of inviscid incompressible flow theory, for airfoils of arbitrary geometry and for various flow conditions.

An example of unsteady, incompressible flow solution is presented in Fig. 3, where several computed pressure distributions near the leading edge of a NACA-0012 airfoil are shown. In this figure the origin corresponds to the leading edge, positive distance represents the upper surface, and negative distance the lower surface. The airfoil is either held steady at zero angle of attack or is pitching harmonically between $\pm 10^\circ$ angle of attack (AOA), with a reduced frequency of $k = 0.1$. The pressure distributions are plotted at that instant of time when the airfoil pitches through zero angle of attack (from positive to negative AOA). The dependence on pitch axis location is shown by plotting the pressures for five different pitch

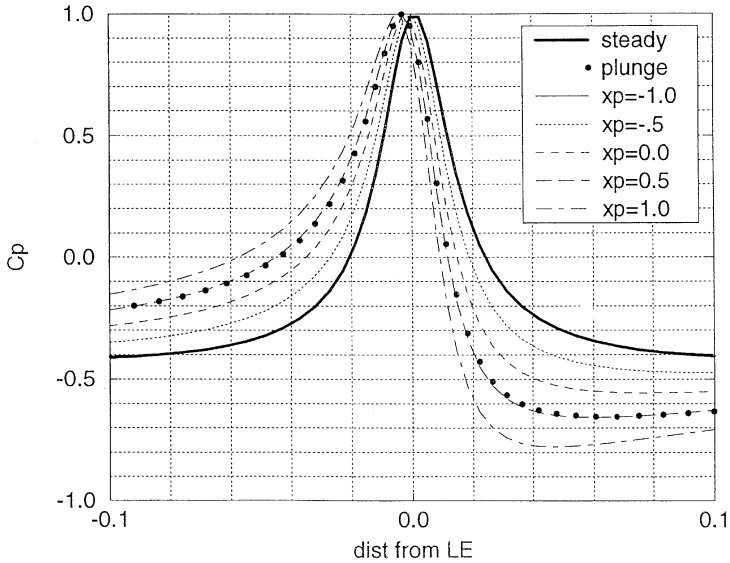

Fig. 3. Effect of pitching axis location on the leading edge pressure distribution; $k = 0.1$, $\alpha(t) = 10^\circ \sin(\omega t)$, $\alpha = 0^\circ$ down.

axis locations (trailing edge, mid-chord, leading edge, one-half chord and one chord upstream of the leading edge). In the same figure, the pressure distribution induced by a harmonically plunging airfoil is also shown. The plunge amplitude was chosen such that it yields a maximum effective angle of attack of $\pm 10^\circ$. The pressure distribution is plotted at that time instant when the plunging airfoil is at zero *effective* AOA, i.e. at the position of maximum downward deflection. It is seen that the pressure distribution near the leading edge varies almost linearly with the location of the pivot point. One observes a significant pressure lag relative to the steady-state pressure distribution. There is a lower pressure on the upper surface and a higher pressure on the lower surface than on the steady airfoil. This effect increases with increasing downstream location of the pitch axis. It is interesting to note that for pitch oscillation about the mid-chord point the pressure distribution matches that of the plunging airfoil. However, there is a 90° phase lag between the pitch and plunge motion. The pressures shown in Fig. 3 occur while the pitching airfoil moves at its maximum pitch rate while the plunging airfoil is at rest at the maximum downward position. As expected, this lag effect also occurs when the airfoil pitches up and when it is in the uppermost position during the plunge oscillation.

In Fig. 4, the lower pressure now occurs on the lower surface as the airfoil pitches through the zero angle of attack position and the higher pressure on the upper surface as compared to the steady angle of attack pressures. It is also of interest to compare the pressures when the airfoil is at the maximum positive or negative angles of attack during the pitch oscillation or when the plunging airfoil moves through its mean position. These pressure distributions are shown in Figs 5 and 6. Here again it is seen that there is a significant lag effect which occurs on the upper surface at the maximum positive angle of attack, as shown in Fig. 5, and at the maximum negative angle of attack, as shown in Fig. 6. Further insight about the time-lag effect can be obtained by looking at the ramp-type pitch motion of the airfoil. Figure 7 shows the computed lift build-up on the NACA 0012 airfoil due to a ramp motion of different pitch rates. It is seen that the lift build-up occurs more slowly as the pitch rate is increased.

Similarly, the unsteady panel code allows the rapid computation of the lift and moment dependence on airfoil motion, airfoil shape, and reduced frequency. For example, Figs 8 and 9 show the computed lift and pitching moment variations over the entire oscillation cycle (from 0 to 2π), for a NACA 0001 airfoil which is pitching harmonically about its aerodynamic center with an amplitude of $\pm 0.1^\circ$ at reduced frequencies of $k = 0.1$ and 0.2.

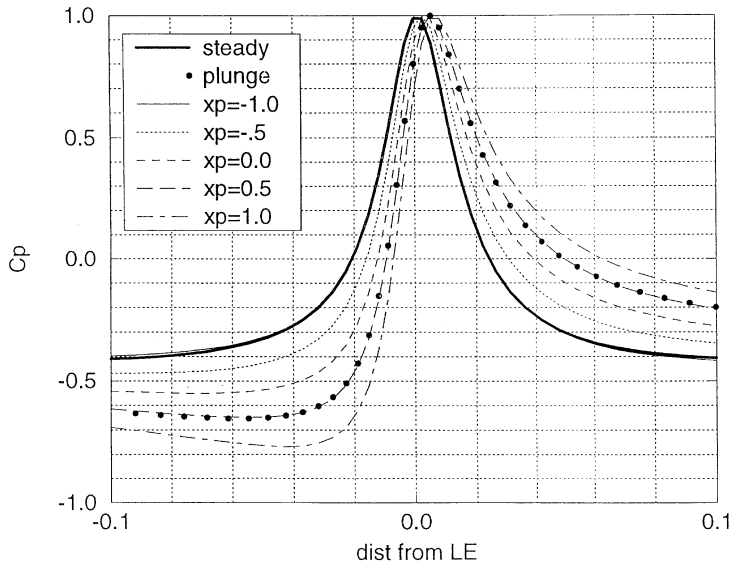

Fig. 4. Effect of pitching axis location on the leading edge pressure distribution; $k = 0.1, \alpha(t) = 10^\circ \sin(\omega t)$, $\alpha = 0^\circ$ up.

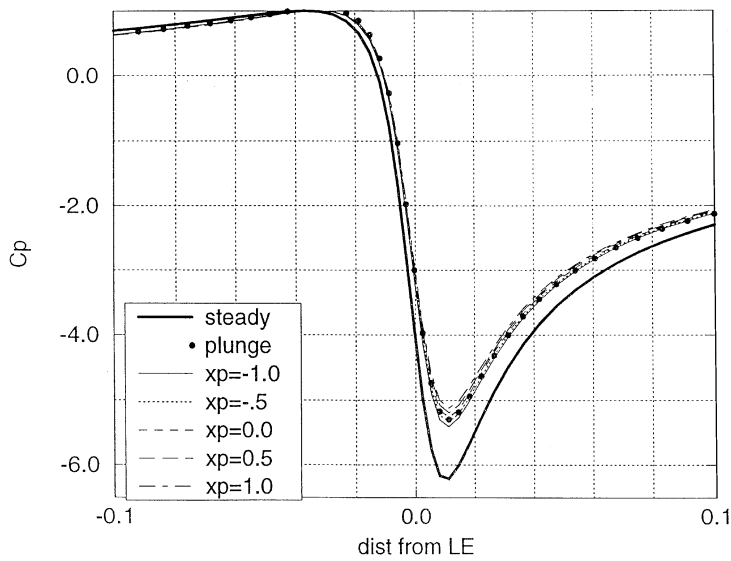

Fig. 5. Effect of pitching axis location on the leading edge pressure distribution; $k = 0.1, \alpha(t) = 10^\circ \sin(\omega t)$, $\alpha = +10^\circ$.

The computations were performed with the unsteady panel code UPOT. Also shown in the same figures are the predictions of the low-frequency theory of Miles[112] and the quasi-steady theory of Munk.[115] It is seen that Miles' theory is in good agreement up to a reduced frequency $k = 0.2$, whereas Munk's quasi-steady theory gives the wrong moment prediction even at very low frequencies (as already pointed out by Miles). Further detailed validations of the panel code by comparing it with Theodorsen's theory have been conducted by Riester[127] and Turner.[151]

As a consequence of the lag effect, both lift and pitching moment develop hysteresis loops. As already pointed out by Smilg[138] and Fung,[57] there are fundamental differences between pitch and plunge oscillations. For example, the pitching airfoil may be unstable if the oscillation occurs at low frequency about a pitch axis forward of the quarter–chord

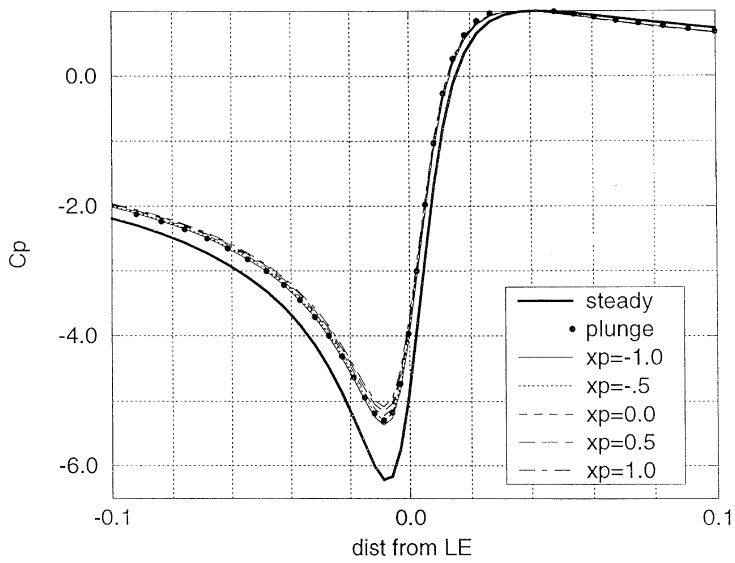

Fig. 6. Effect of pitching axis location on the leading edge pressure distribution; $k = 0.1$, $\alpha(t) = 10^\circ \sin(\omega t)$, $\alpha = -10^\circ$.

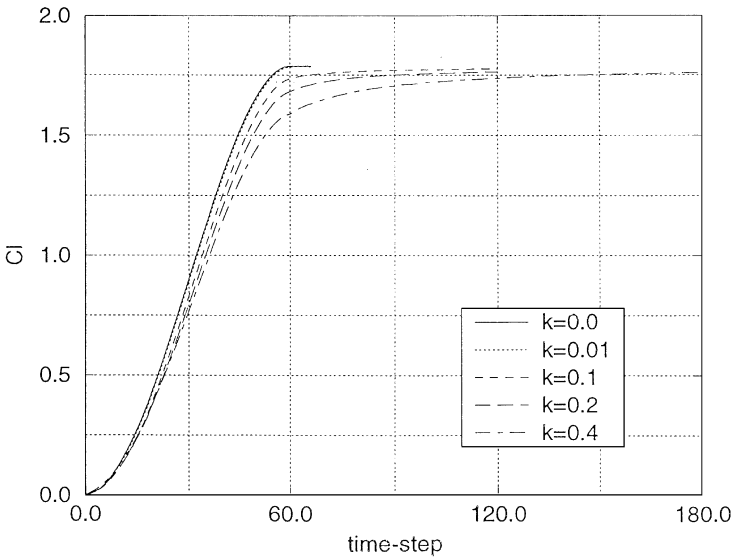

Fig. 7. Effect of reduced frequency on the unsteady lift at ramp motion.

point. Figure 10 depicts a counterclockwise pitching moment hysteresis loop when the airfoil pitches with a reduced frequency of 0.1. This represents a negative pitch damping. The hysteresis loop changes to a clockwise loop as the reduced frequency is increased to $k = 0.2$. A plunging airfoil, on the other hand, is always stable, as demonstrated by Fung.[57] It is also of interest to note another distinct difference between the axial forces developed by pitching versus plunging airfoils. As noted by von Karman[91] and Garrick,[60] plunging airfoils develop a thrust force, whereas pitching airfoils show this effect only at rather high frequencies. These differences become particularly apparent in the different vortical wake behavior, as noted by Freymuth[56] and Jones *et al.*[88] Therefore, care needs to be exercised in postulating equivalent angles of attack.

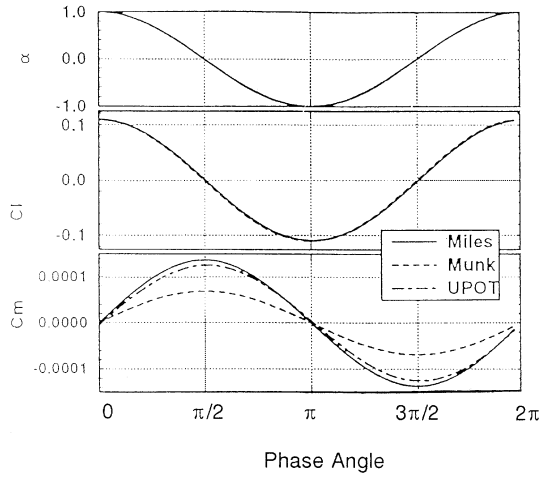

Fig. 8. Comparison of the computed unsteady lift and pitching moment with the analytic results for $k = 0.1$.

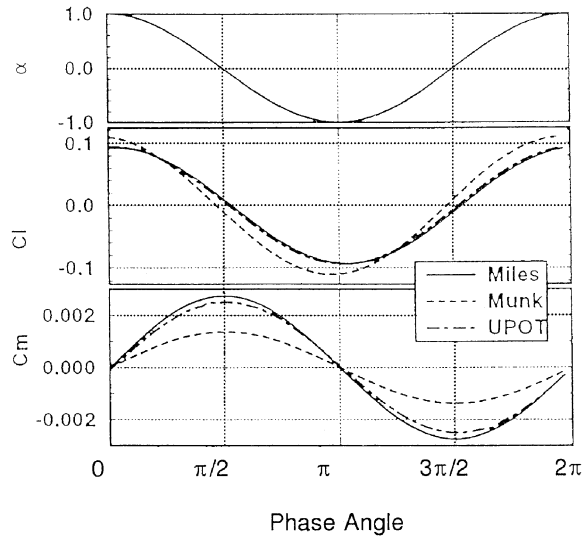

Fig. 9. Comparison of the computed unsteady lift and pitching moment with the analytic results for $k = 0.2$.

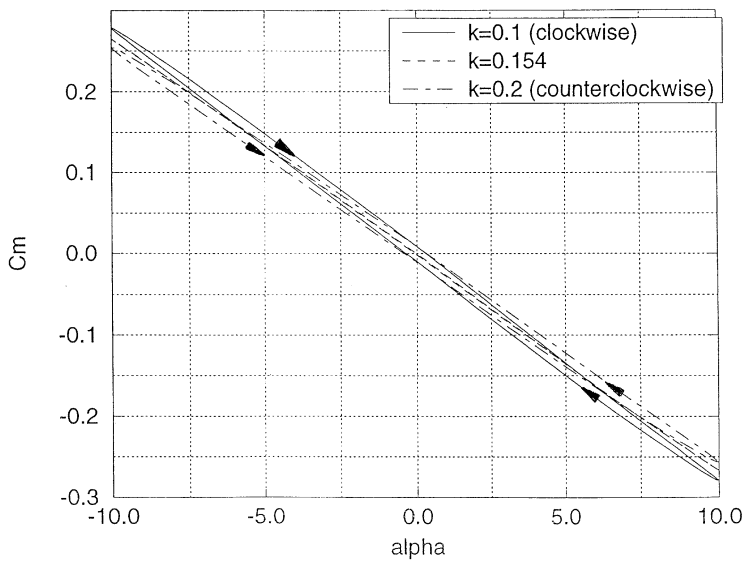

Fig. 10. Effect of reduced frequency on the computed pitching moment hysteresis.

4.2. BOUNDARY-LAYER METHOD FOR INCOMPRESSIBLE AIRFOIL FLOWS

The boundary-layer equations for two-dimensional incompressible laminar and turbulent flows are well known and, with the eddy viscosity concept, can be expressed in the following form:

$$\frac{\partial u}{\partial x} + \frac{\partial v}{\partial y} = 0 \tag{2}$$

$$\frac{\partial u}{\partial t} + u\frac{\partial u}{\partial x} + v\frac{\partial u}{\partial y} = \frac{\partial U_e}{\partial t} + U_e\frac{\partial U_e}{\partial x} + v\frac{\partial}{\partial y}\left(b\frac{\partial u}{\partial y}\right) \tag{3}$$

where U_e is the boundary layer edge external velocity, $b = 1 + \varepsilon_m/v$, v is the kinematic viscosity and ε_m is the turbulent eddy viscosity. The boundary conditions require that both velocity components u and v are zero on the airfoil and that at the edge of the boundary layer the velocity must assume the value U_e, specified by the panel method. The boundary conditions in the wake require the definition of a dividing line.

4.2.1. *Cebeci finite-difference method*[14]

The above boundary layer equations are first expressed in Falkner–Skan-transformed coordinates. This has the advantage over the physical coordinates that the calculations can be performed using larger steps in the streamwise direction. In addition, the use of this transformation removes the singularity the equations have in physical coordinates at the stagnation point of an airfoil. The Falkner–Skan transformation is given by

$$\eta = \sqrt{\frac{U_e}{vx}}\,y; \quad \Psi = \sqrt{U_e v x}F(x,\eta)$$

and the boundary-layer equations in transformed coordinates are

$$(bF'')' + \frac{m+1}{2}FF'' + m[1 - (F')^2 + m_3(1 - F') - \frac{m_3}{2}F''$$

$$= x\left(\frac{1}{U_e}\frac{\partial F'}{\partial t} + F'\frac{\partial F'}{\partial x} - F''\frac{\partial F'}{\partial x}\right) \tag{4}$$

Here a prime denotes differentiation with respect to η and m and m_3 are dimensionless pressure gradient parameters given by

$$m = \frac{x}{U_e}\frac{\partial U_e}{\partial x}; \quad m_3 = \frac{x}{U_e^2}\frac{\partial U_e}{\partial t} \tag{5}$$

For the solution of these equations, initial and upstream conditions must be specified. There is no problem in generating the upstream conditions for the steady flow equations since the calculations start at the stagnation point. However, the situation is somewhat different for unsteady flows because the stagnation point is not fixed. Usually, a quasi-steady approach can be justified in the immediate vicinity of the stagnation point and the solution is started as a standard steady-state problem. For the numerical solution, with Keller's box method, Equation (4) is rewritten as a system of first-order equations. The finite-difference approximations are obtained using central differences for the net cube of Fig. 11. The numerical solution proceeds by marching for a given time along the streamwise direction. The resulting nonlinear system is solved by Newton's iteration method. Further details of this approach are given by Jang.[85]

The Cebeci–Smith (C–S) eddy-viscosity model[13] is used for the computation of high Reynolds number turbulent flows. This model has become widely used for the computation of turbulent boundary-layer-type flows. The C–S model leaves the basic boundary-layer

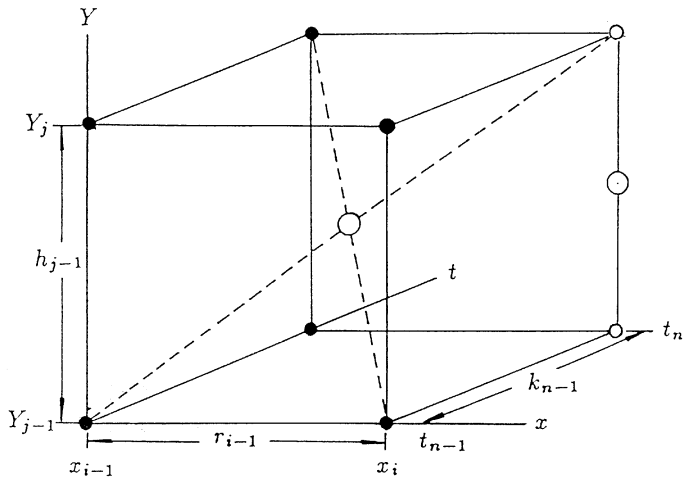

Fig. 11. Net cube for the numerical solution of the unsteady two-dimensional boundary-layer equations.

equations unchanged but modifies the viscosity term by adding a local eddy viscosity to the laminar flow kinematic viscosity. The C–S model divides the viscous region into an inner and an outer layer with the eddy viscosity in each region empirically formulated. The equations describing this model are listed in Appendix C.

4.2.2. Empirical transition onset prediction

In many cases, the point of transition onset is of critical importance for the prediction of dynamic stall. At high Reynolds numbers, the flow may remain fully attached near the leading edge prior to the onset of transition. At lower Reynolds numbers, typically less than one million, a separation bubble may be formed and transition occurs inside the separation bubble. In recent experiments, Malkiel and Mayle[106] have found that the laminar shear layers in separation bubbles can be characterized as a combination between attached boundary layers and free shear layers and, therefore, the transition process in separation bubbles can be modeled with the turbulent spot theory used in attached boundary layers, but there is also evidence of Kelvin–Helmholtz pairing encountered in free shear layers.

At high Reynolds numbers, Michel's empirical transition onset criterion[111] has been found to give good results and therefore has been widely adopted. According to this criterion, transition is initiated when the Reynolds number based on momentum thickness, Re_θ, and the Reynolds number based on the running length, Re_x, satisfy the equation

$$\mathrm{Re}_{\theta_{\mathrm{tr}}} = 1.174\left(1 + \frac{22400}{\mathrm{Re}_{x_{\mathrm{tr}}}}\right)\mathrm{Re}_{x_{\mathrm{tr}}}^{0.46} \tag{6}$$

$\mathrm{Re}_\theta = U_e\theta/\nu$. Unfortunately, at lower Reynolds numbers the available empirical information is insufficient for the formulation of a similar empirical criterion. Therefore, the location of the transition onset has to be chosen judiciously. The sensitivity of the dynamic stall calculations to the choice of transition onset location will be shown in Section 5.

4.2.3. Empirical transition length prediction

The transition length correlation first introduced by Dhawan and Narasimha[37] was based on a limited range of data essentially derived from data obtained in constant pressure flows. Chen and Thyson[26] subsequently used the turbulent spot theory of Emmons[48] to develop a transitional flow model which allowed to account for the influence of pressure gradient on the intermittency distribution and transition length. The Chen–Thyson[26]

transition model is based on data for attached flows and uses an effective eddy viscosity for the computation of the transitional flow region. For the computation of the transitional flow region the transition onset point must be specified or computed and the model provides both transition length and the turbulent intermittency γ_{tr}. The effective eddy viscosity is obtained from the turbulent eddy viscosity, computed from a turbulence model, by scaling with an intermittency function. This function is zero in the laminar region and from the transition onset point progressively increases in the transitional region until it reaches unity in the fully turbulent region. The intermittency function is given by

$$\gamma_{tr} = 1 - \exp\left[C_{tr} U_e^3(x) \, (x - x_{tr}) \int_{x_{tr}}^{x} \frac{dx}{U_e(x)} \right], \tag{7}$$

$$C_{tr} = \left(-\frac{\mathrm{Re}_{x_{tr}}^{-1.34}}{G_{\gamma_{tr}} v^2} \right)$$

where $U_e(x)$ is the boundary-layer edge velocity, x_{tr} is the transition location and $G_{\gamma_{tr}}$ is a parameter of the model which determines the length of the transitional region. For high Reynolds number the recommended value of $G_{\gamma_{tr}}$ is 1200. For low Reynolds numbers this parameter is given by the following empirical formula proposed by Cebeci:

$$G_{\gamma_{tr}} = \frac{213[\log(\mathrm{Re}_{x_{tr}}) - 4.732]}{3} \tag{8}$$

Physically, a low value of $G_{\gamma_{tr}}$ forces transition to take place over a shorter distance. Recently, Gostelow *et al.*[68] performed systematic measurements of the influence of pressure gradient and free-stream turbulence level on transition length. They showed that their correlations gave reliable predictions of transition length for strongly decelerating flows in cases where the pressure gradient did not change significantly over the transition zone. This correlation was further improved by Solomon *et al.*[139] for flows with rapidly changing adverse pressure gradients. No measurements are as yet available on the effect of flow unsteadiness on the transition location and length. Therefore, in the dynamic stall computations the quasi-steady flow assumption is considered to be adequate for the relatively small reduced frequencies typically encountered in practice.

4.2.4. Boundary-layer-lag effects

Section 4.1.2 dealt with the inviscid response characteristics of oscillating or transiently pitching airfoils in incompressible flow and it was demonstrated that significant time lag effects may occur. Therefore, it is of interest to estimate the time lags which may occur in attached airfoil boundary layers. This can be done by examining the step response characteristics of boundary layers. The development of the boundary layer on an infinite plate, initially at rest in a viscous fluid, but suddenly moved parallel to itself with a constant velocity, can be found from the solution for the so-called Stokes layer. According to Hancock and Mabey,[72] the time taken for a boundary layer thickness δ to develop is

$$t = \frac{\delta^2}{13\nu} \tag{9}$$

Hence, the time for the boundary layer at the trailing edge of an airfoil which is suddenly moved forward is given by the same estimate. According to Cebeci–Smith,[18] the turbulent eddy viscosity can be estimated as

$$\nu_{turb} = \frac{U_e \delta}{500} \tag{10}$$

The boundary layer thickness at the airfoil trailing edge typically is of the order of 2% chord length. This gives an aerodynamic rise time for the boundary layer of approximately

one in contrast to typical inviscid aerodynamic rise times of 50 (as estimated from Wagner's step response function). The aerodynamic time is defined as chord divided by flight velocity. This analysis shows that unsteady effects in the boundary layer can be expected to be quite small. Therefore, the use of a steady-state boundary-layer code in combination with the unsteady panel code is likely to provide a good estimate of the boundary-layer development on oscillating or pitching airfoils.

4.2.5. Moving wall effect

Ericsson and Reding[52] introduced the concept of the moving wall or the "leading edge jet" effect to explain the observed stall delay on pitching airfoils. They argue that the effect is similar to the boundary-layer behavior on a rotating cylinder and that, therefore, the leading edge can be replaced by a rotating cylinder. It is instructive to study the boundary-layer development on a pitching airfoil using the unsteady panel code in combination with the Cebeci steady-state boundary-layer code. Figure 12 shows the computed boundary-

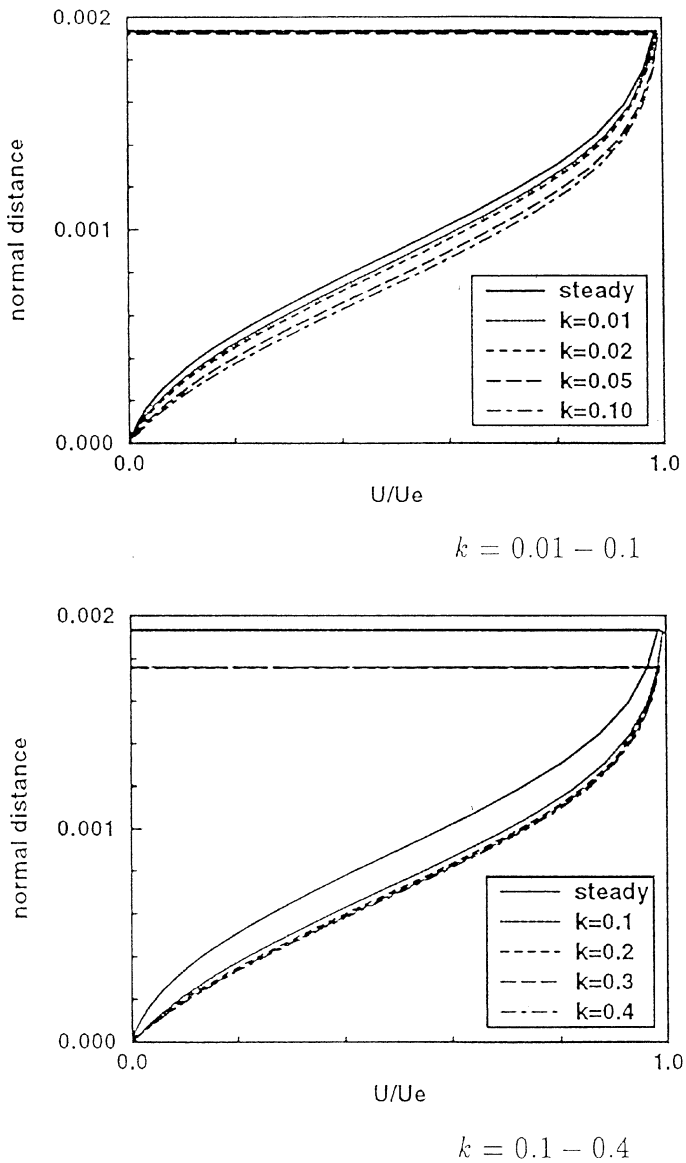

Fig. 12. Effect of reduced frequency on the computed boundary-layer profiles at 10% chord of a NACA-0012 airfoil [from Ref. (89)].

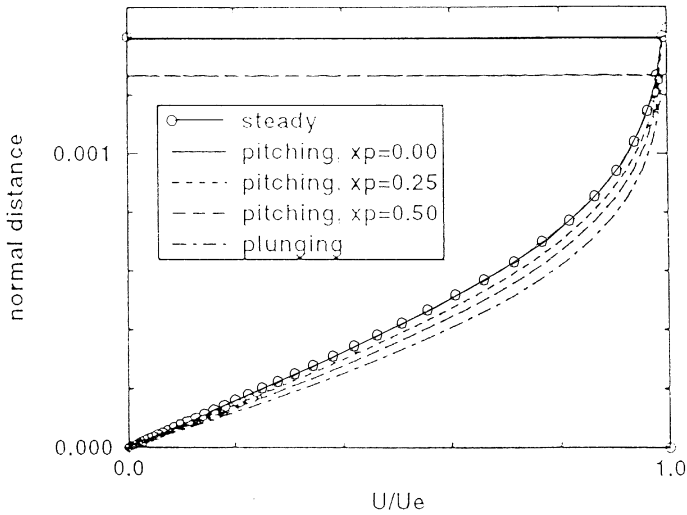

Fig. 13. Effect of pitching axis location on the computed boundary-layer profile at 10% chord of a NACA-0012 airfoil [from Ref. (89)].

layer profiles 10% downstream from the leading edge on the upper surface of a NACA 0012 airfoil.[89] The airfoil pitches from 0 to 20° according to a modified ramp function. The Reynolds number is chosen to be one million. It is seen that the boundary-layer profiles become fuller as the pitching rate is increased, supporting Ericsson's and Reding's moving-wall hypothesis. However, as already pointed out in Figs 3–6, the location of the pivot point is quite important. The effect of varying the pivot location is illustrated in Fig. 13. The boundary layer profiles at a fixed position, roughly 10% downstream from the leading edge on the upper surface, are compared for a NACA 0012 airfoil at a geometric angle of attack of zero degrees for several cases. Included are a steady solution, oscillatory pitching solutions with an angle of attack range of $\pm$ 5°, a reduced frequency of $k = 1.0$, and pivot locations of 0, 0.25, and 0.5, and an oscillatory plunge solution at a reduced frequency of 1.0 with $h = 0.0875$, yielding an effective angle of attack range of $\pm$ 5°. While all five cases have a zero geometric angle of attack, they have different effective angles of attack. Both the steady case and the case of pitching about the leading edge have a zero effective angle of attack, and the velocity profiles are almost identical. Pitching about the quarter chord point generates an effective angle of attack of 1.25°, pitching about mid-chord generates 2.5°, the plunging case has an effective angle of 5.0°, and the velocity profiles become progressively fuller.

Unsteady boundary-layer solutions for a NACA-0012 airfoil in ramp motion were compared with a Navier–Stokes solution in Ref. (43). Surface pressure distributions obtained from a turbulent unsteady boundary-layer solution with the Cebeci–Smith turbulence model for ramp motion of a NACA-0012 airfoil were in good agreement with the unsteady pressure measurements.[95] The boundary layer profiles obtained from the boundary-layer solution and the Navier–Stokes solution computed with the Baldwin–Lomax turbulence model[4] are compared in Fig. 14 for the mid-chord location ($x/c = 0.5$) and different angles of incidence. It is seen that the unsteady boundary-layer solution and the Navier–Stokes solutions are in excellent agreement for all angles of incidence except for $\alpha = 15.5°$ (Fig. 14d) where the flow starts to separate at the trailing edge.

It is also instructive to observe the onset of flow separation for the same pitching NACA-0012 airfoil using the modified ramp with varying pitch rates.[89] Figure 15 shows the angle of attack for which laminar separation is first predicted as a function of the pitch rate. As expected, laminar separation is delayed as the pitch rate is increased, but interestingly the position of the separation point and the point of laminar separation remain constant. In fact, the pressure gradient distribution at the angle of attack where laminar

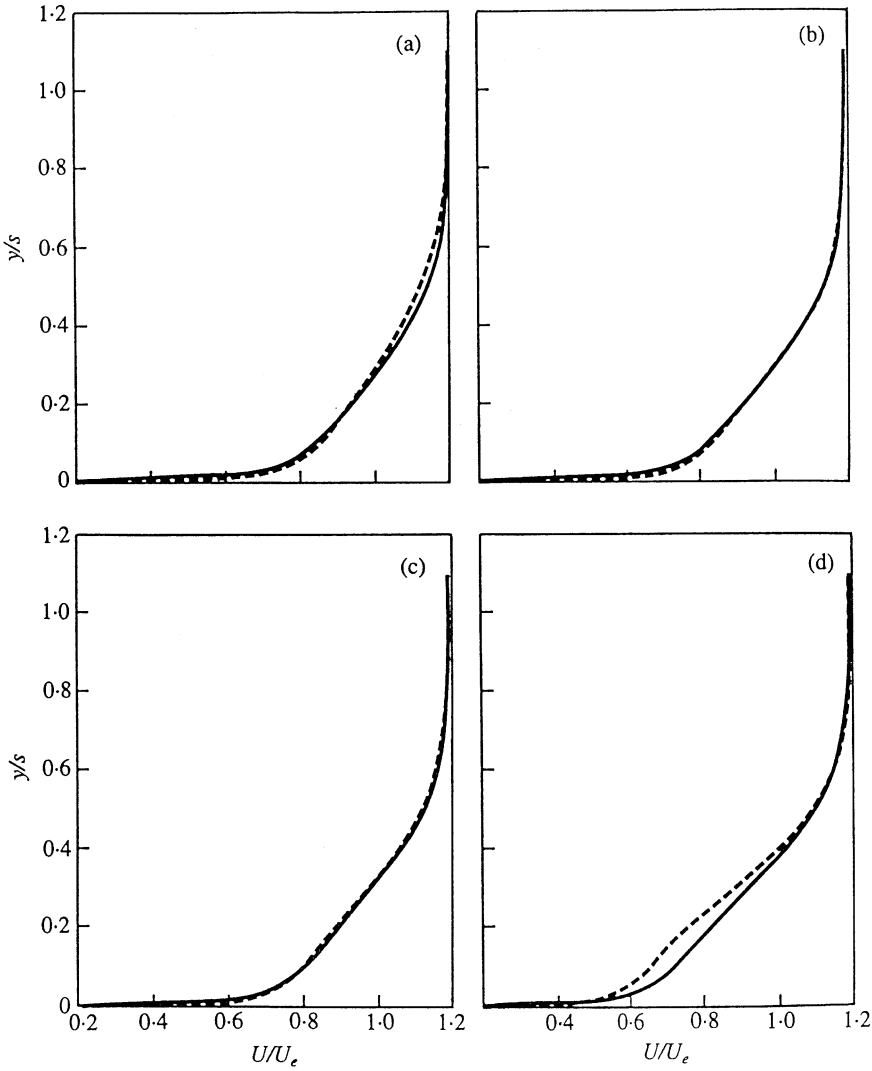

Fig. 14. Comparison of the velocity distributions obtained from the unsteady boundary-layer solution (- - - -) and the Navier–Stokes solution (——) for (a) $\alpha = 5.8°$, (b) $\alpha = 8.9°$, (c) $\alpha = 11.7°$, and (d) $\alpha = 15.5°$ [from Ref. (43)].

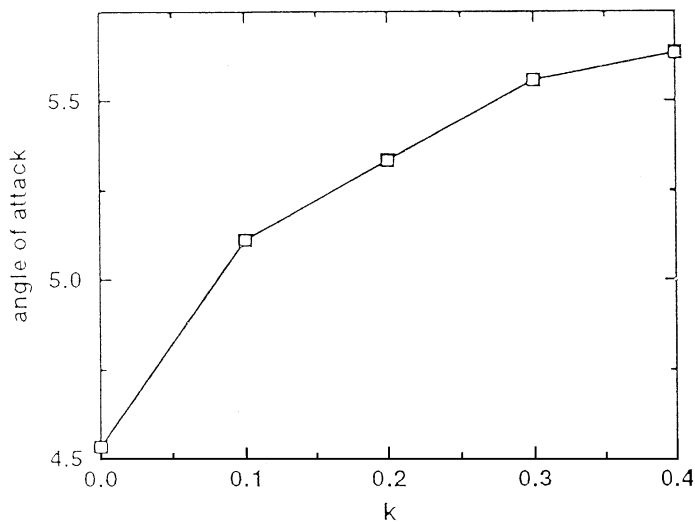

Fig. 15. Effect of reduced frequency on dynamic-stall angle of attack onset [from Ref. (89)].

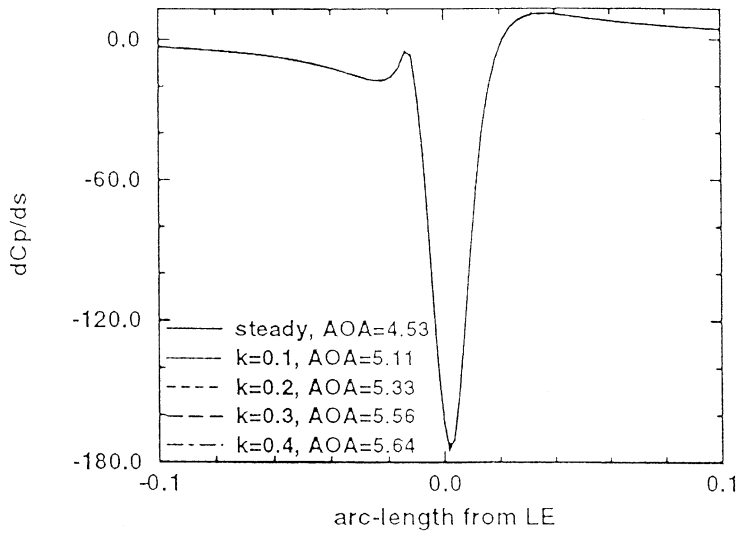

Fig. 16. Pressure gradient distribution at stall onset [from Ref. (89)].

separation first occurs is virtually identical in each case, as shown in Fig. 16. This means that the boundary layers will also be identical for each case. The delay in dynamic stall onset shown here is in qualitative agreement with the experimental results of Chandrasekhara *et al.*,[23] who could not determine the first stages of dynamic stall, but visually identified dynamic stall by the appearance of a leading edge vortex.

4.3. VISCOUS–INVISCID INTERACTION METHODS

Viscous–inviscid interaction methods have become a powerful and efficient tool. They have been used in recent years to compute steady airfoil flows with separated flow regions so that the near stall and post-stall behavior can be predicted. To this end, an inviscid outer flowfield calculation based on either the potential flow or the Euler equations is either coupled with a boundary-layer or Navier–Stokes calculation of the flow near the airfoil. Various coupling procedures with the boundary-layer equations have been developed. Veldman *et al.*, LeBalleur, Williams and Smith and Cebeci *et al.* provided comprehensive reviews of these methods in Volume IV of Numerical and Physical Aspects of Aerodynamic Flows, edited by Cebeci.[14] Recent extensions of these approaches to the computation of unsteady airfoil flows with separated flow regions are described in the following two sections.

4.3.1. Potential flow/boundary-layer method

Cebeci *et al.*[19] based their extension on the coupling between the unsteady inviscid incompressible potential flow solution and the solution of the unsteady boundary-layer equations. The Laplace equation is solved by the panel method described in Section 4.1.1 and the solution of the boundary-layer equations is obtained with the Cebeci finite-difference method described in Section 4.2.1. To calculate flows with separation, the external velocity was computed as part of the solution. This is done with the coupling procedure originally proposed by Veldman[155] according to which the perturbation velocity due to viscous effects is assumed to be given by the so-called Hilbert integral

$$\delta U_e(x, t) = \frac{1}{\pi} \int_{x_a}^{x_b} \left[\frac{d}{d\sigma} (U_e \delta^*) \right] \frac{d\sigma}{(x - \sigma)} \tag{11}$$

where δ^* is the displacement thickness and the interaction region is confined between x_a and x_b. In order to generate the proper upstream conditions, a convenient procedure for the calculation of the first velocity profile at the new time step has been developed by Cebeci and Carr.[16] This procedure involves the characteristic box scheme developed by Cebeci and Stewartson, as described in Bradshaw *et al.*[9]

4.3.2. *Potential flow/Navier–Stokes method*

The potential flow/boundary-layer interaction method is limited in its applicability by the assumptions inherent in the derivation of the boundary-layer equations. In addition, this approach requires the modeling of the unsteady wake. An alternative therefore is the computation of the near-field by the Navier–Stokes equations.

To this end, Tuncer *et al.*[150] coupled the Reynolds-averaged thin-layer Navier–Stokes equations with a potential flow panel code. In a conventional Navier–Stokes solution the computational domain typically extends 15 chord lengths from the airfoil surface. In contrast, in this interaction approach the computational domain boundaries can be placed as close as one-fifth of a chord length from the airfoil surface. The boundary conditions at the outer boundary are obtained from the potential flow solution. The boundary conditions for the potential flow solution are, in turn, computed by the Navier–Stokes solver on the inviscid flow zone beyond the boundary layers. Thus, the potential and Navier–Stokes flow solutions are coupled through their boundary conditions. The vortical wake generated by the airfoil motion is modeled with concentrated wake vortices and fully captures the unsteadiness contained in the wake. Further details are described by Tuncer *et al.*,[150] who showed that this approach yields a 30–50% grid point savings compared to the full Navier–Stokes computations. An example of an unsteady flow calculation using the Navier–Stokes potential flow method is shown in Fig. 17. The unsteady lift and drag coefficients obtained from a full Navier–Stokes solution and the potential/Navier–Stokes method are compared with the experimental data of Ref. (103). It can be seen that the zonal method is capable of predicting attached or mildly separated flows as accurately as the full Navier–Stokes method. A viscous–inviscid interaction procedure was also used in Refs (54, 145) for the computation of steady-state incompressible flows over airfoils and wings. In Ref. (54) the flowfield near the airfoil surface was computed with the parabolized Navier–Stokes equations. In Ref. (145), the near-field solution was obtained from the solution of the compressible flow equations.

4.4. NAVIER–STOKES METHODS

In this section the Navier–Stokes methods used in numerical investigations and predictions of dynamic stall flows are presented. First, the governing equations for compressible and incompressible flow are summarized. Next, numerical schemes for both the compressible and incompressible flow equations are presented.

4.4.1. *Compressible flow equations*

It is well established by experimental investigation that compressibility effects become important for freestream speeds $M_\infty \geqslant 0.2$. Most dynamic stall flows of practical interest occur at free-stream speeds $0.2 \leqslant M_\infty \leqslant 0.5$, and $0.5 \times 10^6 \leqslant \mathrm{Re}_c \leqslant 4 \times 10^6$, i.e. in the compressible, fully turbulent and possibly transitional/turbulent flow regime. For Reynolds numbers greater than a million, only a small region of the leading edge flow is transitional and fully turbulent flow is usually found for a large portion of the suction side. Therefore, numerical investigations of these problems require solution of the Reynolds-averaged, compressible Navier–Stokes equations. The strong conservation law form of the compressible flow equations is used for numerical solutions in order to enable capturing of flow discontinuities such as shock waves which appear at free-stream speeds $M_\infty \geqslant 0.4$.

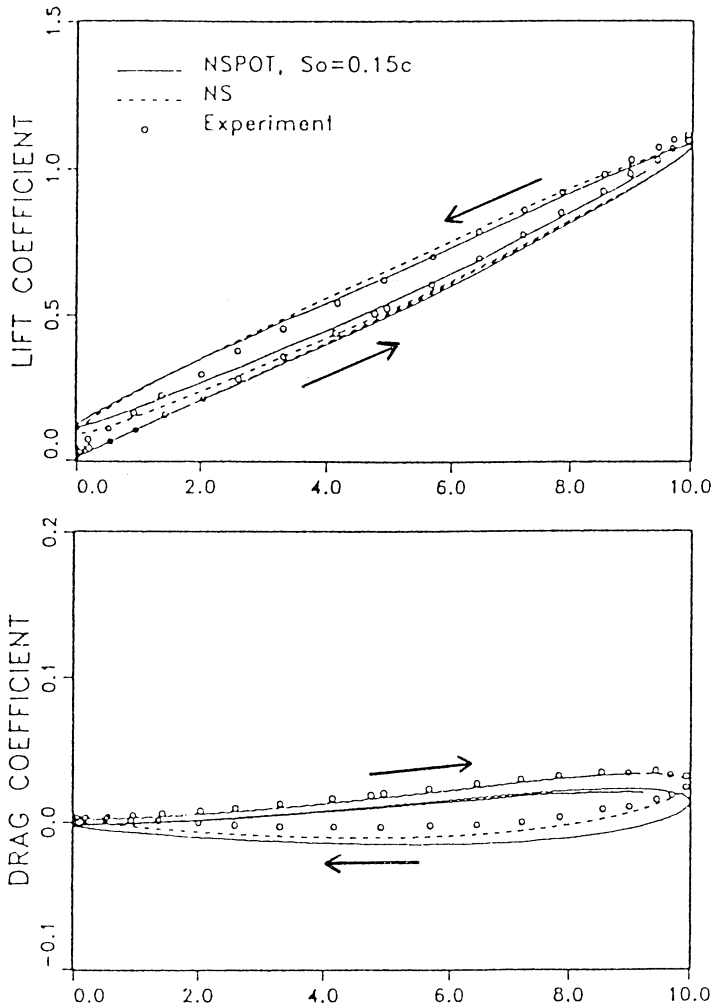

Fig. 17. Comparison of the lift hysteresis computed with the Navier–Stokes/potential flow method with the experiment [from Ref. (150)].

For simplicity, only the two-dimensional form of the compressible flow governing equations and the numerical schemes for their solution are presented. The extension to the three-dimensional case is straightforward.

In order to facilitate the numerical implementation for unevenly stretched grids and arbitrary body shapes the governing equations are written in a body-fitted, curvilinear coordinate system (ξ, η) as follows:

$$\partial_t \hat{\mathbf{Q}} + \partial_\xi \hat{\mathbf{F}} + \partial_\eta \hat{\mathbf{G}} = \frac{1}{\mathrm{Re}}(\partial_\xi \hat{\mathbf{R}} + \partial_\eta \hat{\mathbf{S}}) \tag{12}$$

where $\xi = \xi(x, y, t)$, $\eta = \eta(x, y, t)$ are the curvilinear coordinates along the streamwise and normal to the body directions, respectively. The conservative variable vector $\hat{\mathbf{Q}}$ and the non-linear, inviscid flux vectors $\hat{\mathbf{F}}$, $\hat{\mathbf{G}}$ are given by

$$\hat{\mathbf{Q}} = \begin{pmatrix} \rho \\ \rho u \\ \rho v \\ e \end{pmatrix}, \quad \hat{\mathbf{F}} = \frac{1}{J}\begin{pmatrix} \rho U \\ \rho u U + \xi_x p \\ \rho v U + \xi_y p \\ (e+p)U - \xi_t p \end{pmatrix}, \quad \hat{\mathbf{G}} = \frac{1}{J}\begin{pmatrix} \rho V \\ \rho u V + \eta_x p \\ \rho v V + \eta_y p \\ (e+p)V - \eta_t p \end{pmatrix} \tag{13}$$

where U, V are the contravariant velocity components along the ξ and η directions given by

$$U = u\xi_x + v\xi_y + \xi_t$$

$$V = u\eta_x + v\eta_y + \eta_t$$

The vectors $\hat{\mathbf{R}}$ and $\hat{\mathbf{S}}$ are the viscous stress vectors in the ξ and η directions, respectively. The viscous terms may be retained in both directions with explicit time-integration schemes. Factorized implicit schemes, such as the Beam–Warming algorithm, require to consider the thin layer approximation of the viscous terms. The thin layer approximation of the $\hat{\mathbf{S}}$ viscous flux vector in the η-direction is written as

$$\hat{\mathbf{S}} = \frac{1}{J}\begin{pmatrix} 0 \\ \mu m_1 u_\eta + (\mu/3) m_2 \eta_x \\ \mu m_1 v_\eta + (\mu/3) m_2 \eta_y \\ \mu m_1 m_3 + (\mu/3) m_2 m_4 \end{pmatrix}$$

Here

$$m_1 = \eta_x^2 + \eta_y^2$$

$$m_2 = \eta_x u_\eta + \eta_y v_\eta$$

$$m_3 = \left(\frac{1}{2}\right)\frac{\partial}{\partial \eta}(u^2 + v^2) + \frac{1}{\mathrm{Pr}(\gamma - 1)}\left(\frac{\partial a^2}{\partial \eta}\right)$$

$$m_4 = \eta_x u + \eta_y v$$

where ξ_x, ξ_y, η_x, η_y, ξ_t, and η_t are the coordinate transformation metrics. The thin-layer approximation neglects the viscous diffusion in the direction parallel to the surface and retains only the contributions from the diffusion in the normal direction.

In the above equations, all geometrical dimensions are normalized with the airfoil chord length, c, the Cartesian velocity components, u and v, are scaled by the free-stream sound speed a_∞, and the time t is normalized as tc/a_∞, p is the static pressure normalized by $\rho_\infty a_\infty$, ρ is the density normalized by free-stream density ρ_∞, e is the total energy per unit volume normalized by $\rho_\infty a_\infty^2$, a is the speed of sound, Re is the Reynolds number; Pr is the Prandtl number, γ is the ratio of specific heats, and μ is the viscosity coefficient normalized by its free-stream value and related to temperature by Sutherland's law $\mu = (1.45T^{2/3})/(T + 110)$. The pressure is related to the density and total energy through the equation of state for an ideal gas,

$$p = (\gamma - 1)[e - \rho(u^2 + v^2)/2] \tag{14}$$

For turbulent flow solutions the eddy viscosity μ_T is obtained by the turbulence model and instead of μ, $\mu + \mu_\mathrm{T}$ is used.

The oscillatory motion is incorporated in the governing equations. The governing equations are written in conservation law form for fixed reference frame (x_0, y_0, t). Let $\mathbf{r}_0(t)$ and $\boldsymbol{\Omega}(t)$ be the position vector of the origin and the angular velocity of a rotating frame (x, y) relative to the fixed frame (x_0, y_0). The velocity $\mathbf{v}$ of the moving frame relative to the fixed frame is

$$\mathbf{v} = \mathbf{r}_0(t) + \boldsymbol{\Omega}(t) \times \mathbf{r} = \mathbf{v}_0 + \boldsymbol{\Omega}(t) \times \mathbf{r} \tag{15}$$

where $\mathbf{v}_0$ is the velocity relative to the rotating system and $\boldsymbol{\Omega}(t) \times \mathbf{r}$ is the rotational velocity. When the motion is reduced to pure rotation then $\mathbf{v}_0(t) = 0$. In the general case of a rotating reference frame, such as a helicopter rotor in flight, we have to add the Coriolis force $\mathbf{f}_\mathrm{C} = 2(\boldsymbol{\Omega} \times \mathbf{v})$ and the centrifugal force $\mathbf{f}_\mathrm{c} = -\boldsymbol{\Omega} \times (\boldsymbol{\Omega} \times \mathbf{r}) = \Omega^2 \bar{R}$ where $\bar{R}$ is the component of the position vector perpendicular to the rotation axis. These forces modify the momentum and energy equations. For body rotation around the z-axis with $\boldsymbol{\Omega}(t) = (0, 0, \omega_z)$ and no translation $\mathbf{v} = \omega_z(y\mathbf{e}_x - x\mathbf{e}_y)$. Here $\mathbf{e}_x$ and $\mathbf{e}_y$ are the unit normals along $x -$ and

y-directions, respectively. The rotational speed ω_z is obtained from the type of motion prescribed as $\omega_z = \mathrm{d}\alpha/\mathrm{d}t$. The reduced frequency parameter is defined as either $k = \omega c/2U_\infty$, or $\pi fc/U_\infty$ where f is the frequency of oscillation and U_∞ is the free-stream velocity. Then $\dot{\alpha} = \omega_z = \alpha_1(2kU_\infty/c)\cos[(2kU_\infty/c)t]$ for $\alpha(t) = \alpha_0 + \alpha_1 \sin([2kU_\infty/c]t)$ where α_0 is the mean angle of oscillation and α_1 is the amplitude of the pitch motion.

Over the years, various methods for the numerical solution of the compressible flow equations have been developed. The most commonly used methods for the investigation and prediction of dynamic stall flows are summarized in Appendix A.

4.4.2. *Incompressible flow equations*

For dynamic stall occurring at free-stream speeds $M_\infty \leqslant 0.2$, compressibility effects are negligible even at the airfoil leading edge when the angle of incidence increases. Several experimental investigations have been conducted in water tunnels and low-speed wind tunnels. In addition, there are some problems of practical interest such as dynamic stall of wind turbine blades, where $M_{\mathrm{tip}} \approx 0.2$ and the flow is practically incompressible. Numerical simulation of these flowfields requires the solution of incompressible flow equations. Various incompressible formulations have been used for dynamic stall computations. These formulations and the corresponding numerical techniques are presented in the following sections.

The primary problem with time-accurate solutions of the incompressible flow equations is the difficulty of coupling changes in the velocity field with changes in the pressure field while satisfying the continuity equation. The incompressible flow equations include pressure in a non-time-dependent form because the continuity equation has a non-evolutionary character. The non-time-dependent form of pressure is the source of difficulties of numerical schemes which must treat continuity with special techniques. The alternative streamfunction/vorticity and vorticity/velocity formulations of the incompressible flow equations do not have the same problems as the primitive variable formulation but their application is straightforward only for two-dimensional flows. Numerical solutions of primitive variable formulations are obtained either with the pressure Poisson method[73] or with fractional time-step methods.[27,92] The pressure Poisson method utilizes a Poisson equation in pressure, which is formed from the momentum equations. It advances the velocity field in time using the momentum equations and subsequently solves the Poisson equation for the pressure at the current time level so that continuity is satisfied at the next time level. The pressure Poisson method couples, therefore, velocity and pressure indirectly. The fractional time-step method, introduced by Chorin,[28] first solves for an intermediate velocity field from the momentum equations and then obtains the pressure field which will map the intermediate velocity into a divergent-free velocity.

As an alternative to the above two methods the artificial compressibility or pseudocompressibility method can be used. This method was initially introduced by Chorin[27] for the solution of steady-state incompressible flows, and it was also extended[110] to time-accurate incompressible flow solutions. The artificial compressibility formulation can be utilized for the solution of unsteady flows when a pseudo-time derivative of pressure is added to the continuity equation. This term directly couples the pressure with velocity and allows to advance the equations in physical time by iterating until a divergent-free velocity field is obtained at the new physical time level. The pseudocompressibility method has been utilized successfully for the solution of high Reynolds number, two-[130] and three-dimensional[131] steady and unsteady flows and it appears to be a promising method for the solution of incompressible dynamic stall flows.

4.4.2.1. *Velocity–vorticity formulation*

The velocity–vorticity formulation of the incompressible Navier–Stokes equations has been utilized by Wu[164–168] and his collaborators for the solution of unsteady viscous flow

problems. This formulation is as follows:

$$\nabla \cdot \mathbf{v} = 0$$

$$\nabla \times \mathbf{v} = \boldsymbol{\omega}$$

$$\frac{\partial \boldsymbol{\omega}}{\partial t} = -(\mathbf{v} \cdot \nabla)\boldsymbol{\omega} + (\boldsymbol{\omega} \cdot \nabla)\mathbf{v} + \nu \nabla^2 \boldsymbol{\omega} \tag{16}$$

where $\mathbf{v}$ and $\boldsymbol{\omega}$ are the velocity and vorticity vectors, respectively, and ν is the kinematic viscosity. The vorticity transport equation relates the left-hand side time evolution of vorticity to the physical processes of convection, stretching and rotation, and vorticity diffusion included on the right-hand side. This equation along with the continuity equation and the vorticity definition complemented with initial and boundary conditions for velocity uniquely determine the time-dependent flowfield. Furthermore, the continuity equation and the definition of vorticity describe the kinematics, e.g. the relationship between the vorticity and the velocity field at the same instant of time. The kinetics are described by the vorticity transport equation.

4.4.2.2. Vorticity/streamfunction formulation

The vorticity/streamfunction formulation is limited to two–dimensional flows and requires the definition of a streamfunction Ψ as $u = \partial\Psi/\partial y$, $v = -\partial\Psi/\partial x$. Then the vorticity ω_z is obtained by

$$\omega_z = -\nabla^2 \Psi \tag{17}$$

This equation and the vorticity transport equation constitute the vorticity/streamfunction formulation which has been utilized by Ghia *et al.*[64] for the solution of incompressible two-dimensional dynamic stall flows. In these investigations the following streamfunction along with the appropriate boundary conditions for a moving reference frame was implemented

$$\Psi = y + \Psi_0 + \Psi_D \tag{18}$$

In this equation, y is the vertical coordinate, Ψ_0 an integration constant representing instantaneous displacement of the zero streamline at infinity due to the inviscid lift generation, and Ψ_D a disturbance streamfunction due to deviation from uniform flow. In the vorticity–streamfunction formulation the pressure does not appear explicitly and can be computed from the following Poisson pressure equation, obtained by taking the divergence of the momentum equation:

$$\nabla \cdot \left[\frac{\partial \mathbf{v}}{\partial t} + \mathbf{v} \cdot \nabla \mathbf{v} + \boldsymbol{\Omega}(t) \times \mathbf{v} + \frac{1}{\mathrm{Re}} (\nabla \times \boldsymbol{\omega}) \right] = -\nabla \cdot (\nabla p) \tag{19}$$

Numerical methods for the solution of the incompressible flow governing equations are summarized in Appendix B.

4.4.2.3. Pseudo-compressibility formulation

The pseudo-compressibility formulation of the incompressible flow equations presented here is based on the conservative form of the incompressible flow equations in curvilinear coordinates:

$$\partial_\xi \left(\frac{U}{J} \right) + \partial_\eta \left(\frac{V}{J} \right) = 0$$

$$\partial_t \hat{u} = -\partial_\xi (\hat{f} - \hat{f}_v) - \partial_\eta (\hat{g} - \hat{g}_v) = -\hat{r} \tag{20}$$

where $\hat{u} = (u, v)^{\mathrm{T}}/J$, $U = \xi_x u + \xi_y v$, $V = \eta_x u + \eta_y v$, and $\hat{f}, \hat{f}^v$ the inviscid and viscous fluxes, respectively, given by

$$\hat{f} = \frac{1}{J}\begin{pmatrix} \xi_x p + uU + \xi_t u \\ \xi_y p + vU + \xi_t v \end{pmatrix}, \quad \hat{g} = \frac{1}{J}\begin{pmatrix} \eta_x p + uV + \eta_t u \\ \eta_y p + vV + \eta_t v \end{pmatrix}$$

$$\hat{f}_v = \frac{1}{J}\begin{pmatrix} m_1 u_\xi + m_3 u_\eta \\ m_1 v_\xi + m_3 v_\eta \end{pmatrix}, \quad \hat{g}_v = \frac{1}{J}\begin{pmatrix} m_3 u_\xi + m_2 u_\eta \\ m_3 v_\xi + m_2 v_\eta \end{pmatrix}$$

$$m_1 = \xi_x^2 + \xi_y^2, \quad m_2 = \eta_x^2 + \eta_y^2, \quad m_3 = \xi_x \eta_x + \xi_y \eta_y$$

The artificial compressibility or pseudocompressibility formulation is obtained from the original incompressible flow equations by introducing an additional time derivative of pressure to the continuity equation as

$$\frac{\partial p}{\partial \tau} = -\beta \nabla \cdot \hat{\mathbf{U}} = -\beta \left[\frac{\partial}{\partial \xi}\left(\frac{U}{J}\right) + \frac{\partial}{\partial \eta}\left(\frac{V}{J}\right) \right] \tag{21}$$

Addition of this fictitious pressure derivative enables full coupling of the continuity with the momentum equations and significantly facilitates the numerical solution. In Equation (21), τ does not represent physical time, therefore in the momentum equation t is replaced by τ, and the pseudocompressible form of the governing equation is

$$\frac{\partial \hat{\mathbf{Q}}}{\partial \tau} + \frac{\partial \hat{\mathbf{F}}}{\partial \xi} + \frac{\partial \hat{\mathbf{G}}}{\partial \eta} = \frac{1}{\mathrm{Re}}(\hat{\mathbf{F}}_v + \hat{\mathbf{G}}_v) \tag{22}$$

where $\hat{Q}$ is the solution variable vector and $\hat{F}$, $\hat{G}$ are the inviscid fluxes given by

$$\hat{\mathbf{Q}} = \frac{1}{J}\begin{pmatrix} p \\ u \\ v \end{pmatrix}, \quad \hat{\mathbf{F}} = \frac{1}{J}\begin{pmatrix} \beta U \\ uU + \xi_x p + \xi_t u \\ vU + \xi_y p + \xi_t v \end{pmatrix}, \quad \hat{\mathbf{G}} = \frac{1}{J}\begin{pmatrix} \beta V \\ uV + \eta_x p + \eta_t u \\ vV + \eta_y p + \eta_t v \end{pmatrix}$$

In these equations, τ is referred to as pseudo-time which can be considered as a time-iteration parameter. Steady-state incompressible solutions are obtained with the artificial compressibility method by time marching as in the compressible case. The numerical methods for the solution of the pseudo-compressible equations are very similar to the methods used for the solutions of the compressible flow equations. At convergence, however, the time derivative of pressure and consequently the divergence of the velocity approach zero. The parameter β which is referred to as the artificial compressibility or pseudo-compressibility parameter, usually takes a value between 1 and 5, but larger values may be required for solutions on highly stretched grids. The value of β in these cases is adjusted accordingly so that optimal convergence is obtained. Numerical methods for the solution of the artificial compressibility form of the incompressible flow equations are summarized in Appendix B.

4.5. NUMERICAL SCHEMES

The compressible flow equations are discretized either by the finite-difference or the finite-volume approaches. Time integration is performed either by explicit or implicit numerical schemes. Explicit schemes are more computationally efficient and they have an advantage for parallel computer applications, but numerical stability limitations impose small time steps for time integration. As a result, most unsteady flow computations have been performed with implicit integration schemes which allow much larger time steps at the expense of the solution of systems of linear equations. Among the implicit integration schemes presented in the literature one of the most popular methods for implicit time

integration is the second-order accurate, approximately factorized Beam–Warming algorithm.[7] The standard centered and upwind-biased schemes based on this algorithm are presented in Appendix A. As an alternative to the Beam–Warming algorithm,[7] which requires block tridiagonal matrix inversions, several investigators utilized other algorithms in order to reduce the computational time. Chaderjian[20] used the diagonal form of the Beam–Warming algorithm which is first-order-accurate in time for unsteady solutions for the wing–rock problem of a delta wing. Srinivasan *et al.*[142] used an LU–SGS scheme to obtain solutions for a lifting rotor in hover. Hixon and Sankar[81] used the generalized minimal residual (GMRES) method in an attempt to reduce computational time of unsteady two-dimensional solutions.

4.6. TURBULENCE MODELS

Understanding and prediction of turbulent flows has been and still is a problem of continuous interest in fluid dynamics. In the past few decades (see Refs (148, 8)), several turbulence models have been developed for flows of general interest and for aerodynamic flows. Dynamic stall occurring on helicopter blades and wings always involves high Reynolds number turbulent flow. As in other fields of aerodynamics, numerical investigations of dynamic stall must deal with turbulent flow calculation. Progress in algorithms and high-resolution total variation diminishing (TVD) and essentially non-oscillatory (ENO) schemes achieved over the last few years together with the enormous increase in computing capacity enable very detailed simulations with dense meshes and very accurate time and space resolution. It appears, however, that numerical simulations will only contribute to a better understanding of dynamic stall mechanisms and improvements in predictive ability if progress in numerical schemes is paced directly by an improved ability in resolving turbulent flow. Also modeling of transitional flow regions, which play a critical role in the overall flowfield development, is important.

Turbulence is characterized by irregular motions resulting from the non-linear growth of instabilities and occurs when the local Reynolds number exceeds a critical value. Turbulent motions are three-dimensional and include a wide range of space and time scales, which proliferate with increasing Reynolds number. A detailed computation of all scales existing in turbulent motions, which are fully described by the Navier–Stokes equations without additional external information, imposes enormous requirements in computing speed and storage capacity. These computations were performed only for very low Reynolds numbers and simple flow configurations in direct numerical simulation (DNS), where all significant eddy sizes down to the Kolmogorov scale were resolved. DNS is not expected to play a role for the investigation of dynamic stall due to the enormous computing resources they require and because they are limited to simple flow geometries. Numerical investigation of practical flows requires to model small eddy motions that cannot be resolved in space and time and therefore require some kind of turbulence modeling. There are two types of turbulence models applied to the solution of practical aerodynamic flow problems, "subgrid modeling" in the full Navier–Stokes simulations and statistical turbulence modeling, commonly referred to as turbulence modeling, in the Reynolds averaged equations.

Subgrid modeling is applied to large eddy simulations (LES), which are three-dimensional, unsteady, full Navier–Stokes simulations performed with very high grid resolution and very accurate time and space algorithms. LES simulations resolve scales that are sufficiently large and have a long enough lifetime with the mesh, and the behavior of small unresolved scales is described by the subgrid model. The computational requirements for LES even for simple, steady airfoil flows are very high. However, LES have a potential in improving dynamic stall calculations because they resolve the large eddies which are unique for this type of flow condition and because they rely on the model only for the smaller scales of turbulence. These smaller turbulence scales behave in a statistically universal way and recent progress in subgrid modeling has yielded very encouraging improvements.

Statistical turbulence modeling is applied in the Reynolds-averaged simulations which are obtained by ensemble averaging of the Navier–Stokes equations where all quantities are expanded as mean motions plus turbulent fluctuations. The averaging destroys the dynamic information of turbulence but retains the statistical behavior of the lowest moments which affect the mean motion. Reynolds–averaged computations with a turbulence model do not capture the real-time and space characteristics of turbulence, but they achieve enormous computational savings compared to DNS and LES. They do not need to be time accurate and they can be used for two-dimensional calculations. Many of the turbulence models used in boundary layer and Navier–Stokes codes do not include time terms. These models, strictly speaking, are appropriate only for steady flow computations. However, algebraic models with no time dependency have been used quite successfully for unsteady aerodynamic solutions. Other models, such as the two–equation models include unsteady terms, but they are not actually intended to capture the unsteady behavior of the small–scale turbulent motions. All of these models have been developed for steady flows and there is no model designed for modeling unsteady turbulent flows. On the other hand, the unsteadiness of the mean motion occurs at time scales much slower than the turbulent flow fluctuations. As a result, the same turbulence models originally developed for steady turbulent flows are used for unsteady flow calculations without any modification.

Presently, only the use of the Reynolds-averaged equations can only be considered as a research and design tool for practical aerodynamic flows. The Reynolds-averaged equations include the velocity correlation terms or apparent momentum fluxes. These fluxes are unknown *a priori* and act as apparent stresses throughout the flowfield. They are referred to as Reynolds stresses and they represent the quantities through which turbulence affects the mean motion. Additional equations derived for these stresses include additional unknown moment fluctuations. This proliferation of unknown moments which occurs as equations are written for lower-order moments is called the "closure problem of turbulence". The source of the closure problem is the non-linearity of the governing equations. The function of turbulence modeling is to devise approximations of the unknown correlation terms or stresses in terms of known flow properties in order to obtain a sufficient number of equations to close the system. Turbulence models for use in general engineering applications are required to involve a minimum amount of complexity while they are able to capture the essence of the important and relevant physics. In this spirit, several turbulence models ranging from simple algebraic, which give the turbulent eddy viscosity by a simple algebraic formula, to models consisting of one or more differential equations have been developed over the years. In this section, the essential equations for the implementation of various models as well as the important characteristics of these models used to date in dynamic stall computations are described. The interested reader can find more details in the cited original references.

It has to be emphasized that none of the models presented here has been calibrated for dynamic-stall-type flows. Testing and validation for new flow conditions of interest is therefore important and necessary. It should not come as a surprise that some models proven accurate for other flows might be shown to be insufficiently accurate for engineering purposes in dynamic-stall simulations. The availability of detailed measurements is an invaluable aid in proving the adequacy and accuracy of a model, identifying the strong and weak points of a turbulence model under validation. Unfortunately, most dynamic-stall experiments include only integrated loads, such as lift, drag and pitching moment coefficients. Some experimental investigations[103] include more detailed measurements, such as surface pressure coefficients and skin friction. Recent experimental investigations[24] provide LDV flow measurements and velocity correlations. Continuous testing and validation of turbulence models should be conducted with newly obtained experimental data because the availability of turbulence measurements for the flow of interest can only identify parts of the model that need improvement or readjustment of parameters. Turbulence models used in numerical predictions and investigations of dynamic stall flows are briefly summarized in Appendix C.

4.7. TRANSITIONAL FLOW MODELING

The effect of turbulence and some of the models used for the prediction of turbulent flow behavior for airfoils and wings undergoing dynamic stall were described in the previous section. It was emphasized that most dynamic stall flows include a transitional flow regime unless they are tripped at the leading edge. A complete theory for transition does not exist to date. As a result, progress in turbulent flow modeling and prediction is more advanced compared to available methods for transition location prediction and modeling of transitional flow behavior.

Detailed descriptions of transitional flow physics and the factors which influence and promote laminar flow transition, such as acoustic excitation, receptivity to free-stream turbulence, etc., are discussed in reports by Morkovin,[113,114] Arnal,[2] Reshotko,[125] Reed *et al.*[123] and Herbert.[76] Physically, the transitional flow regime is characterized by a large disparity of scales. The traditional approaches to treat this wide range of scales, applied with success in turbulent flows, such as large eddy simulation or Reynolds averaging, are of little help to model transitional flows. The main reason is that averaging over an intermediate period of time (short enough compared to the time scale of unsteady motion) or spatial filtering over intermediate scales destroys disturbances relevant to transition, such as Tollmien–Schlichting (TS) waves which have long wavelengths and move slowly. For this reason, the flow variables V are decomposed as $V = V_0 + V'$, e.g. to a basic flow component V_0 plus an unsteady deviation or disturbance, V', from the basic flow. These flow components are inserted into the governing equations and, since transitional flow fluctuations are small, products of fluctuations are discarded. The system describing the basic flow is satisfied identically and a second system is obtained that governs the evolution of the disturbances V', and has coefficients which are functions of the basic flow equation variables. A comprehensive and fairly complete review of the mathematical stability theory is given by Mack.[104] Detailed analyses are also presented in books.[35,97,137,161]

Transitional flow over an airfoil is shown schematically in Fig. 18. From a practical point of view, determination of two positions is important: (1) the point of instability x_i, where unstable TS waves first appear, and (2) the transition onset point x_{tr}, where the flow becomes fully turbulent. The final goals of flow stability theory and transitional flow research are to predict unambiguously x_i and x_{tr} and to provide a method for accurate computation of the transitional flow region $(x_{tr} - x_i)$, without having to resort to a complete resolution of all scales which are fully described only by the full Navier–Stokes equations. Towards this end, DNS transitional flow investigations,[122] which can be performed only for very simple configurations with idealized boundary conditions, are prohibitively expensive and therefore can serve only as a research tool. Current understanding of transition is based on the analysis of the growth of small disturbances, which are assumed to be small enough so that quadratic terms can be neglected, and the problem can be described by linearized partial differential equations (PDEs). The linearized PDEs can be further simplified to ordinary differential equations (ODEs) by assuming normal-mode solutions with the parallel-flow approximation, which neglects the weak growth of the boundary-layer and normal velocity component.

Linear stability results, such as amplification rates and stability curves, can be obtained with the linear stability code COSAL,[105] in its incompressible or compressible form, where the parallel flow assumption is employed and the linearized PDEs are reduced to ODEs by assuming wave-like disturbances as

$$\xi(x, y, z, t) = \hat{\xi}(z)\, e^{(\alpha x + \beta y - \omega t)} \tag{23}$$

where $\hat{\xi}$ is the disturbance wave function, α, β are the disturbance wave numbers along the streamwise x and spanwise y directions, respectively, and ω is the disturbance frequency. The linear ODEs along with the homogeneous boundary conditions constitute an eigenvalue problem of the form

$$\alpha = \alpha(\beta, \omega) \tag{24}$$

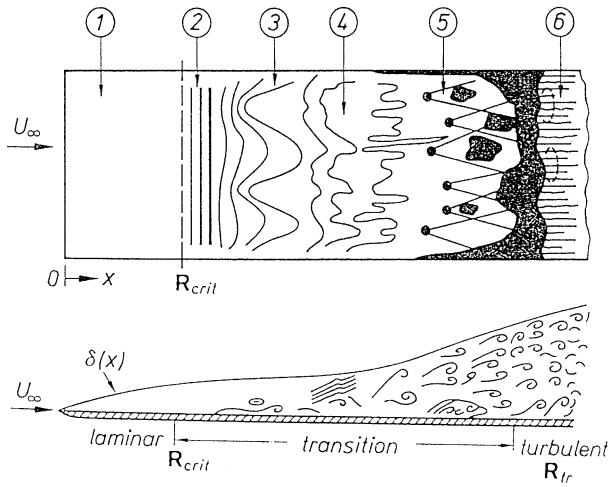

Fig. 18. Schematic of airfoil leading edge transitional flow [from Ref. (161)], where $x_i = R_{\text{crit}}$ and $x_{\text{tr}} = R_{\text{tr}}$ (1) laminar flow (6) fully turbulent flow, and (2)–(5) stages of transition.

The solution of this problem is obtained in the general compressible flow case from the solution of the following system of five ODEs in $\bar{\Phi} = [\alpha\hat{u} + \beta\hat{v}, \hat{w}, \hat{p}, \hat{T}, \alpha\hat{v} - \beta\hat{u}]$,

$$\left(A\frac{\mathrm{d}^2}{\mathrm{d}z^2} + B\frac{\mathrm{d}}{\mathrm{d}z} + C\right)\bar{\Phi} = 0 \tag{25}$$

where A, B, C are matrix coefficients given by Mack.[104]

For the incompressible two-dimensional flow case the stability equation is the familiar Orr–Sommerfeld equation[137] as follows:

$$\left[\left(\frac{\mathrm{d}^2}{\mathrm{d}z^2} - \alpha^2\right)^2 - \mathrm{iRe}(\alpha U - \omega)\left(\frac{\mathrm{d}^2}{\mathrm{d}z^2} - \alpha^2\right) + \mathrm{iRe}\,\alpha\frac{\mathrm{d}^2 U}{\mathrm{d}z^2}\right]\bar{\phi} = 0 \tag{26}$$

This equation with appropriate homogeneous boundary conditions again constitutes an eigenvalue problem, whose solution can be obtained much faster than for the general compressible flow case.

Linear stability theory predicts the point of instability as the location where TS waves appear. Transition occurs downstream from the point of instability. The transition location is obtained with the empirical e^N method where the exponent N is given as

$$N = \ln(A/A_0) = \int_{x_{\text{inst}}}^{x_{\text{tr}}} -\alpha_i \,\mathrm{d}x \tag{27}$$

where α_i represents the amplification rate determined from the solution of the eigenvalue problem of Equations (25) or (26) and A_0 is the amplitude of the disturbance at the onset of instability and A is the disturbance amplitude at some downstream location. The onset of transition is assumed to occur when N reaches a value in the range between 9 and 11. The e^N method is a linear theory prediction for the transition location x_{tr} which does not account for non-linear interactions and turbulent spot formation.

Evolution of disturbances where boundary-layer growth and other effects, such as curvature, are taken into account requires the solution of the full system of linearized PDEs. However, for boundary-layer-type flows, these equations have an elliptic character along the flow direction which arises from the upstream propagation of acoustic waves and streamwise viscous diffusion. Therefore, the solution cannot be obtained with marching methods. The linearized PDEs can become parabolic by suppressing the upstream propagation. Parabolization of the stability equations was achieved by Herbert,[75,76] and Bertoloti[6] by decomposing a disturbance into a rapidly-varying, wave like part and a slowly

growing shape function as follows:

$$\Phi(x, y, z, t) = \Psi(x, y)\, e^{i\left(\int_{x_0}^{x} \alpha(\bar{x})\, dx + \beta y - \omega t\right)} \tag{28}$$

where Ψ is the shape function vector $\Psi = (\hat{\rho}, \hat{u}, \hat{v}, \hat{w}, \hat{T})^{T}$. In this manner the ellipticity is retained for the wave part and the parabolization is applied to the shape function. The resulting parabolized stability equation (PSE) is solved by marching along the streamwise direction and it is valid for both linear and non-linear evolution of convective disturbances in spatially growing boundary layers.

The linear stability analysis and the PSE methods make it possible to isolate the basic flow computation as a separate task. However, the computation of the basic flow in the critical region, e.g. the laminar transitional flow region and the interface of the transitional with turbulent flow region is very demanding. The numerical grid in the critical region must be very smooth without sudden variations, otherwise the sensitive stability equations behave in a peculiar manner and they may exhibit numerical artifacts falsifying the physics. Furthermore, the flow variables and their derivatives must be resolved adequately using high-order accurate numerical schemes.

The flow in the region between transition point and fully developed turbulent flow is quite complex. It is characterized by amplification of disturbances (Tollmien–Schlichting waves), development of spanwise vorticity, which eventually breaks down to three-dimensional vorticity fluctuations, followed by turbulent spot formation which coalesces to fully developed turbulent flow. It has been observed, however, that an adverse pressure gradient may short–circuit some of the above phenomena because of flow separation or extreme instability. For example, a separation bubble forms and reattaches downstream in a fully turbulent flow without intermediate spot formation. In practice, calculation of the full extent of the transitional flow region can only be achieved with a transition model. From a practical, engineering point of view linear stability analysis in conjunction with the empirical e^N method provides only the transition location. PSE calculations[78,25] yield instability and transition points as part of the solution and allow continuation of the computation in the transitional flow region[78] up to the point where the amplitude of disturbances remains small enough. Results from linear stability theory and recently obtained PSE solutions are presented in the following sections. In practice, transitional flow results have been mainly obtained with transition models.

Linear stability computations applied to realistic three-dimensional configurations[82,141] yield the transition location with the e^N method for N factor values between 9 and 11 which is valid for atmospheric flight conditions. However, variation of free-stream turbulence level $T = \sqrt{\overline{u'^2}}/U_\infty$, and adverse pressure gradient conditions may significantly change the N factor value. The locus of the transition points obtained with the e^N method for a delta–wing configuration[82] is shown in Fig. 19. In this figure, each trace represents

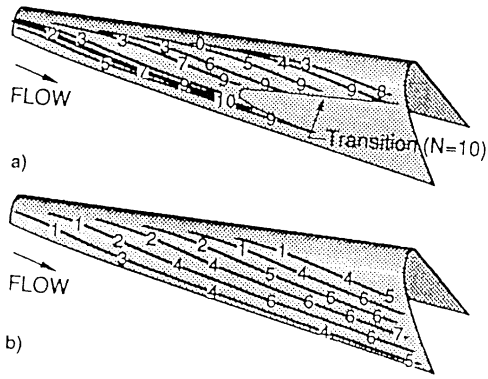

Fig. 19. Locus of flow transition computed with the e^N method [(from Ref. (82)].

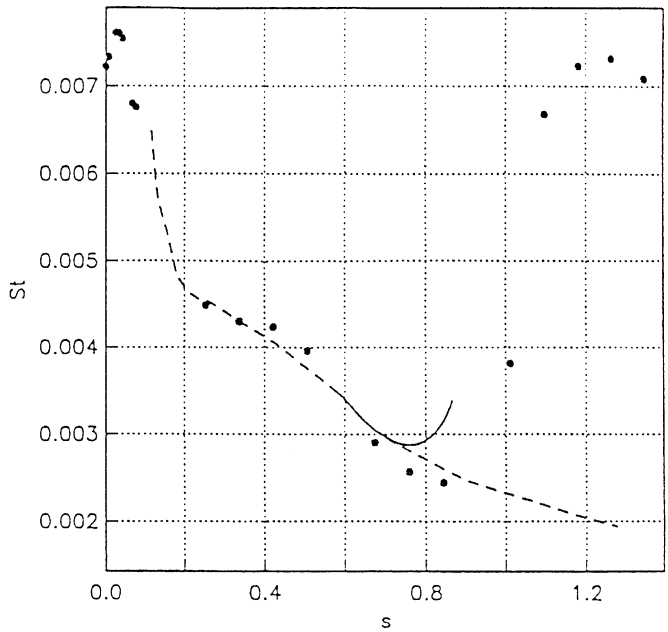

Fig. 20. Variation of the Stanton number with the arc length s along the blade upper surface [from Ref. (78)].

a series of eigenvalue calculations at approximately 20 streamwise locations. The traces terminate when N reaches the value of 10 and transition takes place.

The PSE method was used for boundary-layer-type flows and the computed results were in very good agreement with DNS simulations. The capability of the PSE method to correctly predict the effects of free-stream turbulence levels, curvature, pressure gradient and wall heating on the transition process was demonstrated.[78] The computed variation of the Stanton number for a stator blade is compared with the UTRC measurements in Fig. 20. The basic flow was computed with a boundary-layer code. The PSE computations were carried out for the unstable region and the results are in good agreement with the experiment. The transition onset point was predicted at $s = 0.764$, slightly upstream of the experimental location. The PSE computation was continued until $s \approx 0.9$ where disturbance amplitudes of the order of 10% were reached. It is also reported in Ref. (77) that calculation of the N factor from the onset of instability near $s = 0.15$ up to the experimental transition onset point at $s = 0.8$ yields an unrealistic value of $N \approx -13$, and when $s = 0.6$ is considered as point of instability the N factor value is $N \approx 3.5$. Therefore, application of the e^N method for cases where the flow conditions are very different from free flight conditions characterized by low turbulence intensities may lead to errors, because the value of the amplification factor is 9 only for these conditions.

For unsteady flow predictions, the cost of both the compressible stability and the PSE method are significant. Results for incompressible transitional flows over airfoils with separation bubbles were obtained in Ref. (13). The transition location was obtained with the e^N method. The Chen–Thyson[26] empirical intermittency formula was used for the calculation of the transitional flow region. The mean flow was computed with an interactive boundary-layer code. A comparison of the computed and measured velocity profiles, pressure distributions and momentum thickness distribution for the incompressible flow over the ONERA-D airfoil at Reynolds number 3×10^5 and zero angle of attack is shown in Figs 21–23. The computations are in very good agreement with the experiment. The computational cost of this method is quite low. It appears, therefore, that calculations at the low Mach number limit, where the compressibility effects are small, with the incompressible stability equation similar to the steady-state calculations in Ref. (13) would be the rational first step for transition location prediction in dynamic stall flows. The problem of the

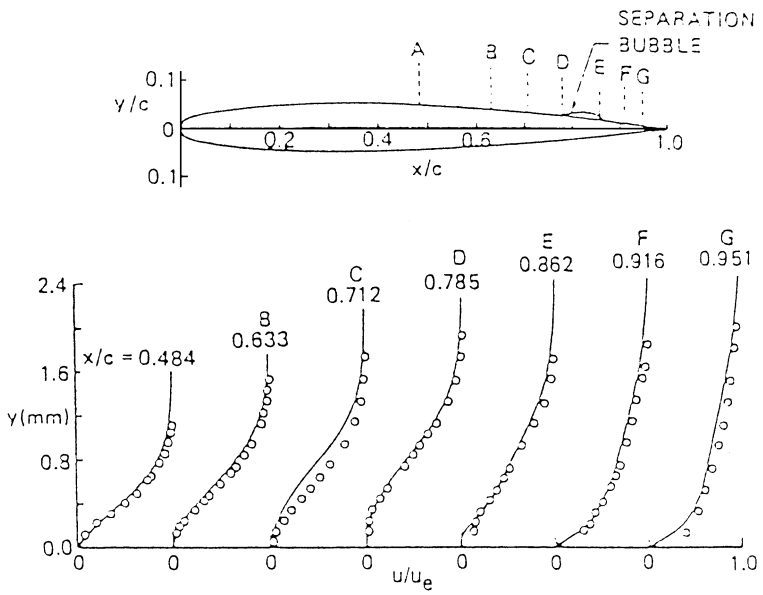

Fig. 21. Comparison of the calculated (solid lines) and measured (symbols) velocity profiles for ONERA-D airfoil for $\alpha = 0°$. $Re_c = 3 \times 10^5$ [from Ref. (13)].

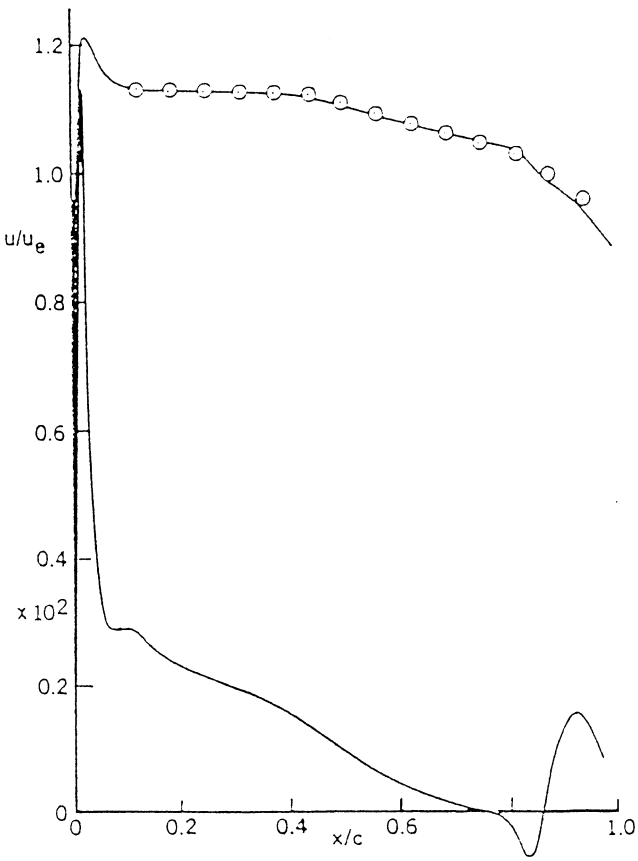

Fig. 22. Comparison of the calculated (solid lines) and measured (symbols) boundary layer edge velocity distribution for ONERA-D airfoil for $\alpha = 0°$. $Re_c = 3 \times 10^5$ [from Ref. (13)].

e^N method transition location predictions with large turbulence levels, adverse pressure gradients or curvature must be carefully addressed. Appropriate values of N factor must be chosen for the unsteady calculations based on experiments.

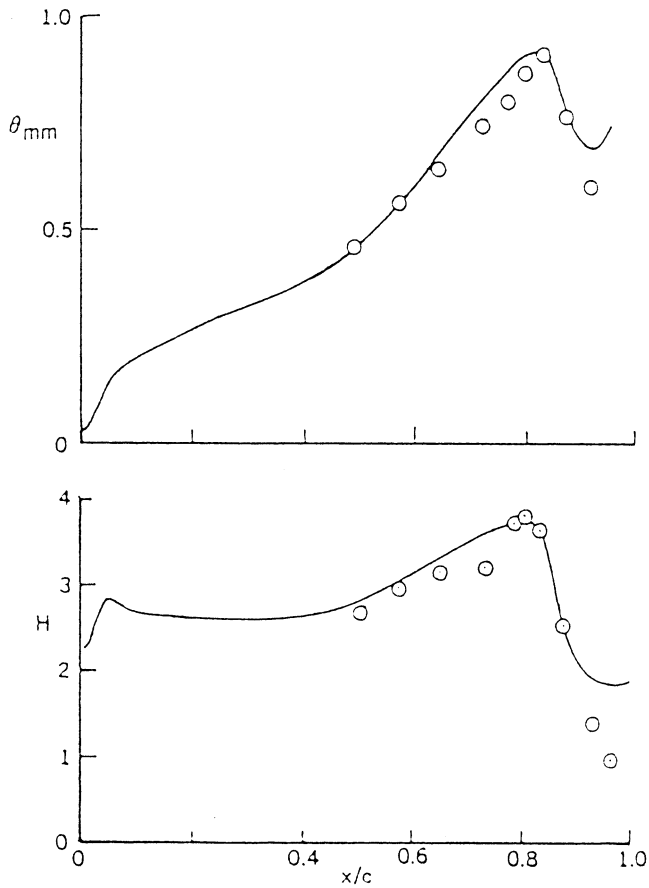

Fig. 23. Comparison of the calculated (solid lines) and measured (symbols) momentum thickness θ and shape factor H values for the upper surface of the ONERA–D airfoil; $\alpha = 0^\circ$ $\mathrm{Re}_c = 3 \times 10^5$ [from Ref. (13)].

Computations with transition models presented recently[33] for steady airfoil flows required the transition location as an input parameter. The transition location can be obtained by measurements and input directly in the model for the steady case. For dynamic stall and unsteady flows, experimental acquisition of transitional flow measurements is difficult and it is imperative that either linear stability theory method with appropriate N factor value or the PSE method is used for unambiguous prediction of transition location in spite of the computational cost.

Computations of transition of the Blasius flow over a flat plate was obtained in Ref. (172) by specifying the transition onset and with a transition model which represents the mean streamwise velocity in the transitional region using an intermittency factor γ as $U_{\mathrm{tr}} = \gamma U_{\mathrm{tur}} + (1 - \gamma)\, U_{\mathrm{lam}}$. The transitional region fluctuation consists of three contributions as

$$\overline{(u_i' u_j')}_{\mathrm{tr}} = \gamma \overline{(u_i' u_j')}_{\mathrm{tur}} + (1 - \gamma)\overline{(u_i' u_j')}_{\mathrm{lam}} + \gamma(1 - \gamma)\Delta U_i \Delta U_j$$

where the first contribution is the turbulent component, the second is the non-turbulent contribution due to TS waves, and the third contribution is from the large eddies. Turbulent flow contributions in Ref. (172) are obtained with a one-equation turbulence model. The computed solutions confirmed that skin friction and velocity profiles in agreement with the measurements can be obtained by taking into account only the turbulent contribution. However, in order to obtain the full spatial evolution of the intensities, $\overline{u'^2_{\mathrm{tr}}}$, it is necessary to consider both TS contributions which improve predictions of the early stage, and large eddies which improve predictions of the spikes in streamwise intensities. These results

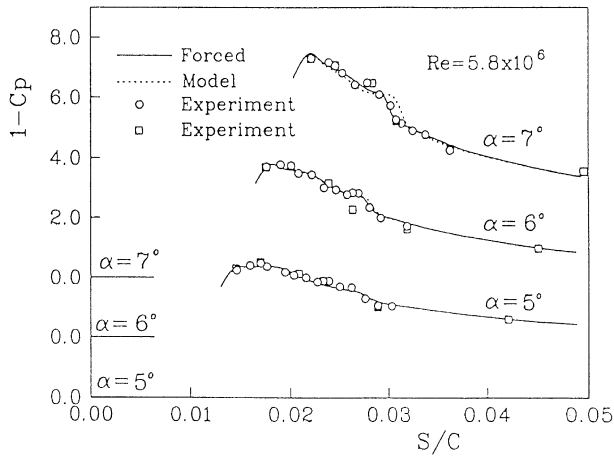

Fig. 24. Pressure distribution on the modified NACA 0010 section at $\alpha = 8°$ for various Reynolds numbers [from Ref. (33)].

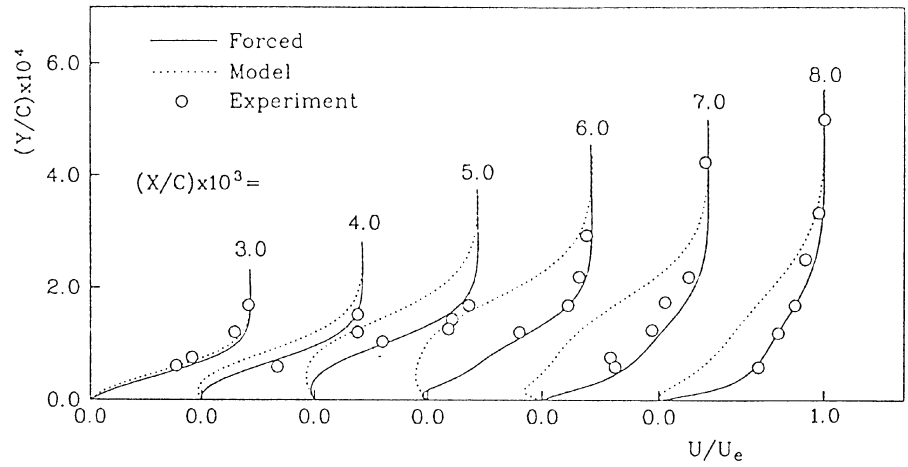

Fig. 25. Comparisons of velocity profiles on the NACA 63–009 section for $Re_c = 5.8 \times 10^6$ at $\alpha = 7°$ [from Ref. (33)].

support use of transition models based only on turbulent contributions for airfoil flows where adverse pressure gradients and high free stream turbulence intensities shorten the transition length.

In Ref. (33) the computation of the transitional flow region is carried out with a modified form of the same turbulence model used for the computation of the fully turbulent flow region. The results of this approach for steady airfoil flows[33] yield acceptable engineering accuracy. Results of the calculations of Ref. (33) for a NACA 63-009 airfoil at $Re = 5.8 \times 10^5$ and angle of incidence 8° are shown in Fig. 24. The transition point was specified to best fit the measured data. A k–ε model was implemented and an intermittency factor was used for the computation. Transition was obtained inside the separation bubble and the computed velocity profiles of Fig. 25 are in good agreement with the measurements. It remains to be verified that this is a viable approach for the dynamic case by comparison with unsteady surface pressure and skin friction measurements.

Recently, dynamic-stall computations[45] were carried out using as transition model a modified form of the turbulence model and *ad hoc* specification of the instability location at the point of maximum computed suction pressure. The Baldwin–Barth one-equation model was modified to mimic the transitional flow behavior from instability onset to fully

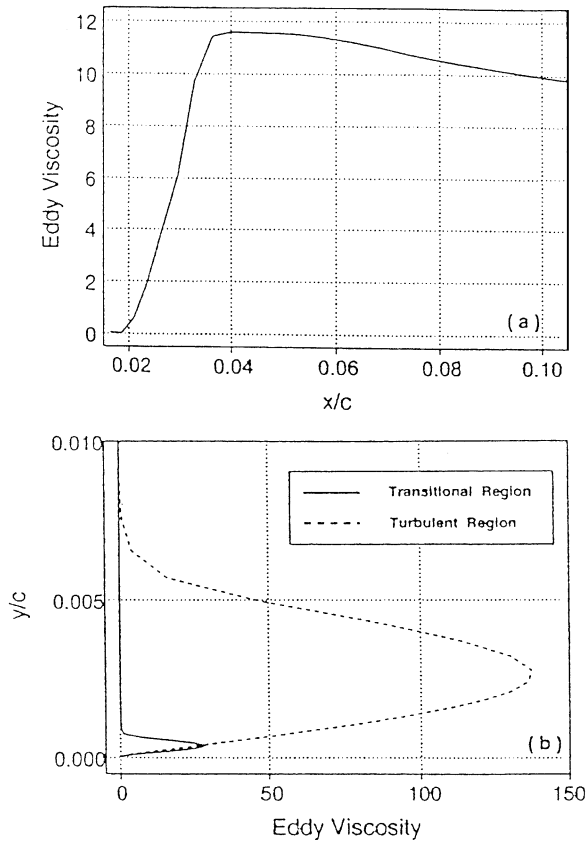

Fig. 26. Computed eddy viscosity distribution in the chordwise and normal directions [from Ref. (45)].

developed turbulent flow region. The production term of the turbulence model was forced to be zero upstream of the instability point. Gradual increase of production from zero to the fully turbulent value yield a smooth increase of an "effective eddy viscosity" in the transitional flow region. The streamwise and normal variation of the computed eddy viscosity are shown in Fig. 26. In spite of these crude approximations, the computed results[42,45] have shown very significant improvement compared to fully turbulent calculations. It appears that transitional/turbulent solutions capture the correct physics of the unsteady flowfield which are completely missed by a fully turbulent computation. It is important, therefore, that the effect of transitional flow behavior on dynamic stall be further investigated using a reliable transition location prediction criterion and a more accurate transition model. Towards this end testing of transition models in adverse pressure gradient conditions and free-stream turbulence effects which are significant at the airfoil leading edge region, where transition occurs at moderate Reynolds numbers of the order of 500,000, has been recently conducted in Refs (136, 154).

5. COMPUTATION OF STALL INITIATION

5.1. VISCOUS–INVISCID INTERACTION METHOD

Cebeci *et al.*[19] investigated the initiation of dynamic stall on a Sikorsky SSC-A09 airfoil which was subjected to a ramp-type motion with constant non-dimensional pitch rate of 0.02. The angle of attack varied from 0 to 30°. The Reynolds number was 2 million. This case was also studied experimentally by Lorber and Carta,[99] who found that a leading-edge vortex starts to form around 18–19° angle of attack whereas the steady stall angle is

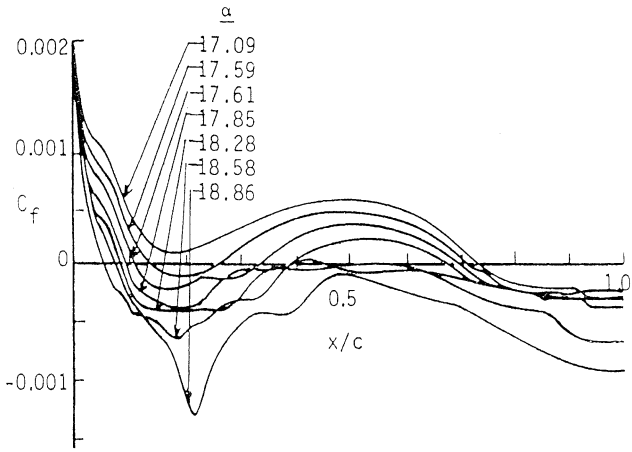

Fig. 27. Initiation of the leading-edge vortex and the trailing-edge separation on the Sikorsky airfoil subject to ramp-type motion with pitch rate of $k = 0.02$, $\mathrm{Re}_c = 2 \times 10^6$ and α varying from 0 to 30° [from Ref. (19)].

around 14°. Figure 27 shows the skin friction distributions computed by Cebeci *et al.*[19] using the viscous-inviscid interaction method described in Section 4.3.1. At $\alpha = 17.09°$ there is no leading-edge flow separation but only a trailing-edge separation which extends to about 72% chord. At the next angle of attack, $\alpha = 17.69°$, leading-edge separation takes place close to 12% chord with a bubble reattaching around 33% chord, followed by trailing-edge separation at 70% chord. The explosive nature of the leading-edge separation bubble, which is all turbulent, becomes more obvious at the next $\alpha = 17.88°$, where leading-edge separation takes place around 10% chord, but the reattachment of the bubble moves to 50% chord, causing a bubble of 40% in extent, followed by trailing-edge separation moving to 60% chord. Very shortly thereafter, in less than 1° increase in angle of attack, the leading-edge separation bubble disappears with complete flow separation taking place at around 5% chord. Hence, these calculations show that the viscous-inviscid interaction method closely predicts the data of Lorber and Carta for the Sikorsky airfoil and that, for this airfoil, the initiation of dynamic stall is caused by trailing-edge separation.

5.2. NAVIER–STOKES METHOD

Ekaterinaris *et al.*[42] and van Dyken *et al.*[154] analyzed the initiation of dynamic stall on a NACA 0012 airfoil which oscillated about a mean angle of attack of 10° with an amplitude of 2° in a flow which had a free-stream Mach number of 0.3 and a Reynolds number of 540,000. This case was studied experimentally by van Dyken and Chandrasekhara[153] and by Chandrasekhara and van Dyken[24] using point diffraction and laser velocimetry. Their experiments revealed the formation of a leading-edge separation bubble which started to form at around 8° angle of attack. Using the thin–layer Navier–Stokes equations, Ekaterinaris *et al.*[42] and van Dyken *et al.*[154] found it necessary to model the boundary-layer transition using the Chen–Thyson transition length model and specifying the transition onset location for the successful computation of the separation bubble formation. Figure 28 shows the computed and measured density contours as the airfoil pitches through an angle of attack of 10° during the upstroke. It is seen that there is satisfactory agreement. However, as explained by van Dyken *et al.*[154] the computations are quite sensitive to the proper choice of the transition onset location and to the length of the transition region.

6. TWO-DIMENSIONAL DYNAMIC STALL COMPUTATIONS

A considerable number of experimental investigations of airfoil dynamic stall for oscillatory,[103,61,120] ramp[95,98] and more complex motions[53] at various free-stream speeds

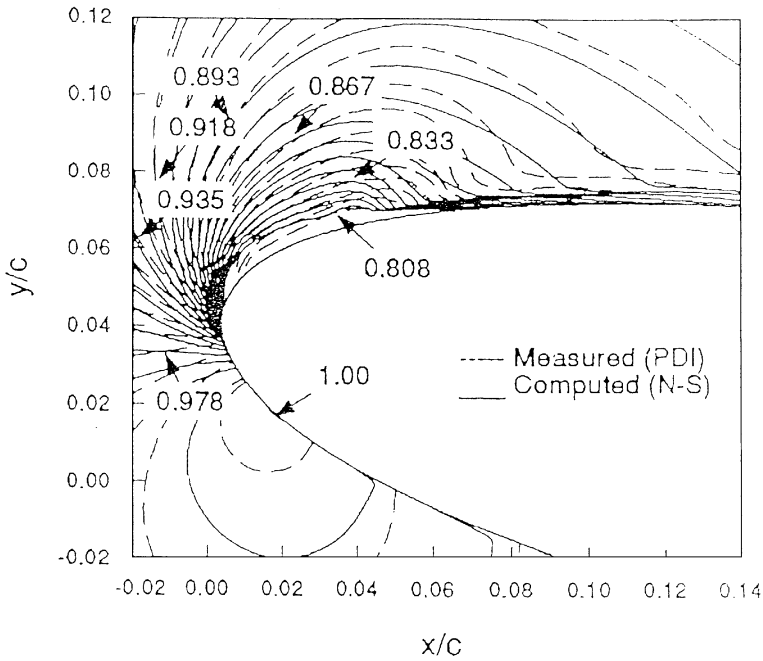

Fig. 28. Computed and measured density contours over oscillating airfoil near leading edge; $M_\infty = 0.3$, $\alpha(t) = 10^\circ + 2\sin(\omega t)$, $\alpha = 10^\circ$ upstroke; $k = 0.05$, and $\mathrm{Re}_c = 0.54 \times 10^6$ [from Ref. (154)].

and Reynolds numbers have been conducted in the past two decades. These measurements provide a database, many times only in the form of integrated unsteady loads, against which numerical methods can be calibrated and validated. Many investigators applied numerical techniques, described in Section 4, for the prediction of dynamic stall flows. The majority of the numerical work was directed towards the investigation and prediction of *two-dimensional* dynamic stall flowfields. Only recently, unsteady, three-dimensional flowfields, which are of primary interest in industrial applications, have been calculated for a pitching[116] and an oscillating[41] wing. In Section 6.1 incompressible flow dynamic-stall solutions are presented. Compressible dynamic-stall flow solutions are presented in Section 6.2 where numerical predictions of compressibility effects on dynamic stall are shown. Special emphasis is given to the presentation of results obtained by several investigators for high Reynolds number, turbulent dynamic stall flowfields. The effects of turbulence modeling on the accuracy of the computed solutions are shown in Section 6.2.2. Leading-edge transition plays an important role in the development of dynamic stall even when the Reynolds number is fairly large. The effect of incorporating transitional flow behavior in dynamic-stall calculations is shown in Section 6.2.3. Finally, recent numerical investigations on suppressing dynamic stall by modifying the leading-edge geometry are summarized in Section 6.2.4.

6.1. INCOMPRESSIBLE FLOW

Dynamic stall of airfoils and wings in laminar flow is mainly of theoretical interest because fully laminar flow cannot be sustained above Reynolds numbers $\mathrm{Re}_c \approx 10^4$ based on chord length. Some of the early numerical investigations on dynamic stall, however, were done for laminar flows. Due to the lack of measurements for most low Reynolds number flow conditions, no quantitative comparisons are available. The important contribution of these early investigations is that they have shown the ability of the numerical solutions to obtain certain flowfield features similar to the available flow visualizations. The computed hysteresis loops appear to capture the measured trends which were obtained, however, for higher Reynolds number and freestream speeds. Laminar incompressible dynamic stall

computations are presented in Section 6.1.1. Incompressible turbulent flow computed results, which are of practical interest to wind turbine technology and design, are presented in Section 6.1.2.

6.1.1. Laminar flow calculations

Laminar incompressible flow solutions over a modified NACA-0012 airfoil were obtained by Mehta[107] using the vorticity stream function formulation. The computations were conducted for $\mathrm{Re} = 5 \times 10^3$ and 10×10^3 and oscillatory motion given by $\alpha(t) = 10^\circ[1 - \cos(\omega t)]$ and reduced frequencies $k = 0.25$ and 0.50. Good qualitative agreement of the computations with water tunnel flow visualization was obtained and the development of the unsteady flowfield and the loads was investigated. Sample results of Mehta's computations are shown in Fig. 29.

Incompressible laminar dynamic stall flowfields were also investigated by Ghia *et al.*[64] using the vorticity–streamfunction formulation. In Ref. (65), solutions were obtained for pitch up motion of a NACA-0015 airfoil at $\mathrm{Re} = 10 \times 10^3$ and 45×10^3. Favorable comparison of the computation with the smoke flow visualization was obtained. Sample results from these comparisons are shown in Fig. 30 for the flow at $\mathrm{Re} = 45 \times 10^3$ and $\alpha \approx 36^\circ$. In the same investigation the effect of leading-edge suction and trailing-edge injection in controlling the evolution of the dynamics-stall vortex was also investigated. It was found that suppression of the leading-edge flow separation controls the formation of the dynamic-stall vortex with a suction/injection strength of only 5% of the free-stream speed.

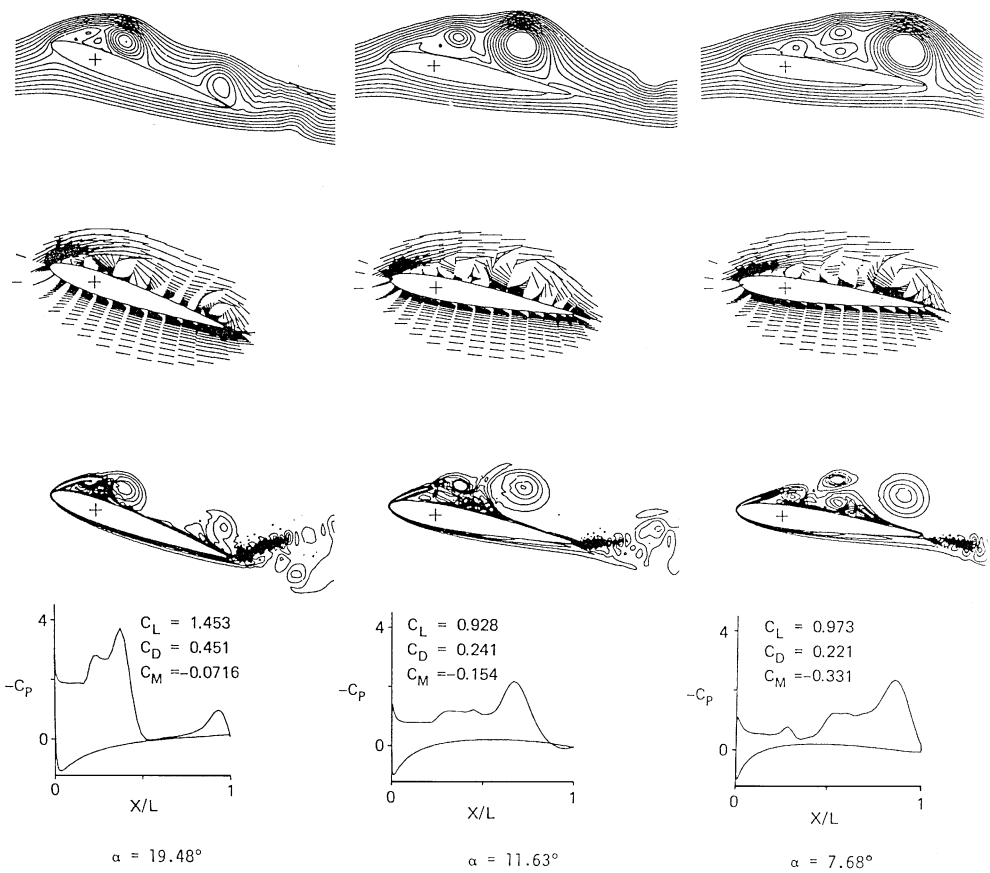

Fig. 29. Computed instantaneous streamlines, velocity vectors, vorticity contours, and surface pressure distribution; Incompressible flow calculation, $\mathrm{Re}_c = 5 \times 10^3$, $k = 0.5$, $\alpha = 10^\circ + 10^\circ \cos(\omega t)$ [from Ref. (107)].

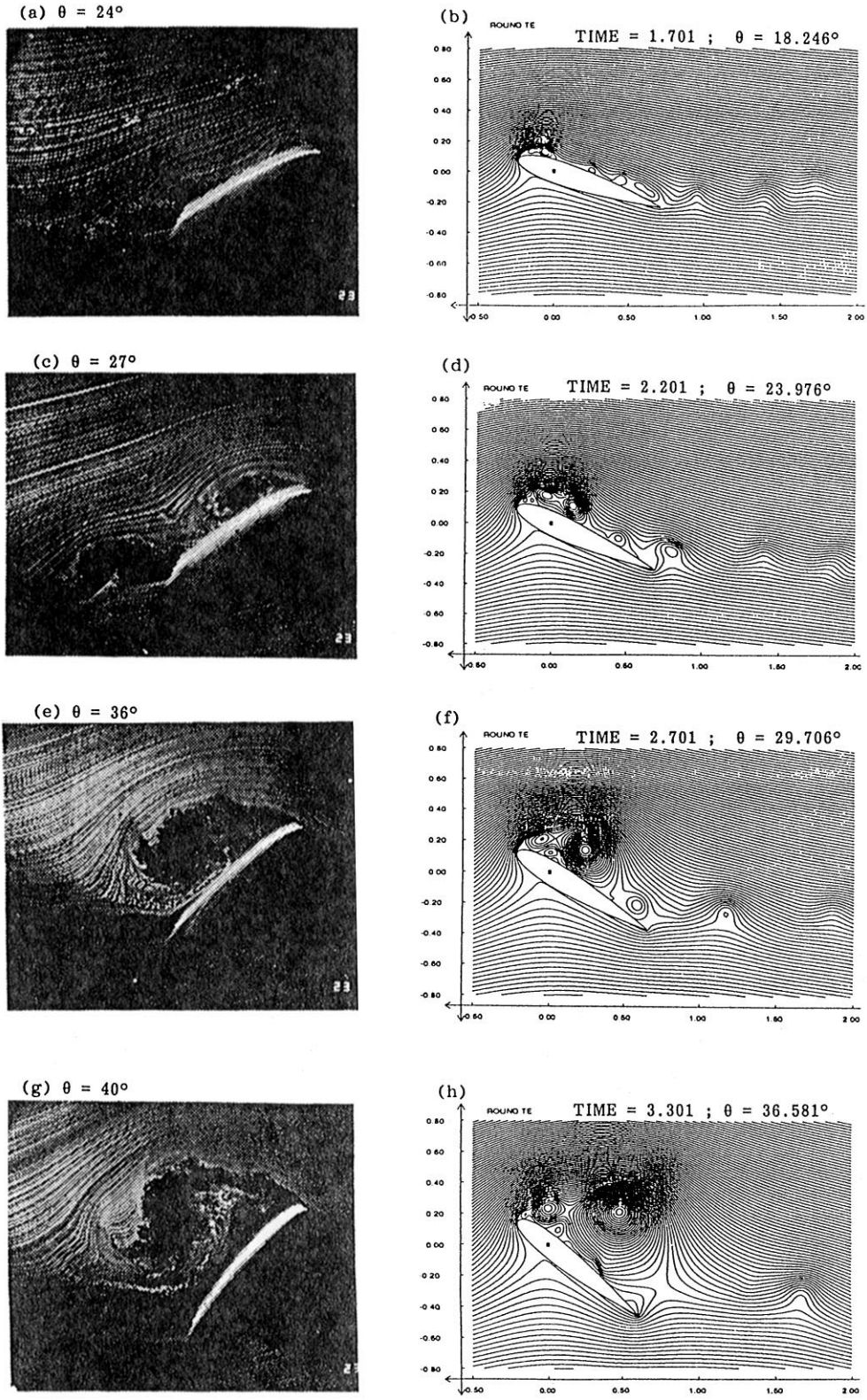

Fig. 30. Computed vorticity contours for a NACA 0015 airfoil at ramp motion; $Re_c = 045 \times 10^3$ [from Ref. (64)].

6.1.2. Turbulent flow calculations

Laminar[166] and turbulent[149] incompressible dynamic-stall flowfields were investigated numerically by Wu and his collaborators, using the vorticity–velocity formulation described in Section 4.4.2. Fully turbulent solutions at $\mathrm{Re} = 1 \times 10^6$ for a sinusoidal oscillation of a NACA-0012 airfoil with $\alpha(t) = 15^\circ + 10^\circ \sin(\omega t)$ and reduced frequencies $k = 0.1, 0.15$ and 0.25 were obtained in Ref. (149), using the computationally efficient procedure of Refs. (164, 165). The Baldwin–Lomax turbulence model was used for the prediction of the turbulent flow behavior. The computed loads were in good agreement with the measurements. A comparison of the computed lift, drag and pitching moment hysteresis loops for $k = 0.15$ with the experiment is shown in Fig. 31. Similar quantitative agreement was achieved for lower and higher reduced oscillation frequencies.

6.2. COMPRESSIBLE FLOW

Helicopter rotors and propeller blades as well as most turbomachinery bladings operate at Reynolds numbers above 10^5 to several millions, therefore the flow is mostly turbulent. However, there will always be a small laminar/transitional flow region near the leading edge unless the flow is tripped close to the leading edge stagnation point. Wind tunnel experiments typically are conducted at Reynolds numbers between $0.5 \times 10^6 \leqslant \mathrm{Re}_c \leqslant 4 \times 10^6$. Therefore, purely laminar flow calculations are of limited practical interest. Nevertheless, early numerical solutions of dynamic stall were performed for purely laminar flows because the lack of computing resources did not allow the use of large grids required for turbulent flow solutions. More recently, laminar solutions were obtained in order to investigate the leading-edge separation process. The laminar, compressible flow investigations on dynamic stall are summarized in Section 6.2.1. Turbulent flow calculations of dynamic stall are presented in Section 6.2.2, where improvements obtained from the application of recently developed one– and two–equation turbulence models are shown. The effect of transition on the accuracy of computed solutions is shown in Section 6.2.3.

6.2.1. Laminar flow computations

The ability of numerical schemes to predict compressible unsteady flowfields over oscillating airfoils was tested in early investigations[134, 84]. In Ref. (84) inviscid solutions for an oscillating airfoil in transonic flow at $M_\infty = 0.8$ were obtained with a central difference space discretization and a Runge–Kutta time-integration scheme. Inviscid and viscous turbulent solutions with the Baldwin–Lomax turbulence model and an approximately factorized, central difference algorithm were obtained by Chyu and Davis[31] for small amplitude oscillations of a NACA-64A010 airfoil in transonic flow at $M_\infty = 0.75$ and 0.8. The computations of Ref. (31) were in good agreement with the measured unsteady pressures for attached flows. Small discrepancies were obtained for the separated part of the flow. An example of these computations is shown in Fig. 32, where computed solutions for reduced frequencies $k = 0.025$ and 0.2 are compared with experimental measurements. The high Reynolds number of the experiment and the small oscillation amplitude justified the use of an inviscid solution. Small deviations of this solution from the experiment are observed at the shock location. Small amplitude oscillations are of interest in aeroelastic response and flutter predictions. Numerical investigations of unsteady flow relevant to aeroelastic calculations can be found in Ref. (71).

One of the first numerical investigations of dynamic stall for compressible flow was presented by Sankar and Tassa,[134] who used central differences for space discretization and performed time-accurate computations with the implicit Beam–Warming algorithm. Low Reynolds number, $5000 \leqslant \mathrm{Re}_c \leqslant 10000$, laminar flows were considered and the effects of compressibility on the dynamic stall were investigated in solutions computed at free-stream Mach numbers $M_\infty = 0.2$ and 0.4. An example of the results presented in Ref. (134) is

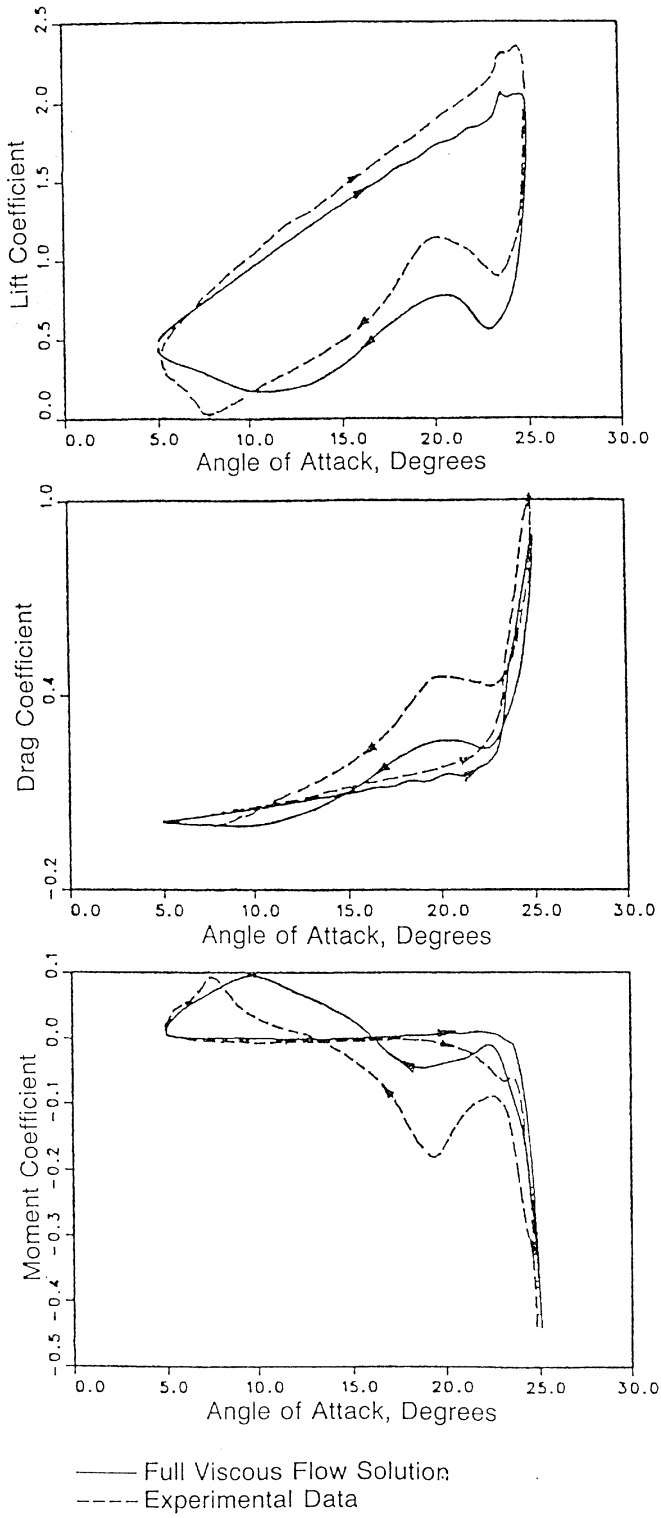

Fig. 31. Comparison of the computed load hysteresis loops with the measurements; $\alpha(t) = 10 + 10\sin(\omega t)$, $k = 0.2$, $\mathrm{Re}_c = 3 \times 10^6$ [from Ref. (149)].

shown in Fig. 33, where the computed lift and pitching moment hysteresis loops for a reduced frequency $k = 0.5$ and $M_\infty = 0.4$ are presented. The computed load hystereses loops show similar trends with the high Reynolds number turbulent flow measurements reported by McCroskey.[103]

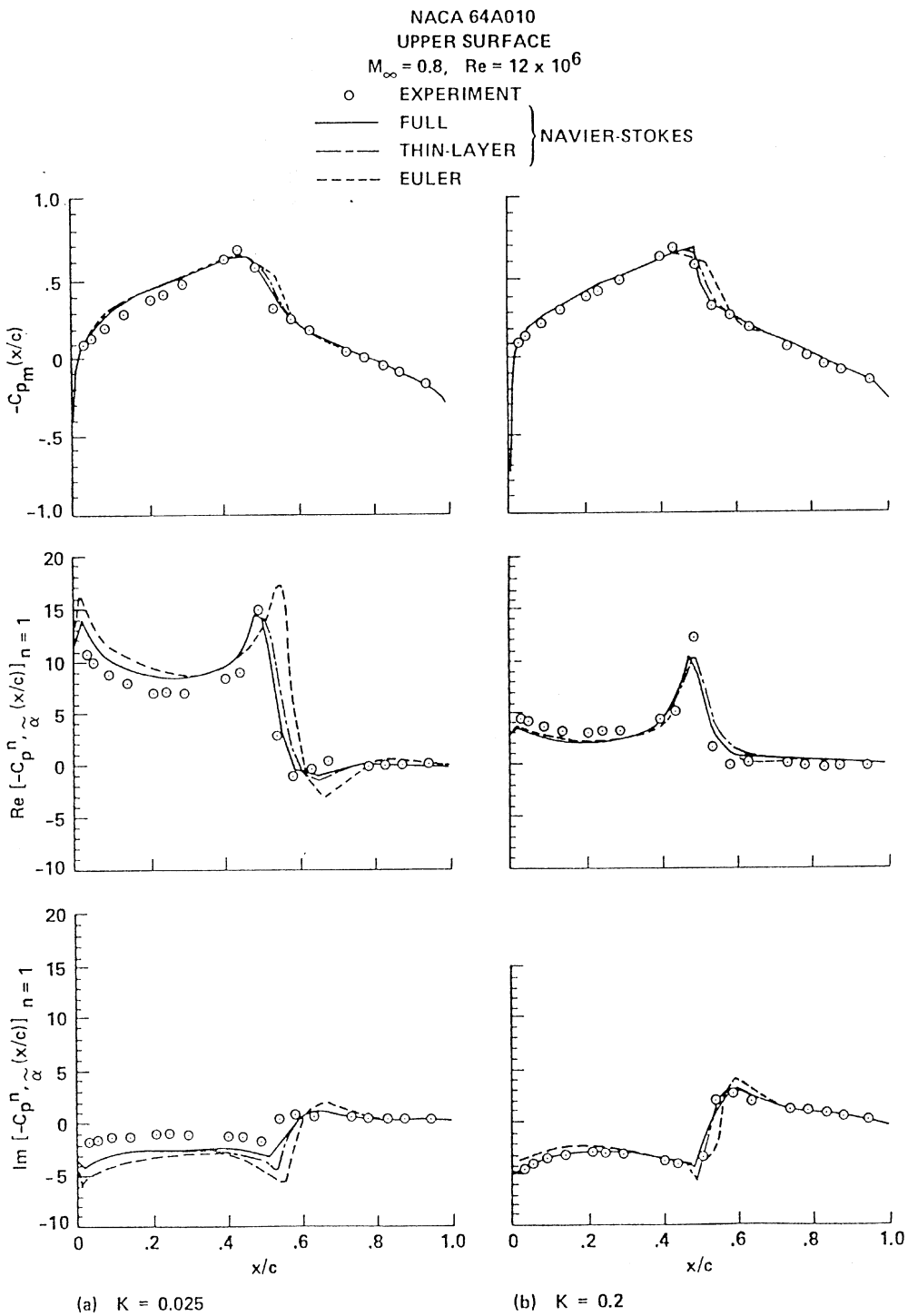

Fig. 32. Mean and first harmonic complex components of pressure coefficients; $a = 0 + 1° \cos(\omega t)$ [from Ref. (31)].

Dynamic stall in laminar flow was further investigated by Visbal.[157,158] An example of these computations is shown in Figs 34–36. In Fig. 34 the effect of pitching axis location on the development of the dynamic stall flowfield is demonstrated. The Reynolds number is $Re_c = 45{,}000$ and the solution was obtained for $M_\infty = 0.2$. The computed solutions of Fig. 34 are in good agreement with flow visualization experiments. Visbal used an implicit

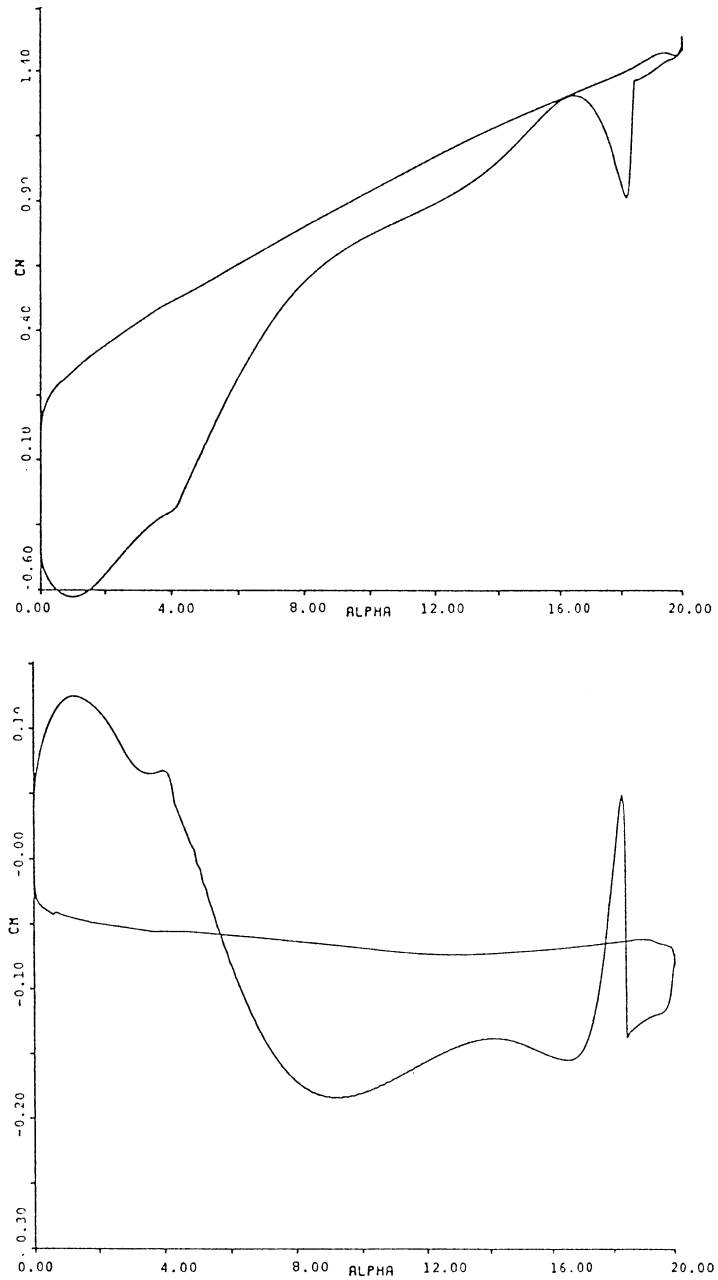

Fig. 33. Computed lift and pitching moment hysteresis loops for the dynamic stall of a NACA 0012 airfoil; $M = 0.2$, $\mathrm{Re}_c = 5,000$, $K = 0.5$ [from Ref. (134)].

central difference method for the computations. Further investigations of pitch rate and Mach number effects were also conducted. Examples of these computations are shown in Fig. 35, where the lift and pitching moment response of a NACA-0012 airfoil executing ramp motion with different reduced frequencies in low-speed flow $M_\infty = 0.2$ was computed. The development of a leading-edge supersonic region at the airfoil leading edge for $M_\infty = 0.4$ was also found, as shown in Fig. 36.

More recently, numerical investigations of dynamic stall in laminar flow were performed with the numerical solution of the compressible Navier–Stokes equation in Refs (29, 124). The objective of these investigations was to identify flow features concerning the onset of leading-edge separation. Solutions were obtained with an implicit central difference scheme

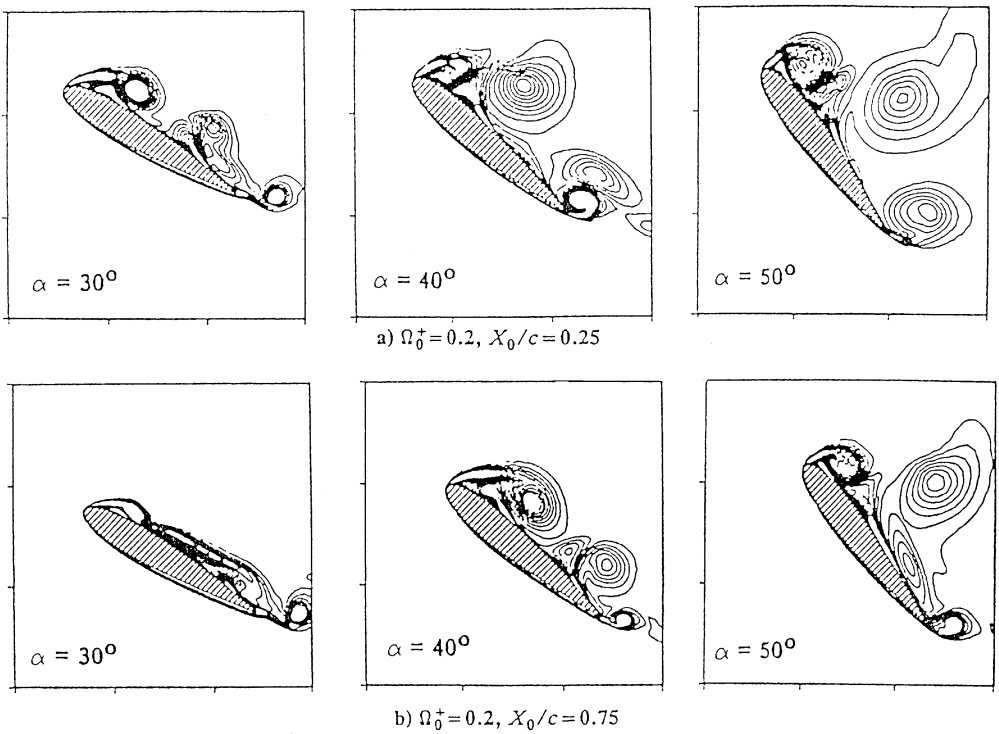

Fig. 34. Effect of pitching axis location on the evolution of the vorticity field [from Ref. (158)].

and high grid resolution for a pitching airfoil. The effects of compressibility were investigated and complex recirculatory flow patterns at the airfoil leading edge were obtained, as shown in Fig. 37. In this figure, the instantaneous streamlines for $\mathrm{Re_c} = 10^4$, of a NACA-0012 airfoil at $\alpha = 18^\circ$ rapidly pitching with reduced frequency $k = 0.1$, Mach numbers $M_\infty = 0.2$ and 0.5 are shown. The conclusion of this investigation was that increase in Mach number from 0.2 to 0.5 delays the formation of the recirculatory region. It was also reported that for low pitch rates, trailing-edge dynamic stall was obtained, while for higher pitch up rates the leading-edge dynamic stall was obtained. Similar conclusions concerning the dynamic-stall initiation were obtained in Ref. (124), where the solution was obtained with a high-order finite-difference scheme and a zonal grid with very high grid resolution at the leading edge was used.

6.2.2. Turbulent flow computations

Dynamic stall of airfoils, helicopter and turbomachinery blades and aircraft wings for turbulent high-speed flow is of primary interest in practical applications. In this section, recent attempts to calculate dynamic stall with the numerical solution of the compressible Navier–Stokes equations augmented with a turbulence models for the computation of the fully turbulent flow region are presented.

Compressible, unsteady, turbulent flow computations were obtained by Sankar and Tang[134] and Rumsey and Anderson.[132] The latter investigators computed dynamic stall at transonic speeds and the numerical simulations were in agreement with the experiments of Ref. (95) Dynamic stall of a SSC-A09 Sikorsky airfoil executing rapidly pitching and oscillatory motions was investigated numerically by Ekaterinaris[40] for turbulent $\mathrm{Re_c} = 2 \times 10^6$ flow. An implicit finite-difference scheme was used for the numerical solution of the compressible thin-layer form of the Navier–Stokes equations. Turbulent flow was computed with the Baldwin–Lomax algebraic model. A comparison of the computed and

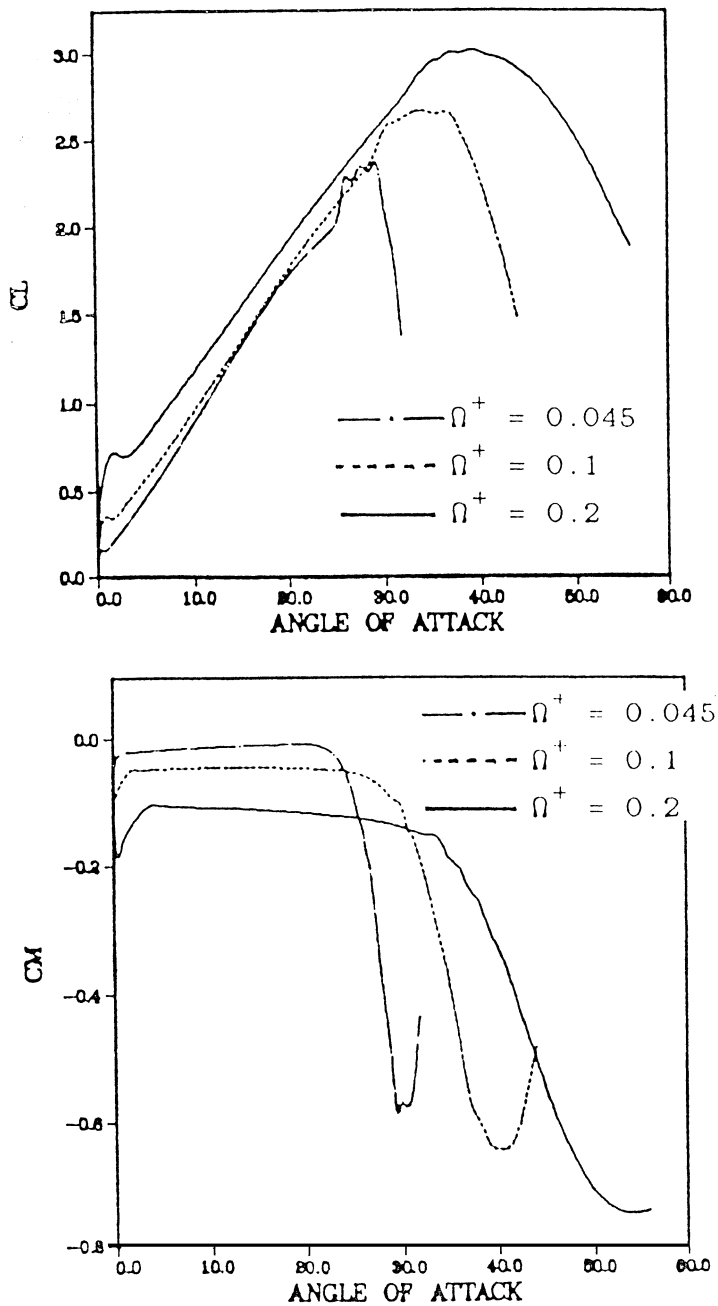

Fig. 35. Effect of reduced frequency on the computed unsteady lift and pitching moment coefficients [from Ref. (157)].

measured lift and pitching moment hysteresis loops for oscillatory motion $\alpha(t) = 10^\circ + 10^\circ \sin(\omega t)$ is shown in Fig. 38. Both the computation and the experiment were performed for a free-stream Mach number of $M_\infty = 0.2$. The lift and pitching moment hysteresis loops were predicted reasonably well from the numerical solution. In the same study the effects of compressibility and pitch rate were also investigated and solutions for a rapid pitch–up motion with different reduced frequencies and pitch up rates were obtained. A comparison of the computed and measured lift for the airfoil pitching at different rates is shown in Fig. 39. It was found that dynamic stall develops at lower angles of incidence as the Mach number increases. Figure 40 shows the effect of increasing Mach number on the development of dynamic stall. Supersonic leading-edge regions were found

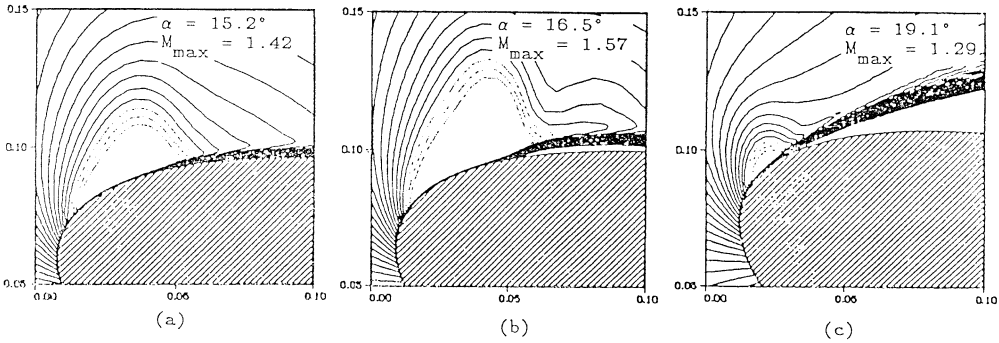

Fig. 36. Evolution of leading-edge supersonic bubble; $M = 0.4$, $\mathrm{Re_c} = 10^6$, $k = 0.045$ [from Ref. (157)].

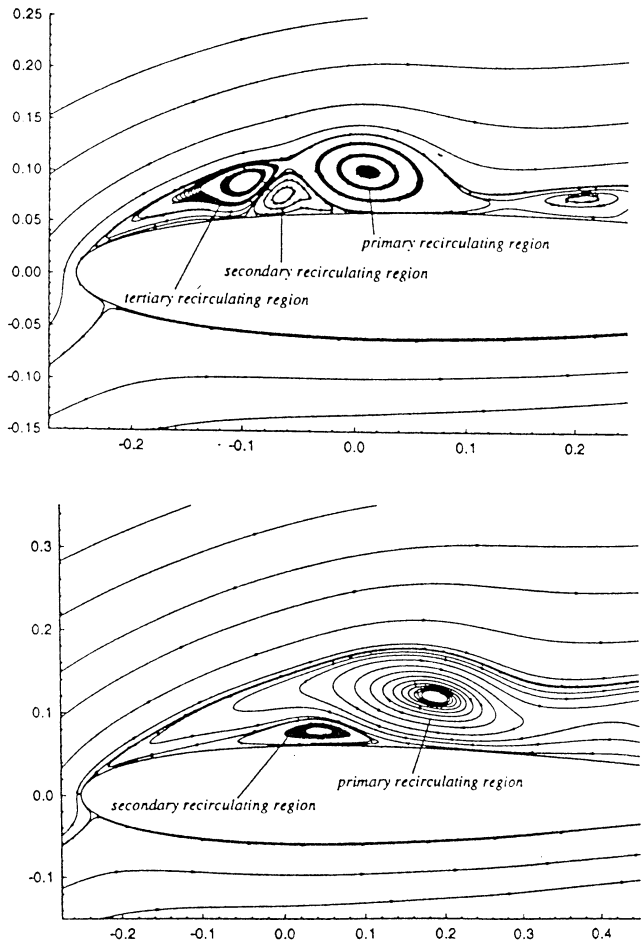

Fig. 37. Effect of Mach number on leading edge flowfield for ramp motion, shown by instantaneous streamlines at $\alpha = 18^\circ$; upper $M = 0.2$, $\mathrm{Re_c} = 10^4$, $k = 0.1$, lower $M = 0.5$, $\mathrm{Re_c} = 10^4$, $k = 0.1$. [from Ref. (29)].

consistent with Visbal's[158] laminar flow solutions. The same cases were also investigated numerically by Patterson and Lorber,[119] who reported similar results.

Numerical investigations of dynamic stall in turbulent flow were also conducted by Fung and Carr,[58] who concluded that an increase of the reduced frequency delays the boundary-layer separation and allows the airfoil to attain higher lift values at higher angles of attack. However, at high incidences the flow becomes locally supersonic and the local supersonic

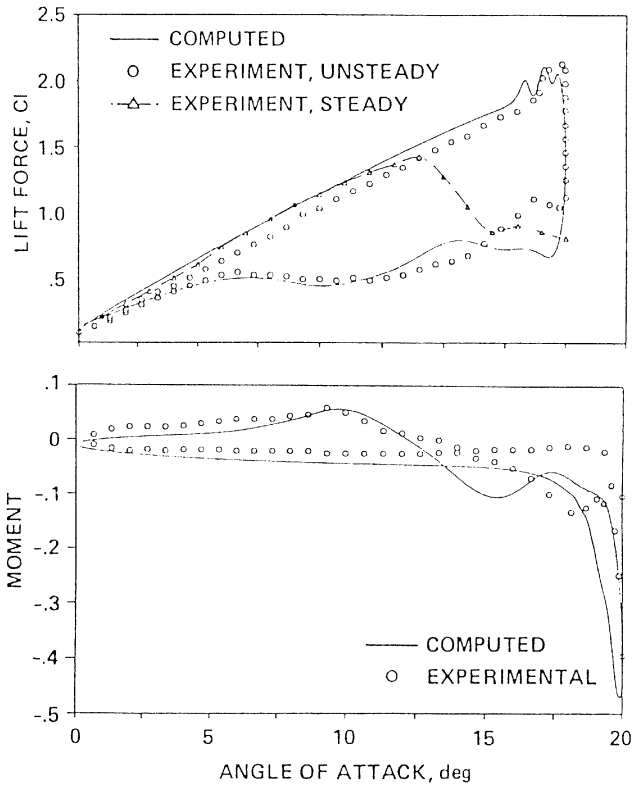

Fig. 38. Comparison of the computed unsteady lift and pitching moment hysteresis loops with the measurements; $\alpha(t) = 10^\circ + 10^\circ \sin(\omega t)$, $k = 0.1$, $\mathrm{Re}_c = 2 \times 10^6$ [from Ref. (40)].

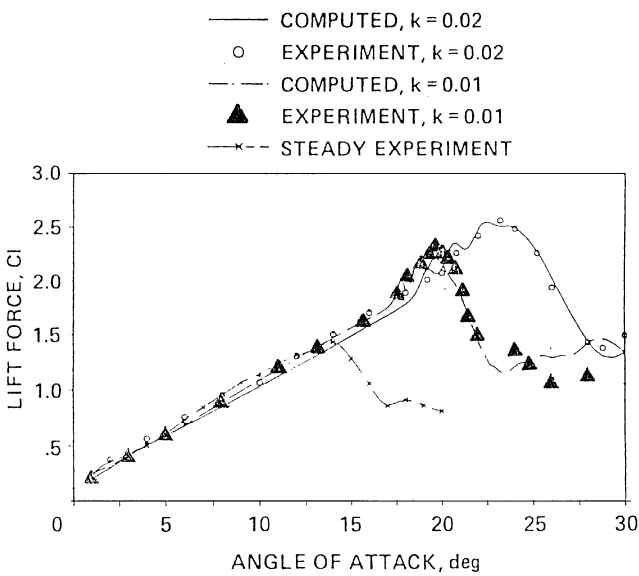

Fig. 39. Effect of reduced frequency on the unsteady lift; $\mathrm{Re}_c = 2 \times 10^6$, $M = 0.2$ [from Ref. (40)].

region may be terminated by a shock close to the leading edge where the radius of curvature is small. Fung and Carr therefore suggested that the shock-generated vorticity may be responsible for dynamic airfoil stall and that compressibility effects may become important for free-stream Mach numbers as low as 0.2. In a later investigation, Currier and Fung[34]

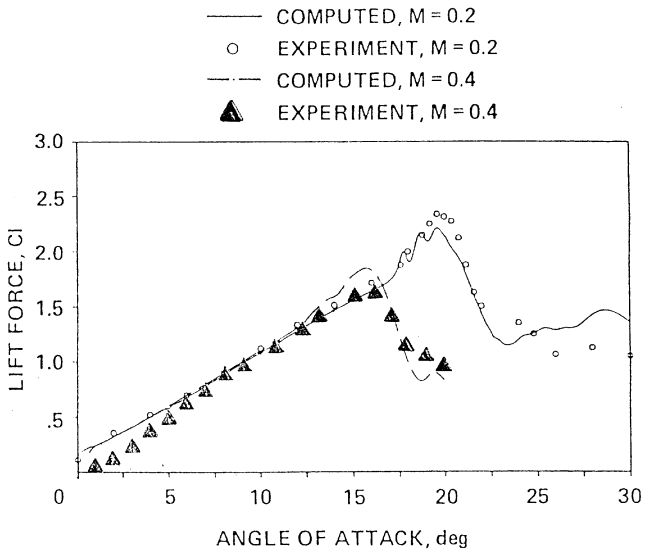

Fig. 40. Effect of Mach number on the unsteady lift [from Ref. (40)].

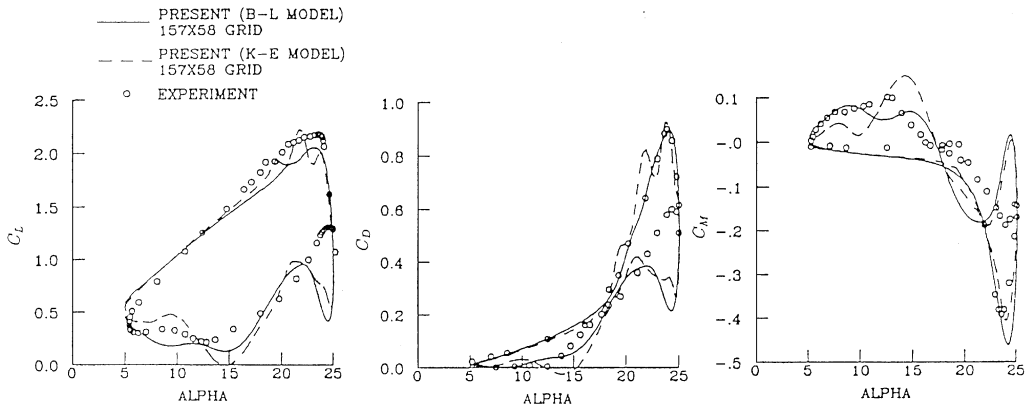

Fig. 41. Effect of turbulence modeling on the computed load hysteresis loops; NACA-0012 airfoil, $M = 0.283$, $\alpha(t) = 15^\circ + 10^\circ \sin(\omega t)$, $k = 0.151$, $\mathrm{Re_c} = 3.45 \times 10^6$ [from Ref. (166)].

concluded in addition that the dependency on reduced frequency can be vastly different for airfoils with different leading-edge shape.

A conclusion of the early numerical investigations of dynamic stall in turbulent high Reynolds number flow was that algebraic turbulence models cannot properly simulate the massively separated flow at high angles of incidence. Therefore, the ability of more sophisticated turbulence models, such as the k–ε model, has been tested. Wu and Sankar[166] used the k–ε model to compute deep stall of a NACA-0012 airfoil. The computed load hysteresis loops obtained with the k–ε model, however, did not show significant improvement compared to the load hysteresis loops obtained from the algebraic Baldwin–Lomax model. Figure 41 shows the comparison of the computation with the experiment reported in Ref. (166). Similar studies for a rapidly pitching airfoil were presented by Rizetta and Visbal.[128]

A problem encountered in several numerical investigations was lack of accuracy in the computation of light dynamic stall hysteresis loops. Light stall usually occurs when the airfoil oscillates around a mean angle of attack close to the static stall and with a small oscillatory amplitude. Depending on the parameters of motion, e.g. mean angle, oscillation amplitude, and reduced frequency, the pitching moment hysteresis loop for light stall may

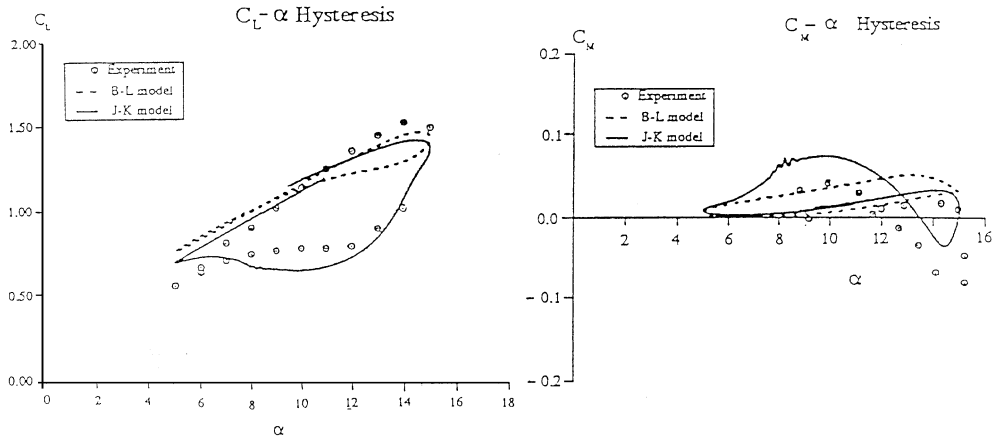

Fig. 42. Effect of turbulence modeling on the computed load hysteresis loops; $M = 0.3, \alpha(t) = 10^\circ + 5.0^\circ \sin(\omega t), k = 0.1$, NACA 0012 airfoil $\mathrm{Re}_c = 4 \times 10^6$ [from Ref. (38)].

exhibit characteristics indicating positive or negative damping, which is characteristic for stall flutter, as pointed out by Carta and Lorber.[12] Accurate computation of pitching moment hysteresis loops is, therefore, critical to efforts in designing helicopter and turbomachinery blades which can operate without stall-flutter-induced loading. The Johnson–King half-equation model presented in Appendix C provided a very good prediction of mildly separated flows. Calculations of shock-induced separated flows have shown that this model is a superior option compared to the algebraic models.

Computations of light dynamic stall of a NACA-0012 airfoil with the Johnson–King model were obtained by Dindar and Kaynak[38] and Clarkson *et al.*[32] The Reynolds number of the experiment was $\mathrm{Re}_c = 3 \times 10^6$, the reduced frequency $k = 0.1$ and the oscillatory motion $\alpha(t) = 10^\circ + 5^\circ \sin(\omega t)$. In both solutions similar grid densities were used and the oscillation amplitude was increased to 5.5° in order to promote separation because for the amplitude of the experiment ($\alpha = 5^\circ$), very little separation at the trailing edge region was obtained and hysteresis effects were small. The computed lift and pitching moment hysteresis loops in Refs (38, 32) are shown in Figs 42 and 43, respectively. The computations of Ref. (38) (Fig. 42) were obtained with the ARC2D code. In Ref. (32) an implicit central difference method was also used. The lift hysteresis computed in Ref. (38), Fig. 42, overpredicted separation and the pitching moment was in fairly good agreement with the experiment. In Ref. (32) (Fig. 43), on the other hand, the lift was in fairly good agreement with the experiment while the pitching moment hysteresis loops did not yield the trends shown in the experiment. In the same figure, the hysteresis loops obtained from the algebraic RNG-based model are also shown.

In an attempt to improve the prediction of dynamic stall, Srinivasan *et al.*[143] performed a systematic study of the effect of turbulence modeling on dynamic-stall computations. They used algebraic, half-equation and one-equation turbulence models. An implicit central difference scheme, as in Ref. (32), was used for the numerical solution. The effects of grid density and artificial smoothing coefficients on the accuracy of the computed unsteady solutions was investigated. Deep and light dynamic stall of a NACA-0015 airfoil, which was studied experimentally in Ref. (120) was computed. The experiments for these cases were obtained at $M_\infty = 0.3$ and Reynolds number $\mathrm{Re}_c = 2 \times 10^6$. However, the flow was tripped at the leading edge to ensure a fully turbulent flow. Load hysteresis loops from Ref. (143), for light and deep stall, are shown in Figs 44 and 45, respectively. The numerical results of Ref. (143) indicate that the one–equation turbulence models show improvements compared to the Baldwin–Lomax algebraic eddy viscosity, the Johnson–King and the RNG-based algebraic model. Application of the algebraic turbulence models and the Johnson–King model requires the definition of the boundary-layer thickness, which becomes ambiguous for massively separated flows. As a result, one-equation turbulence models are more

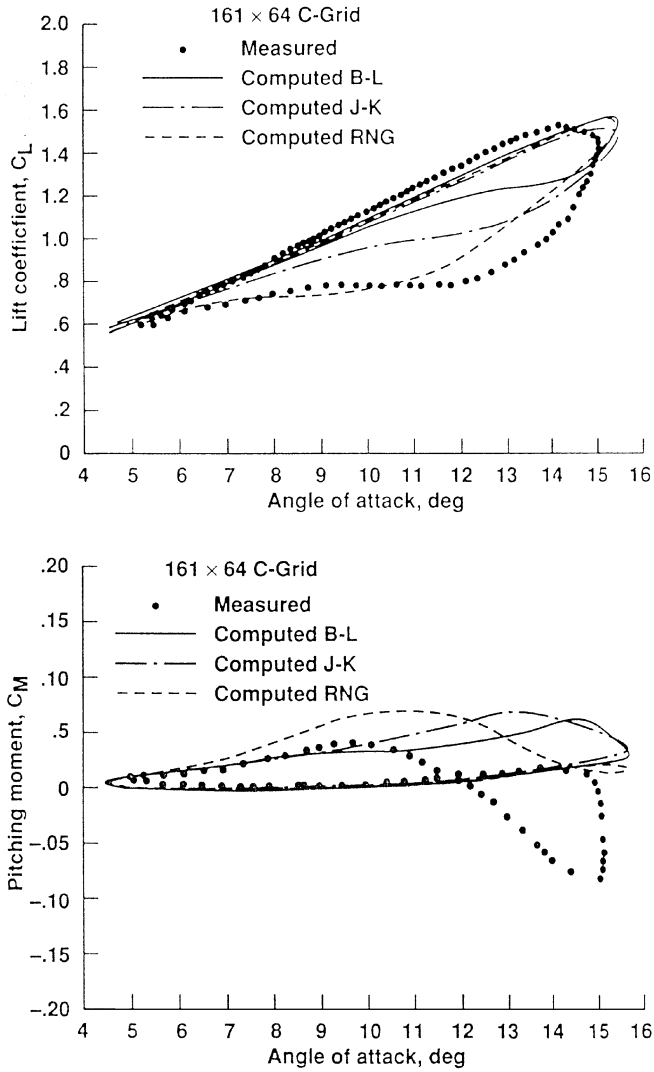

Fig. 43. Effect of turbulence modeling on the computed load hysteresis loops $M = 0.3, \alpha(t) = 10^\circ + 5.0^\circ \sin(\omega t), k = 0.1$, NACA 0012 airfoil $Re_c = 4 \times 10^6$ [from Ref. (32)].

appropriate for the computation of deep stall. Examples of the computed load hysteresis loops are shown in Figs 44 and 45 to support this conclusion. The reversed flow location on the suction surface, obtained from different turbulence models, was recorded during the oscillation cycle. Figure 46 shows that significant changes are obtained for the flow-reversal point location with different turbulence models.

The computation of the experimental case of Ref. (120) was repeated by Ekaterinaris and Menter.[44] An implicit, upwind-biased numerical scheme was used in these computations. One- and two-equation turbulence models were tested for unsteady attached flow for the light and deep-stall cases. Examples of these computations are shown in Fig. 47, where the performance of the S–A, B–B and the SST k–ω turbulence models in predicting light dynamic stall is demonstrated. Computations of deep stall with one- and two–equation models are shown in Figs 48 and 49, respectively. During the downstroke the computed loads show an oscillatory behavior. The flowfield structure is shown in Fig. 50 by means of unsteady particle trace trajectories. These trajectories are obtained by particles which are released continuously in the flowfield close to the leading edge region and they are subsequently convected with the computed local instantaneous flow speed. It is observed that a significant portion of the upper surface has reverse flow during the downstroke. It

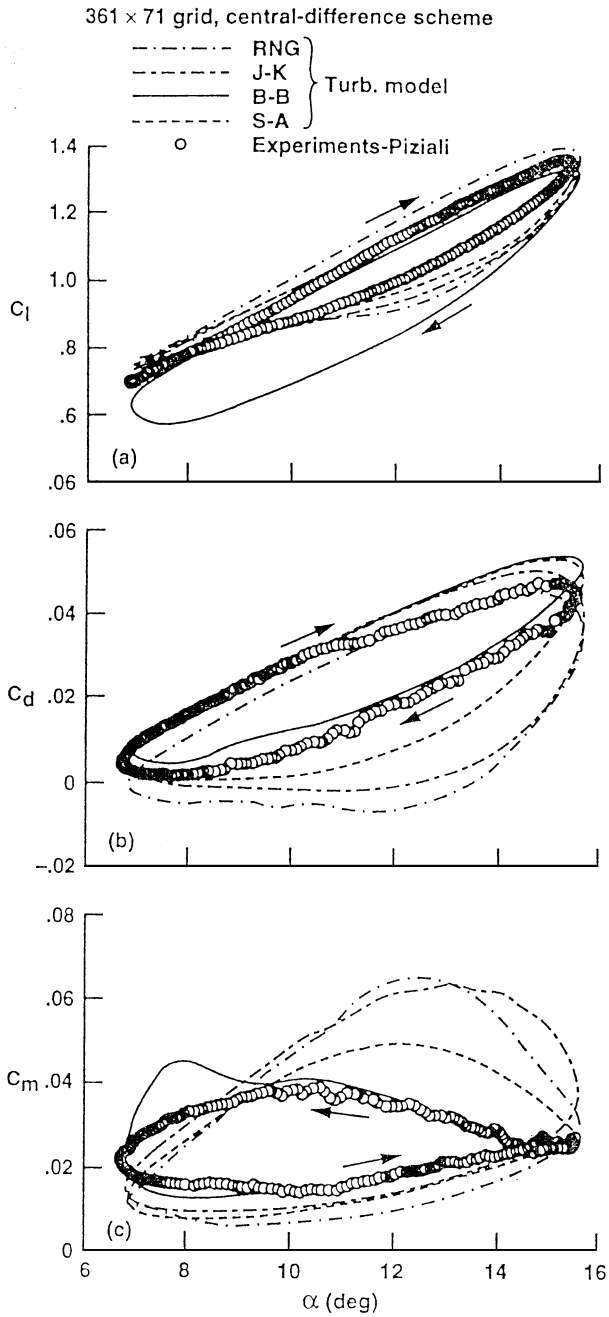

Fig. 44. Effect of turbulence modeling on the computed load hysteresis loops for light stall $M = 0.3, \alpha(t) = 11^\circ + 4.2^\circ \sin(\omega t), k = 0.1$, NACA 0015 airfoil $Re_c = 2 \times 10^6$ [from Ref. (143)].

was also found that the oscillatory behavior of the loads is caused by vortical structures at the trailing edge. The experimental data were averaged over several cycles and, as expected, the variations were smoothed out. The conclusion of Ref. (44) was that the one-equation models and the SST k–ω model offer an advantage compared to the standard k–ω and the zonal k–ε turbulence models.

The k–ε and S–A models were further tested in Ref. (94) for the same experimental condition of Ref. (120). The upwind TURNS code[142] was used for the numerical solution. A comparison of the hysteresis loops obtained from computations with the S–A and the standard k–ε models with the measurements is shown in Fig. 51. Similar trends with the

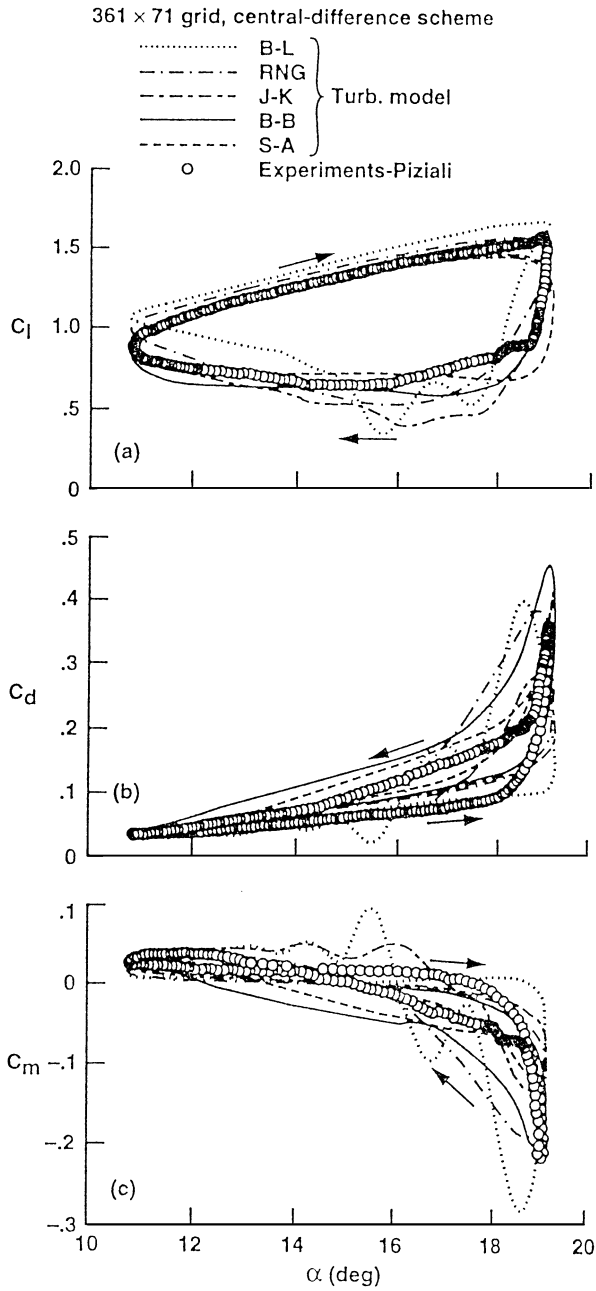

Fig. 45. Effect of turbulence modeling on the computed load hysteresis loops for deep stall $M = 0.3$, $\alpha(t) = 15^\circ + 4.2^\circ \sin(\omega t)$, $k = 0.1$, NACA 0015 airfoil $Re_c = 2 \times 10^6$ [from Ref. (143)].

computations of Ref. (44) are observed and oscillatory behavior was obtained for the downstroke with both the S–A and k–ε turbulence models. The development of the dynamic stall reported in Ref. (94), is shown with unsteady particle traces in Fig. 52.

Alternative numerical techniques were explored for the computation of dynamic stall flows. The vorticity confinement method was developed by Wang[159] for the computation of dynamic-stall flows with a reduced computing cost. Hixon and Sankar[81] applied a GMRES method for the computation of dynamic stall. A comparison of the load hysteresis loop obtained from the GMRES solution with the experiment is shown in Fig. 53. In Ref. (126) a structured/unstructured method was applied for the computation of dynamic stall on a rapidly pitching airfoil. The numerical mesh used for the calculations is shown in

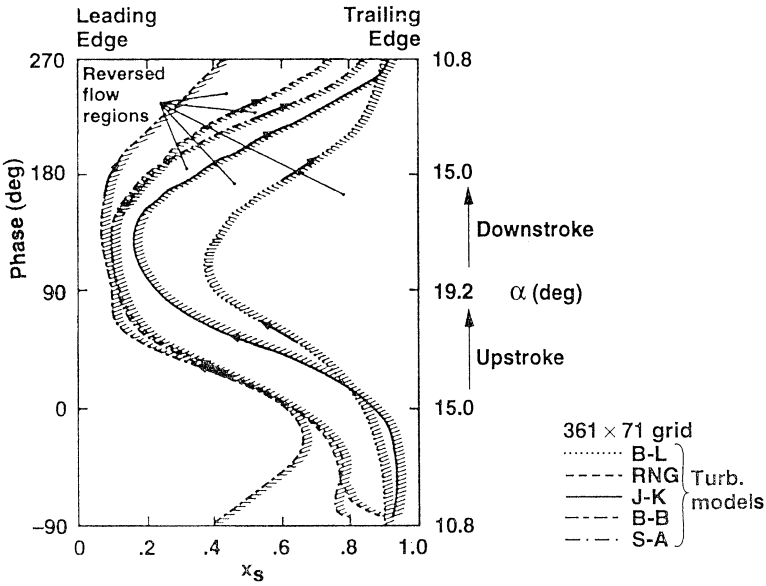

Fig. 46. Reversed flow point obtained from computations with different turbulence models; $M = 0.3, \alpha(t) = 15^\circ + 4.2^\circ \sin(\omega t), k = 0.1$, NACA 0015 airfoil $Re_c = 2 \times 10^6$ [from Ref. (143)].

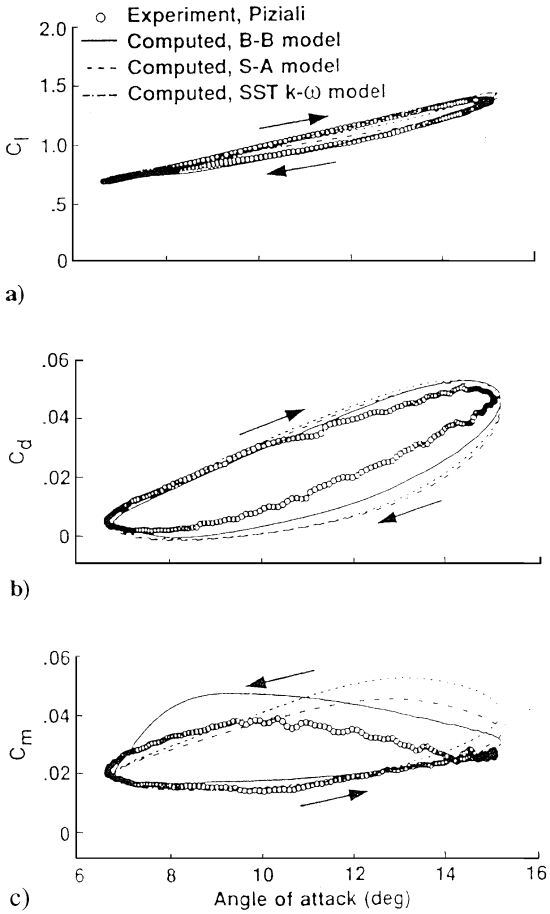

Fig. 47. Effect of turbulence modeling on the computed load hysteresis loops for light stall; $M = 0.3, \alpha(t) = 11 + 4.2^\circ \sin(\omega t), k = 0.1$, NACA 0015 airfoil $Re_c = 2 \times 10^6$ [from Ref. (44)].

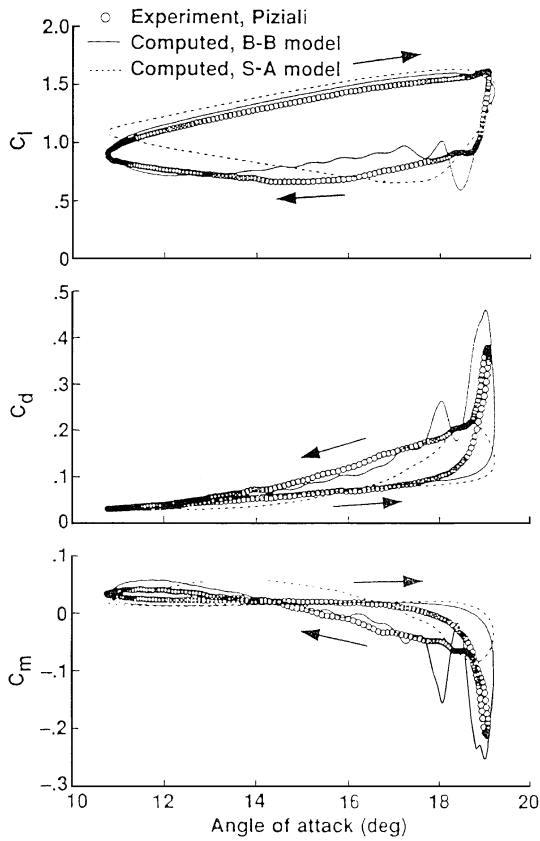

Fig. 48. Load hysteresis loops for deep-stall computed with one-equation turbulence models; $M = 0.3$, $\alpha(t) = 15 + 4.2^\circ \sin(\omega t)$, $k = 0.1$, NACA 0015 airfoil $\mathrm{Re_c} = 2 \times 10^6$ [from Ref. (44)].

Fig. 54. The flowfield near the airfoil surface is computed more efficiently with a structured grid where turbulence models can be applied more easily. The structured/unstructured method has potential for dynamic-stall computations because it allows adaptive re-meshing of the suction side to better resolve the dynamic-stall vortex. A full unstructured grid method was recently presented by Venkatakrishnan and Mavriplis.[156] Dynamic-stall flowfields at transonic speed were computed. This method, however, has potential for accurate computation of weak shocks formed at the airfoil leading edge by adaptive remeshing of the leading edge region.

6.2.3. Effect of transition

The effect of the leading-edge transition was not taken into account in most of the earlier dynamic-stall computations. To overcome this difficulty, part of the leading-edge flow was computed as laminar while the rest as fully turbulent.[58] Experimental investigation[24] of low Reynolds number airfoil flows at fixed angles of incidence indicated that at the leading edge the flow is transitional and a separation bubble develops as the angle of attack increases. Numerical investigations were performed by Ekaterinaris *et al.*[42] at the experimental flow conditions, $\mathrm{Re_c} = 0.54 \times 10^6$, $M_\infty = 0.3$. It was concluded that a fully turbulent computation cannot predict the flow physics at the leading edge but a transitional flow computation closely predicted the separation bubble and the drop of the suction peak observed in the experiment. A comparison of the measured surface pressure coefficient distribution with the fully turbulent solution and the solution where the transitional flow behavior was modeled is shown in Fig. 55. In the computation the location of the transition onset was obtained by Michel's criterion, given in Section 4.2.2, and the computation of the

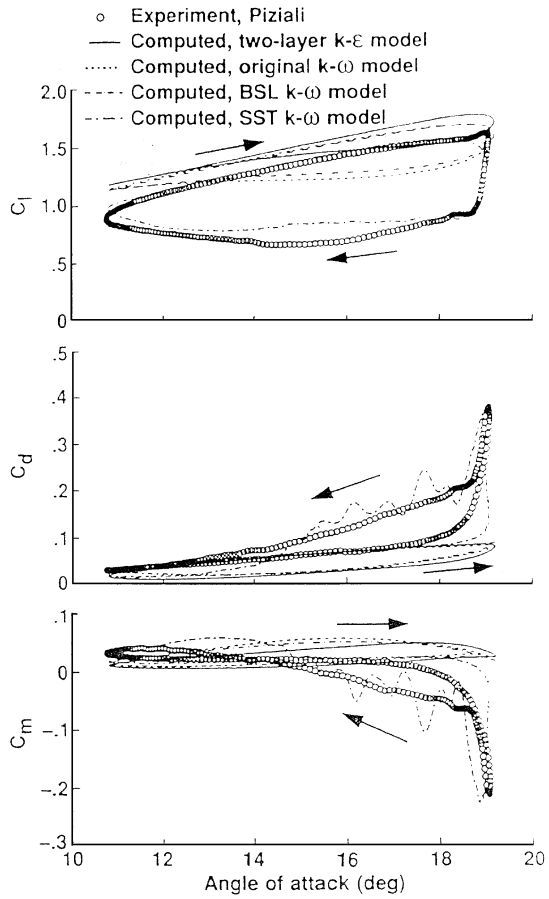

Fig. 49. Load hysteresis loops for deep-stall computed with two-equation turbulence models; $M = 0.3$, $\alpha(t) = 15 + 4.2^\circ \sin(\omega t)$, $k = 0.1$, NACA 0015 airfoil $\mathrm{Re_c} = 2 \times 10^6$ [from Ref. (44)].

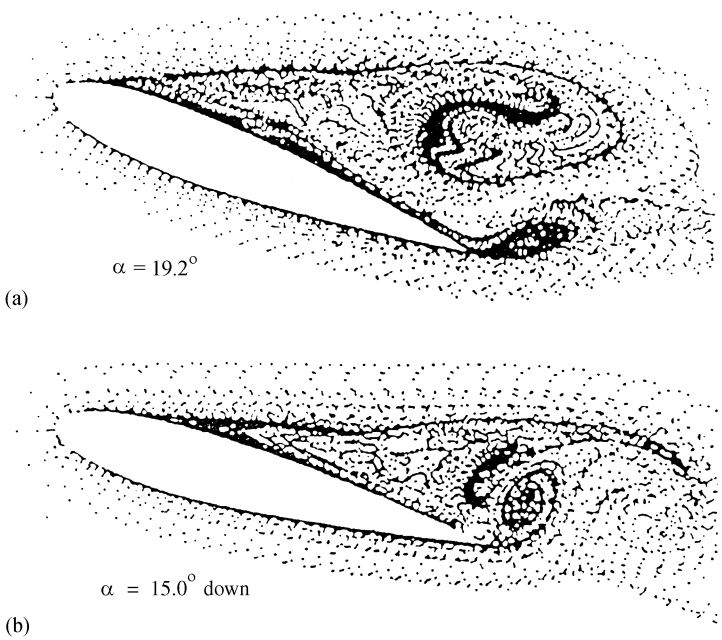

Fig. 50. Dynamic stall during the downstroke shown by snapshots of convected particles: (a) $\alpha = 19.2^\circ$ and (b) $\alpha = 15.0^\circ$; $M = 0.3$, $\alpha(t) = 15 + 4.2^\circ \sin(\omega t)$, $k = 0.1$, NACA 0015 airfoil $\mathrm{Re_c} = 2 \times 10^6$ [from Ref. (44)].

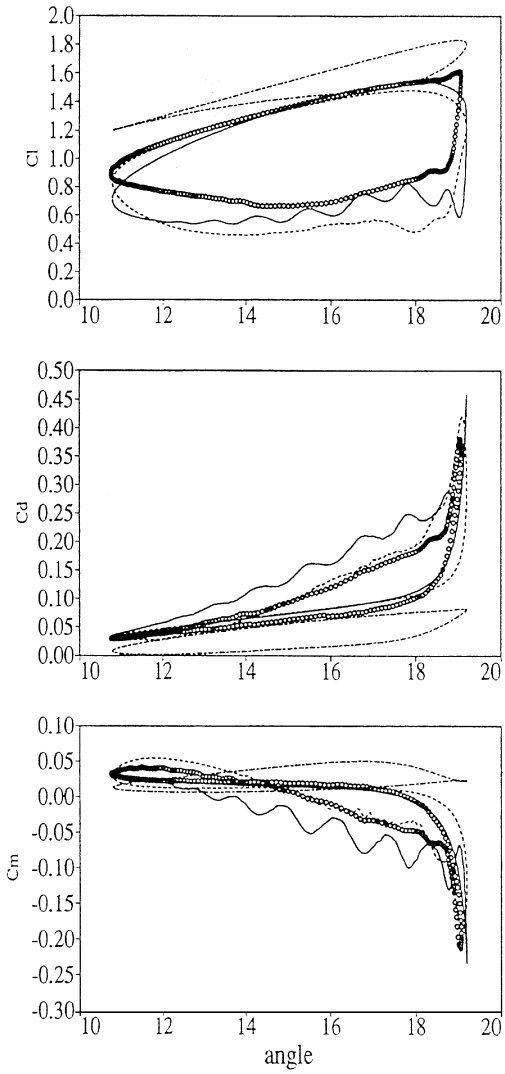

Fig. 51. Load hysteresis loops for deep-stall computed with the B–L, S–A and k–ε turbulence models; $M = 0.3$, $\alpha(t) = 15 + 4.2^\circ \sin(\omega t)$, $k = 0.1$, NACA 0015 airfoil $\mathrm{Re}_c = 2 \times 10^6$ [from Ref. (94)].

transitional flow region was obtained by an effective eddy viscosity. Scaling of the computed turbulent eddy viscosity in the transitional flow region was obtained by multiplying the computed eddy viscosity with the Chen-Thyson[26] intermittency function. The transitional flow computation of Fig. 55 shows a better agreement with the experiment compared to the fully turbulent computation.

It is shown in Figs 42 and 43 that fully turbulent flow computations for the light dynamic stall oscillation, $\alpha(t) = 10 + 5^\circ \sin(\omega t)$ are unable to reproduce all the hysteresis effects obtained in the experiment even when the oscillation amplitude is increased. In Ref. (44) a similar computation with oscillation amplitude increased to 5.5° was performed using the S–A and B–B one-equation turbulence models. It was found, however, that the computed loads even though they are in reasonable agreement with the measured lift and pitching moment hysteresis loops failed to predict the drag increase at the end of the downstroke. A computation, therefore, was performed where the leading-edge transitional flow region was approximately modeled as follows. The transition location was specified at the grid point where the maximum suction peak occurs. The transitional region was computed from the one-equation turbulence model by specifying zero production in the laminar flow region and a transitional flow region where the eddy viscosity increased progressively to the fully

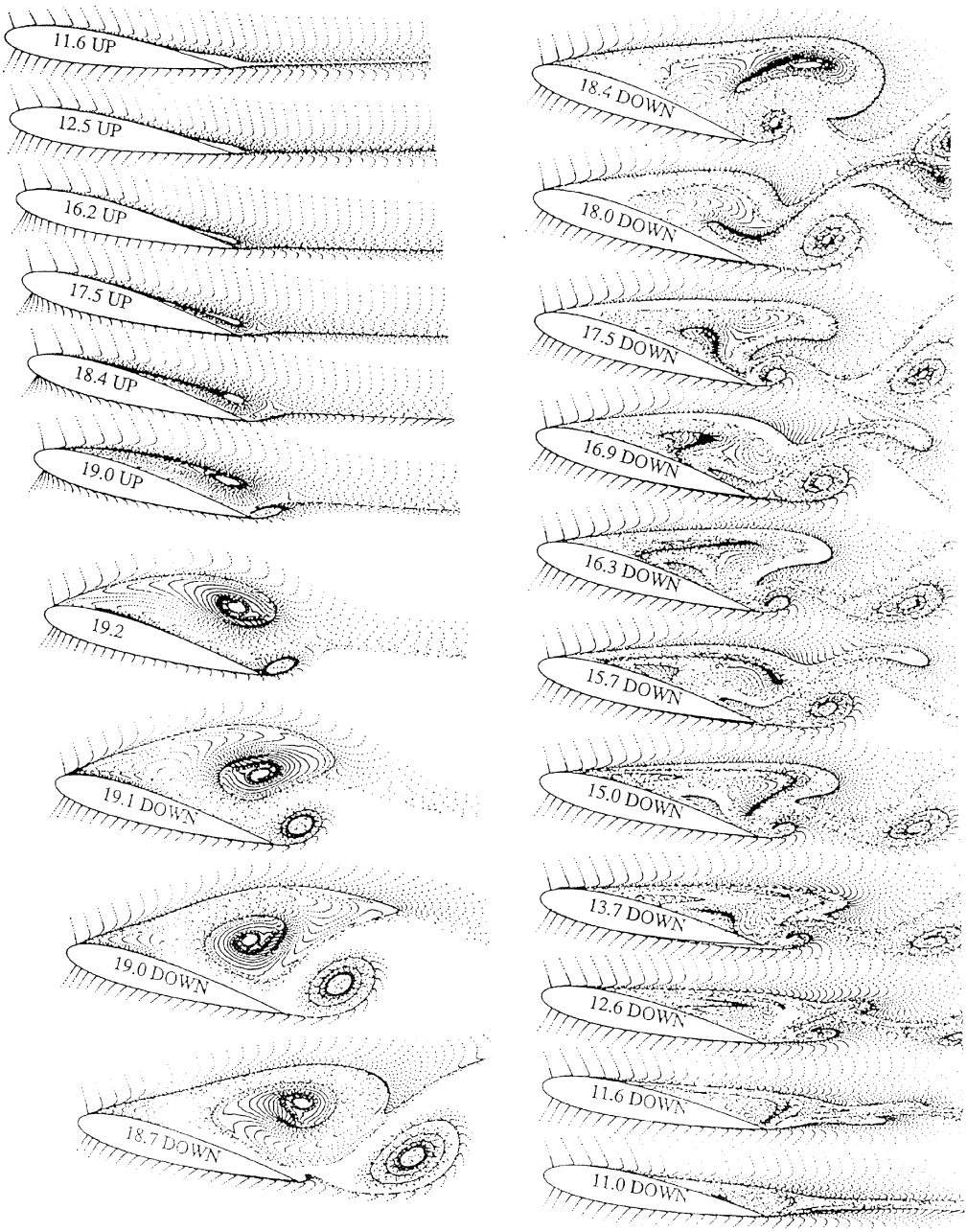

Fig. 52. Dynamic stall development shown by snapshots of convected particles; $M = 0.3$, $\alpha(t) = 15^\circ + 4.2^\circ \sin(\omega t)$, $k = 0.1$, NACA 0015 airfoil $\mathrm{Re}_c = 2 \times 10^6$ [from Ref. (94)].

turbulent flow value was obtained. Computed hysteresis loops from a fully turbulent and a transitional flow solution are compared with the experiment in Fig. 55. It is seen that the transitional flow solution closely predicts the experimental values during the upstroke but there are some discrepancies during the downstroke where the computed transitional flow fails to capture the complex reattachment process. A comparison of the surface pressure coefficient distributions of the experiment and the fully turbulent and transitional flow computations is shown in Fig. 56. It is evident that the fully turbulent solution predicts a much higher suction peak. The effect of transition was further verified[46] in later numerical investigations for different airfoils, oscillation amplitudes and reduced frequencies. An example of these computations for a case relevant to stall flutter[45] is shown in

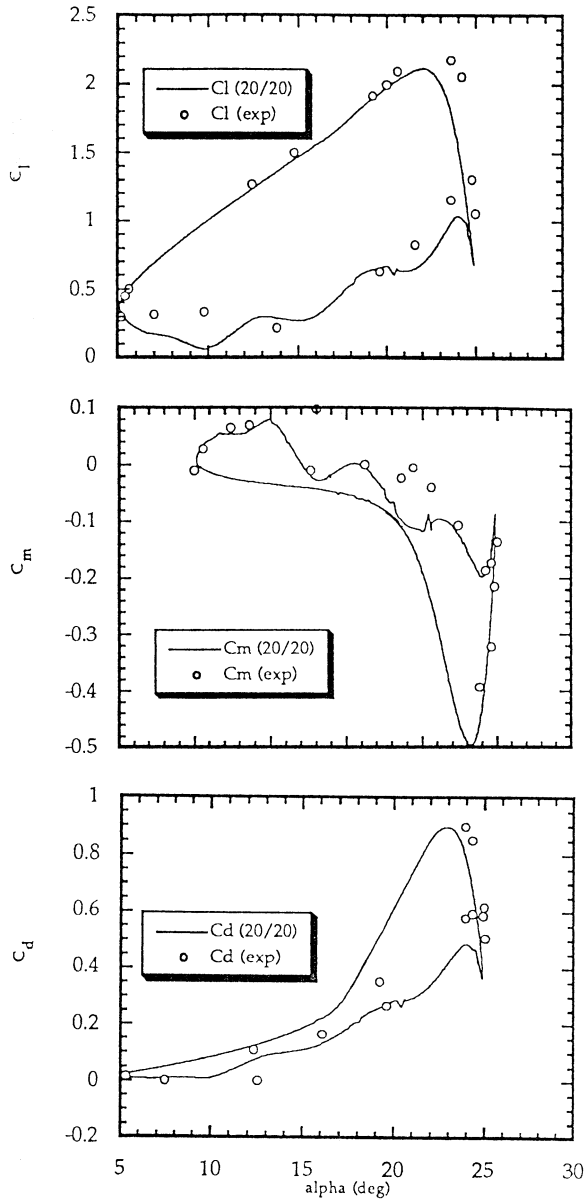

Fig. 53. Comparison of the computed load hysteresis loops with the experiment [from Ref. (81)].

Fig. 57. The load hysteresis effects obtained from a fully turbulent and a transitional flow computation are shown in Fig. 58. It is again seen that the computation fails to predict the experimental values during the downstroke.

Further investigations of transitional low Reynolds number steady and unsteady flows were performed by VanDyken *et al.*[154] using the Chen–Thyson transition length model in conjunction with a systematic variation of the transition onset location. A comparison of the pressure field obtained by the steady state solution with the experiment is shown in Fig. 59. The computed and measured velocities for oscillatory airfoil motion are compared in Fig. 60.

Recent computation by Ekaterinaris *et al.*[47] have used transition modeling for the computation of low Reynolds number, $Re_c = 0.4 \times 10^6$, flow of a NACA-0012 airfoil in a combined oscillatory and translatory motion. It was shown, that due to the low Reynolds number a fully turbulent flow solution fails to predict the hysteresis effect shown in the

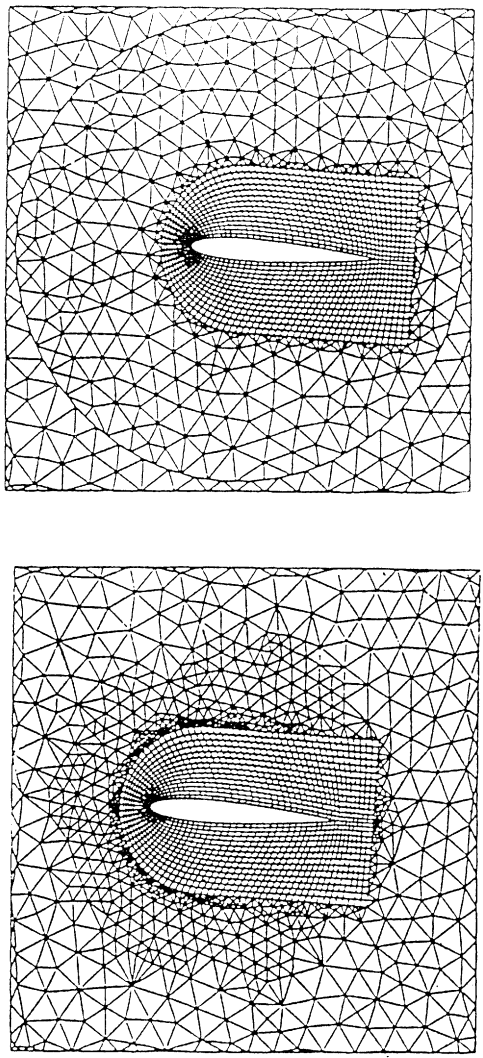

Fig. 54. Numerical mesh used for the computation of dynamic stall using a structured/unstructured approach [from Ref. (126)].

experiment. Figures 61 and 62 show comparisons of computations with the experiment for oscillation ($\alpha = 9 + 6^\circ \sin(\omega t)$) and translatory motion $V(t) = \lambda \sin(t + \pi/2)$. Both lift and drag hysteresis loops are in fair agreement with the measurements for the low reduced frequency case ($k = 0.135$, $\lambda = 0.153$), shown in Fig. 61. For the high reduced frequency case ($k = 0.314$, $\lambda = 0.356$), shown in Fig. 62, the lift hysteresis is closely predicted and qualitative agreement with the experiment is obtained for the drag hysteresis.

6.2.4. *Effect of leading-edge modifications*

Early experimental[103] and numerical investigations by Fung and Carr[58] indicated that there is a strong dependency of dynamic stall on the leading edge geometry. Grohsmeyer *et al.*[70] performed a systematic study of the sensitivity of dynamic stall onset to small changes of the leading-edge geometry of a NACA–0012 airfoil. It was found that a slightly thinner leading edge produced earlier dynamic stall. It was also concluded that there is a critical pressure gradient distribution near the suction peak triggering the dynamic-stall

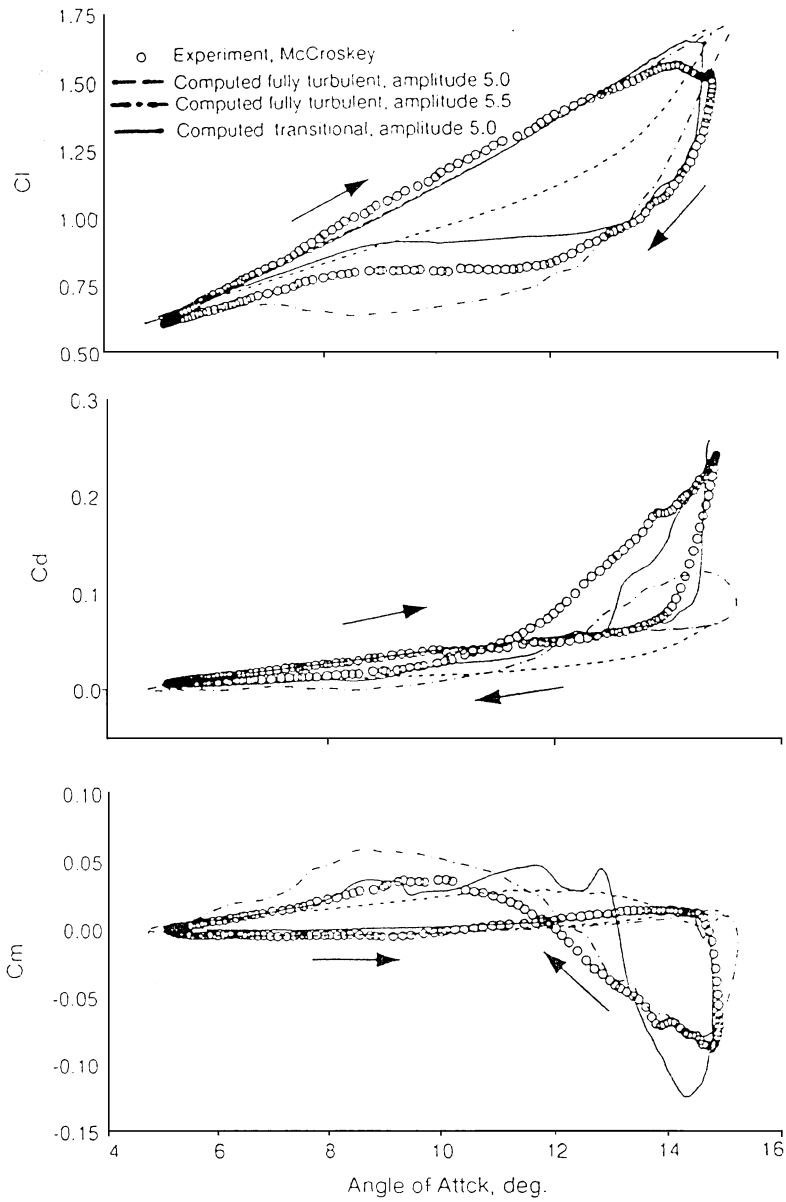

Fig. 55. Effect of leading-edge transition on the load hysteresis effects; $M = 0.3, \alpha(t) = 10 + 5.0^\circ \sin(\omega t)$, $k = 0.1$, NACA 0012 airfoil $\mathrm{Re_c} = 4 \times 10^6$ [from Ref. (44)].

onset. This pressure gradient distribution was found to be relatively independent of reduced frequency and Mach number for the values of these two parameters investigated. The computed surface pressure gradient distribution for different Mach numbers and reduced frequencies is shown in Fig. 63. A similar behavior concerning the dependency of dynamic-stall onset on pressure gradient distribution was shown in Fig. 16 using incompressible boundary-layer computations.

Recent investigations by Geissler and Sobieczky[62,63] have shown that dynamic stall can be controlled by active airfoil shape variation. They demonstrated that the flow over dynamically deforming airfoils can be controlled by nose drooping of the airfoil so that the development and shedding of the dynamic-stall vortex can be reduced or completely avoided. The effect of the nose drooping on the load hysteresis loops is shown in Figs 64 and 65. The maximum lift is nearly unchanged but the negative peak in the pitching moment

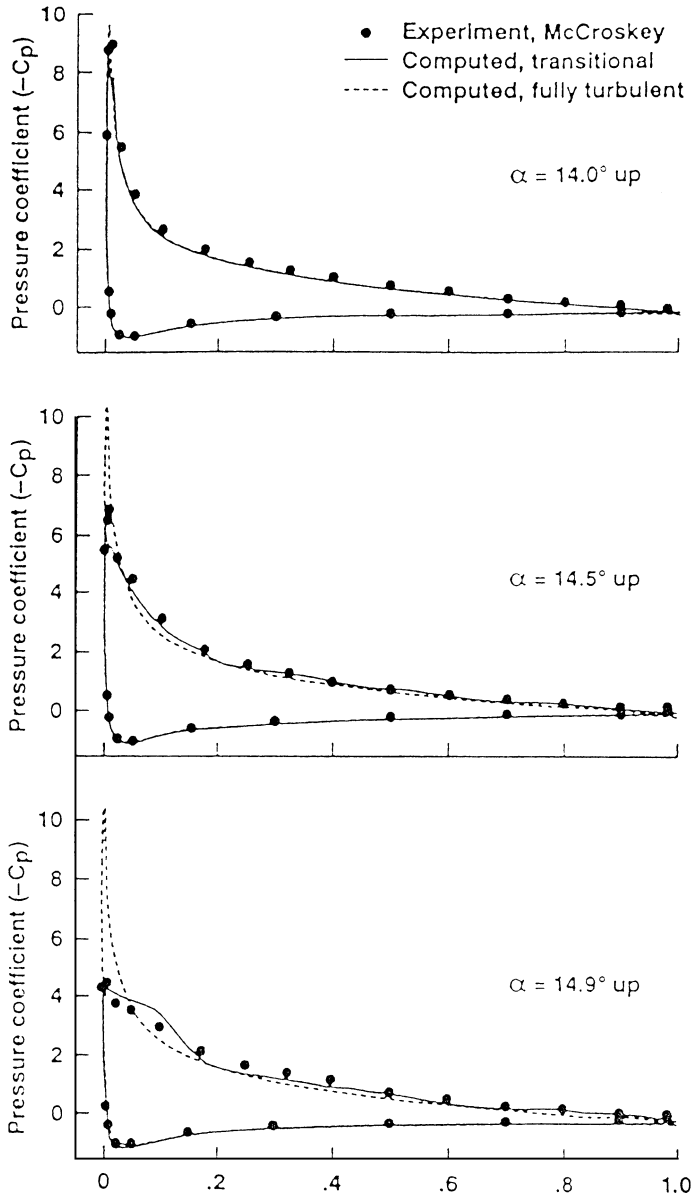

Fig. 56. Comparison of the surface pressure coefficient distributions obtained by fully turbulent and transitional flow computations with the experiment [from Ref. (44)].

loop is reduced. In addition, negative aerodynamic damping and the tendency to dangerous stall flutter is diminished.

7. THREE–DIMENSIONAL DYNAMIC-STALL COMPUTATIONS

Three-dimensional dynamic stall is of primary interest for practical applications. For example, helicopter flight and wind turbine flows require a better understanding of the three-dimensional effects near the tip region. Nevertheless, only a few numerical investigations of three-dimensional dynamic stall were performed, mainly because these computations require very large computing times. Also, there is a dearth of three-dimensional dynamic stall experiments, the most important ones being those of Piziali[120] for rectangular

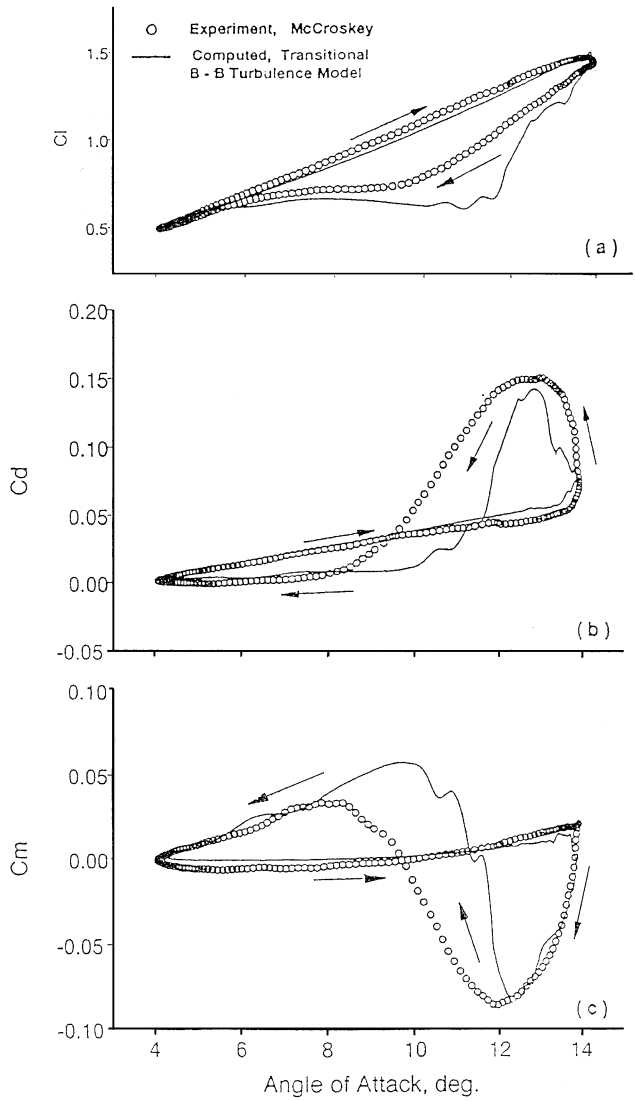

Fig. 57. Effect of leading-edge transition on the computed surface pressure coefficient distribution; $M = 0.3$, $\alpha(t) = 10 + 5.0^\circ \sin(\omega t)$, $k = 0.1$, NACA 0012 airfoil $\mathrm{Re}_c = 4 \times 10^6$ [from Ref. (45)].

wings and Lorber *et al.*[100] and Lorber[98] for swept wings. The flowfield development of a rapidly pitching rectangular wing was investigated numerically by Newsome.[116] Dynamic stall of rectangular wings in oscillatory motion was also computed in Refs (133, 170). The light stall computations of Ref. (41) were performed for an aspect ratio five wing. The flow in the experiment of Ref. (120) was tripped and a fully turbulent computation with the one equation B–B model was obtained at $\mathrm{Re}_c = 3 \times 10^6$. The numerical solution was obtained on a $161 \times 81 \times 61$ point grid along the streamwise spanwise and normal directions, respectively. The numerical results (see Figs 66 and 67) are in good agreement with the measurements for the inboard spanwise locations. At the tip, Fig. 68, only quantitative agreement was obtained because of insufficient grid resolution. The three-dimensional measurements for a 50% span location appear to be different from the two-dimensional experimental loops shown in Fig. 66. The computations indicated that three-dimensional effects during the downstroke are important up to 50% span. The numerical investigations of Salari and Roach[133] have shown qualitative agreement with the experiments. Similarly, three–dimensional numerical investigations[170] showed only qualitative features of

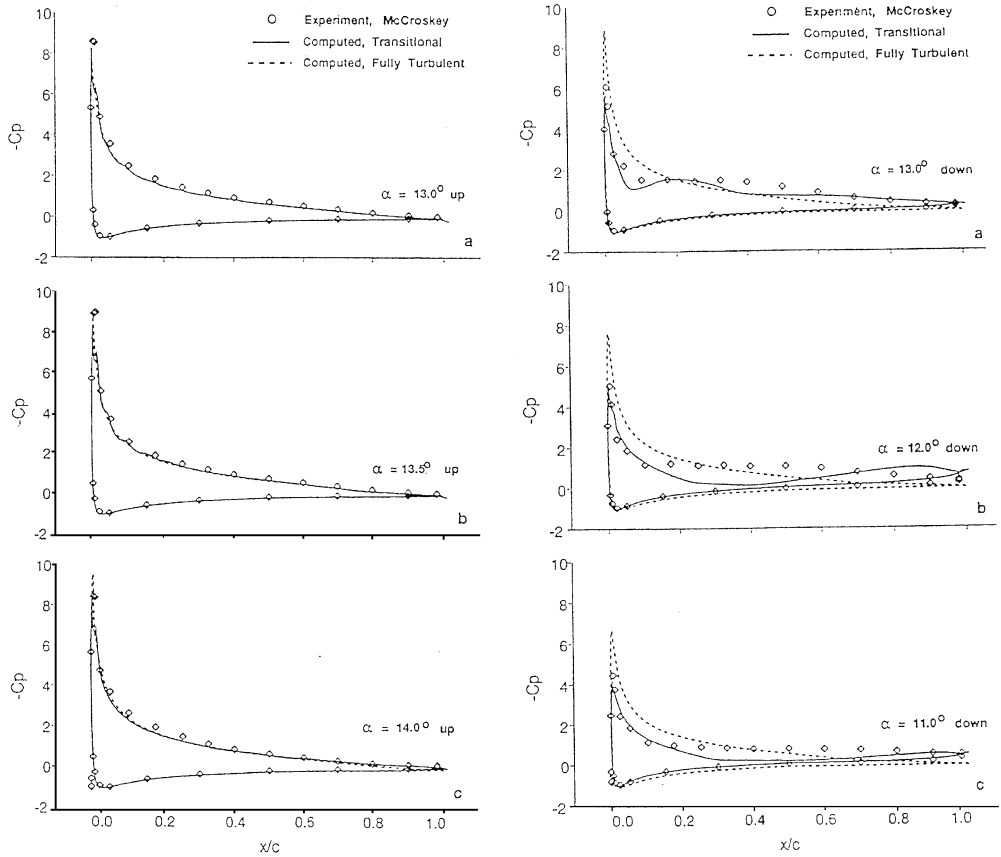

Fig. 58. Effect of leading-edge transition on the load hysteresis effects; $M = 0.3, \alpha(t) = 12 + 2.0^\circ \sin(\omega t)$, $k = 0.1$, NACA 0012 airfoil $Re_c = 4 \times 10^6$ [from Ref. (45)].

computed three-dimensional dynamic stall effects and limited comparisons with experimental measurements.

8. SUMMARY AND RECOMMENDATIONS

It is apparent from the foregoing review that significant progress has been achieved in the numerical computation of dynamic stall in recent years. However, several problem areas remain which require considerable further research. These are:

(1) *Compressibility effects.* Even at relatively low free-stream Mach numbers, locally supersonic flow develops in typical dynamic stall encounters. For example, on a NACA-0012 locally supersonic flow occurs near the leading edge as soon as the incidence angle exceeds 12° although the free–stream Mach number is only 0.4. The termination of this supersonic flow region by means of a weak shock often causes a shock boundary-layer interaction which can have a significant effect on the dynamic stall physics. The adequate modeling and the numerical resolution required to capture all the details of this interaction remain very challenging problems.

(2) *Flow reattachment.* The computation of the flow reattachment process during the airfoil downstroke shows serious deficiencies. Current turbulence models appear to be inadequate to model this type of flow. Furthermore, two-dimensional calculations are questionable because the experiments reveal significant three-dimensional flow features, especially for deep stall cases.

(3) *Transitional flow effects.* The incorporation of transitional flow effects using transitional flow modeling was found to be a key element for an improved prediction of

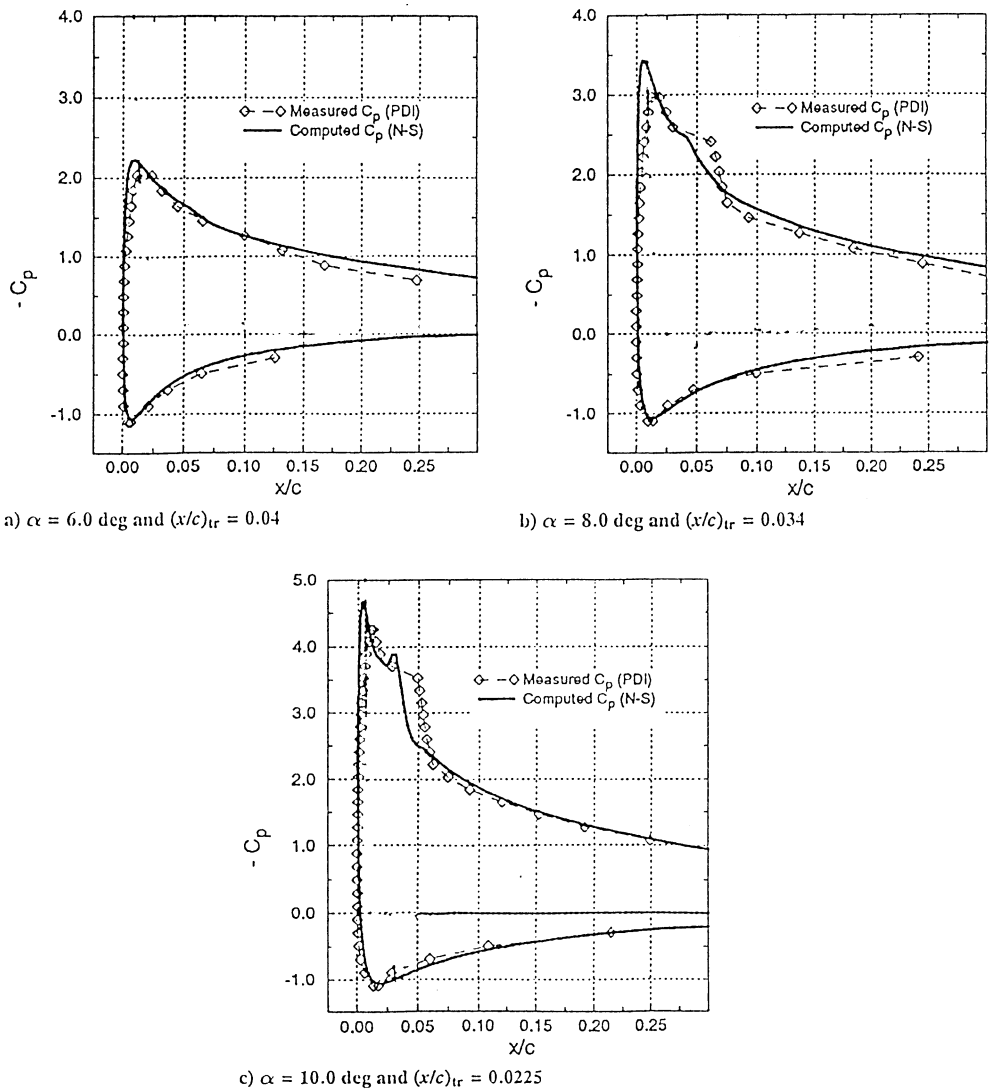

Fig. 59. Effect of leading-edge transition on the computed surface pressure coefficient distribution; $M = 0.3$, $\alpha = 6, 8$ and 10°, NACA 0012 airfoil $Re_c = 0.5 \times 10^6$ [from Ref. (154)].

the dynamic-stall hysteresis loops, even at relatively high Reynolds numbers. Unfortunately, this transition modeling is mostly based on empirical information. More work is required to improve calculation of the transitional flow region.

(4) *Transonic effects.* Transonic aileron buzz and transonic wing flutter may be caused by shock-induced flow separation and may produce nonlinear hysteresis effects. A review of the basic flow physics and of the computational methods has been given by Mabey[101] and by Edwards and Thomas.[39] Very little has been done both experimentally and computationally to obtain a better understanding of forced, unsteady, transonic, separated, flows. Clearly, improved modeling of oscillating airfoil shock-boundary-layer interaction is required for a reliable prediction of these complex flow phenomena.

(5) *Three-dimensional dynamic-stall effects.* The numerical computation of three-dimensional dynamic stall effects represents the most challenging area for future studies. The required computer resources are much larger compared to the two-dimensional cases. Furthermore, there is a definite requirement for improved transitional and turbulent flow models which need to be developed, tested and applied for the better prediction of unsteady, separated, three-dimensional flows.

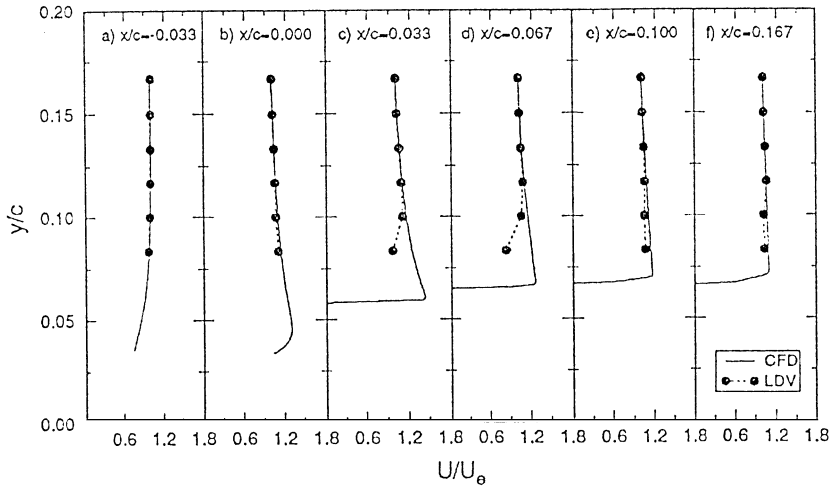

Fig. 60. Comparison of the computed and measured velocities at the airfoil leading edge; $M = 0.3$, $\alpha(t) = 10 + 2.0^\circ \sin(\omega t)$, $k = 0.1$, NACA 0012 airfoil $\mathrm{Re_c} = 0.5 \times 10^6$ [from Ref. (154)].

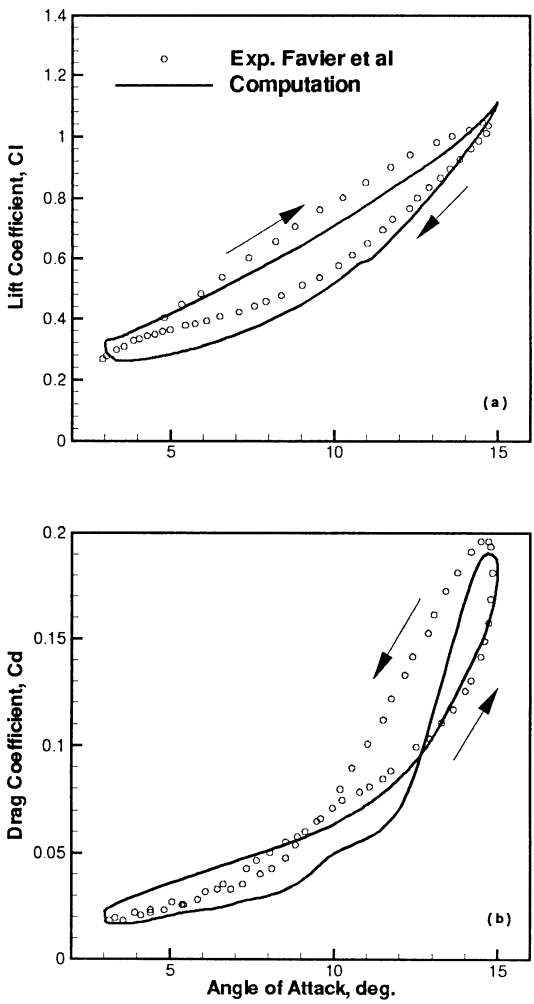

Fig. 61. Comparison of the computed loads for light stall of the NACA 0012 airfoil in combined motion with the experiment: $\alpha(t) = 9 + 6^\circ \sin(\omega t)$, $V(t) = \lambda \sin(\omega t + \phi)$, $k = 0.135$, $\lambda = 0.153$, $\phi = \pi$, $\mathrm{Re_c} = 0.4 \times 10^6$ [from Ref. (47)].

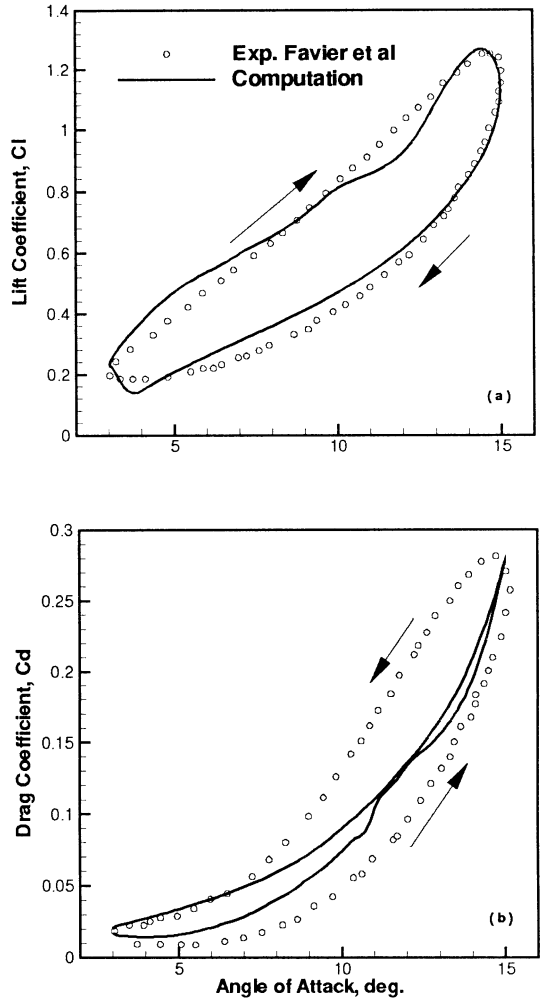

Fig. 62. Comparison of the computed loads for light stall of the NACA 0012 airfoil in combined motion with the experiment: $\alpha(t) = 9 + 6^\circ \sin(\omega t)$, $V(t) = \lambda \sin(\omega t + \phi)$, $k = 0.314$, $\lambda = 0.356$, $\phi = \pi$, $\mathrm{Re}_c = 0.4 \times 10^6$ [from Ref. (47)].

APPENDIX A: NUMERICAL SCHEMES FOR COMPRESSIBLE FLOWS

A.1. CENTRAL DIFFERENCE SCHEMES

The delta form of the implicit, approximately factorized Beam–Warming[7] algorithm is

$$\{I + h[\delta_\xi \hat{\mathbf{A}}^n_{i,j} - \mathrm{Re}^{-1}\delta_\xi \hat{\mathbf{M}}^n_{i,j} + (D_{\mathrm{imp}})_i]\}^p \times \{I + h[\delta_\eta \hat{\mathbf{B}}^n_{i,j} - \mathrm{Re}^{-1}\delta_\eta \widehat{\mathbf{N}^n_{i,j}} + (D_{\mathrm{imp}})_j]\}^p \Delta\hat{Q}^p_{i,j}$$
$$\equiv -\Delta t\{\hat{Q}^p_{i,j} - \hat{Q}^n_{i,j} + [\delta_\xi \hat{F}^n_{i,j} + \delta_\eta \hat{G}^n_{i,j}] - [\delta_\xi \hat{R}^n_{i,j} + \delta_\eta \hat{S}^n_{i,j}] + \varepsilon_e D^n_{i,j}\} \tag{A.1}$$

In these equations, central differences are used for the discretization of the inviscid fluxes. The viscous terms may be retained in both ξ- and η-directions and in a thin-layer-approximation form. The viscous terms are treated implicitly when the matrices $\hat{M}$, $\hat{N}$ are included on the left-hand side. δ is the central difference operator and h is the timestep that determines whether the algorithm is first- or second-order time accurate. The time index is denoted by n and $\Delta\hat{Q}^n_{i,j} = (\hat{Q}^{n+1}_{i,j} - \hat{Q}^n_{i,j})$. The superscript, p, in Equation (A.1) denotes subiterations which may be performed during each physical time step in order to diminish

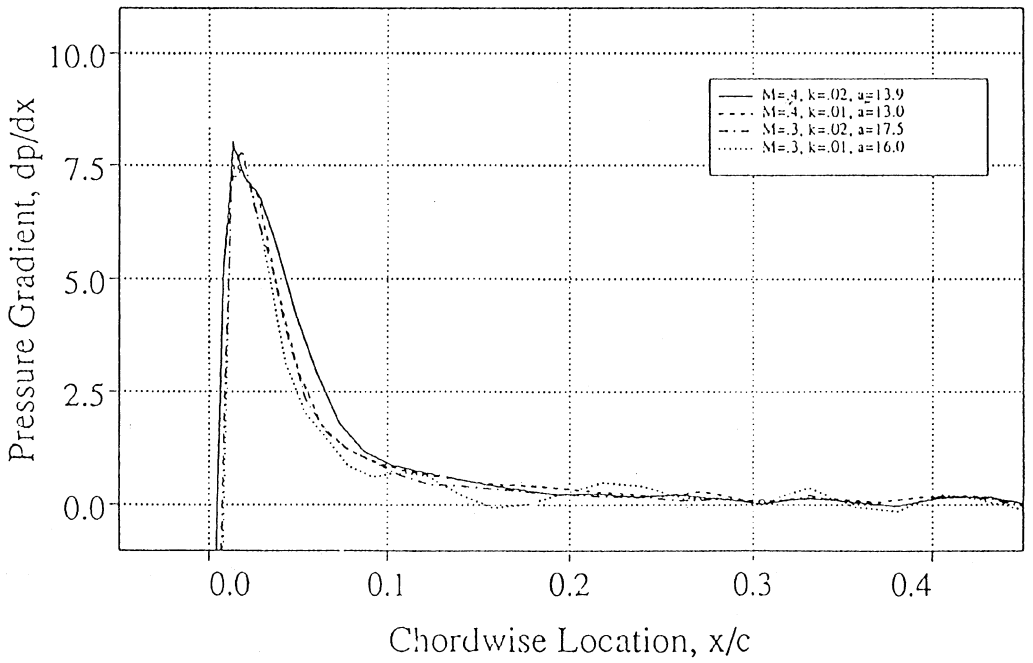

Fig. 63. Surface pressure gradient distribution [from Ref. (70)].

factorization errors. In many unsteady computations, however, it was found that subiterations are not required. The explicit inviscid fluxes are given by $\hat{E}_{i,j}$, $\hat{F}_{i,j}$ and $\hat{R}_{i,j}$, $\hat{S}_{i,j}$ are the explicit viscous fluxes. The quantities $\hat{\mathbf{A}}$, $\hat{\mathbf{B}}$, $\hat{\mathbf{M}}$ and $\hat{\mathbf{N}}$ in Equation (A.1) are flux Jacobian matrices obtained from the linearization of the left-hand side and D_{imp} and $\varepsilon_e D$ denote the implicit and explicit dissipation terms, respectively. A Jameson type,[83] blended second- and fourth-order numerical dissipation, based on the computed pressure field, is used to suppress high frequency numerical oscillations. For subsonic shock-free solutions only the fourth-order dissipation is used, while for transonic solutions the second-order dissipation is activated in the vicinity of shocks where the pressure jump has steep gradients. Both the implicit and explicit dissipation are scaled by the spectral radius. For the accuracy of calculated solutions, the added dissipation coefficients must be kept as small as possible. Recent improvements of artificial dissipation schemes allow sharper capturing of shocks and discontinuities at the expense of a larger computing time. Unsteady flow computations over three-dimensional configurations were performed by Guruswamy,[71] Chaderjian,[20] and Visbal[157] using central-difference algorithms.

A.2. UPWIND SCHEMES

The scheme discussed in the previous section is based on central-space discretization. These schemes are symmetric with respect to a change in sign of the Jacobian eigenvalues and do not have the ability to distinguish upstream from downstream influences. As a result, the physical propagation of disturbances along the characteristics is not taken into account in the definition of the numerical scheme. For this reason, second-order central difference schemes produce oscillations in the vicinity of sharp flow gradients and discontinuities. These numerical oscillations are damped out by adding artificial dissipation or numerical smoothing. In order to eliminate these shortcomings an entire class of upwind schemes has been constructed. These schemes incorporate the physical properties of the flow equations into the discretized formulation. Upwind techniques cover a variety of approaches such as flux-vector splitting and flux-difference splitting. The former introduces information about the flow character into the numerical scheme based only on the sign of

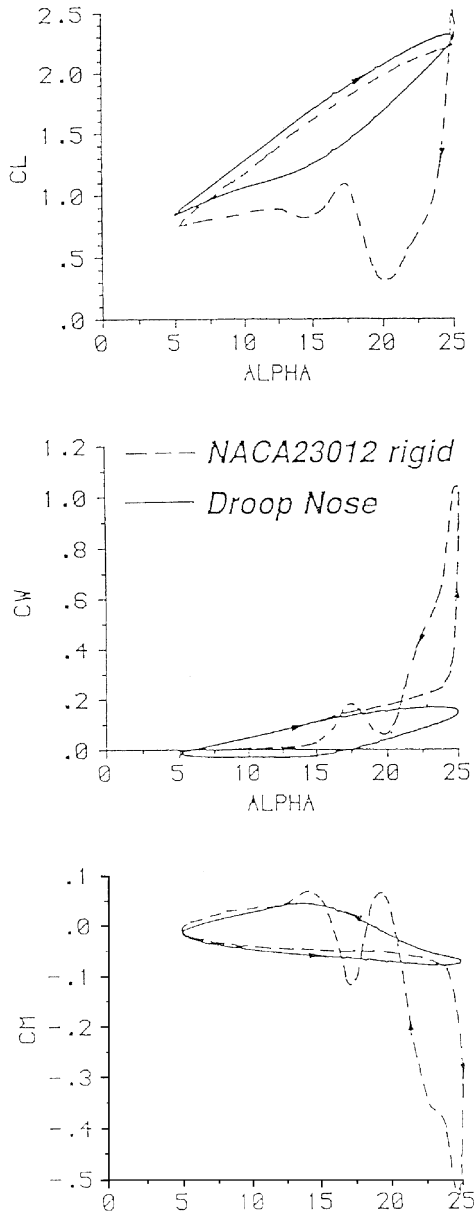

Fig. 64. Effect of nose drooping for $M = 0.1$ [from Ref. (63)].

eigenvalues. The flux terms are split and discretized directionally according to the sign of the associated propagation speeds. This is the essence of Steger–Warming [144] flux-vector splitting described in the next section. The flux difference splitting schemes introduce a higher level of physical properties into their definition. They can be defined following the Godunov[67] scheme where the conservative variables are considered piecewise constant over the mesh cells at each time step. The Godunov method determines the time evolution by the exact solution of the Riemann (shock tube) problem at the computational cell boundaries, and introduces properties derived from the exact local solution of the Euler equations in the numerical discretization. The scope of this presentation is not to analyze the merits and deficiencies of various upwind schemes. Therefore, in this section only several of the most popular upwind schemes used for dynamic stall computation are presented. Approximately factorized, implicit algorithms based on the Steger–Warming[144] flux vector splitting as well as implicit forms of approximate Riemann solvers of Roe[129] and Osher[118] are briefly described.

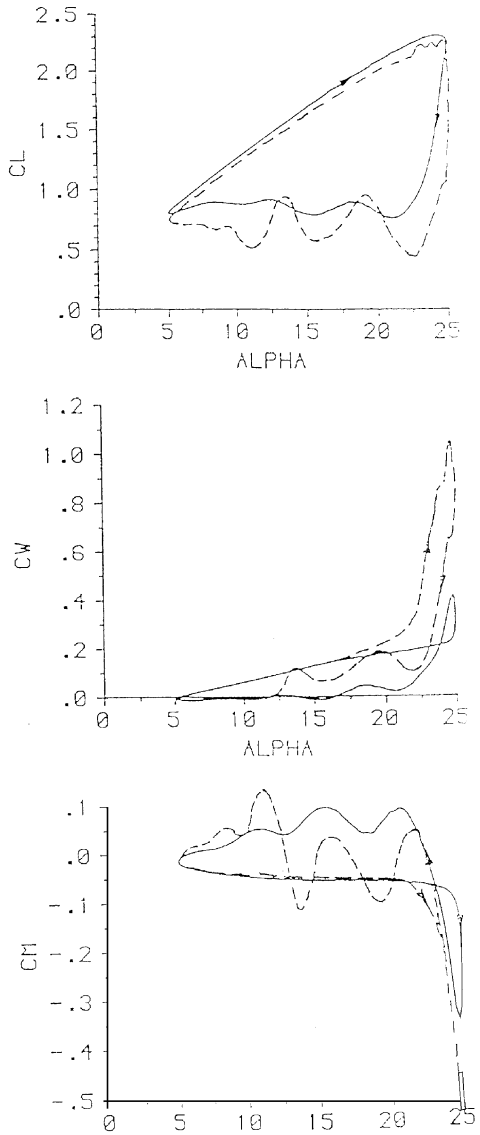

Fig. 65. Effect of nose drooping for $M = 0.3$ [from Ref. (63)].

A.3. FLUX–VECTOR SPLITTING

The Steger–Warming[144] upwind scheme defines splitting of the fluxes according to the signs of the eigenvalues. The flux vector **F**, for example, is divided into two parts each of which has a Jacobian matrix whose eigenvalues are all of the same sign. The Steger–Warming flux vector splitting has been implemented in a two-factor partially flux split numerical algorithm in the OVERFLOW code. Upwinding is performed along the main flow direction and central differencing is used in the other two space directions. The two-factor algorithm has the following form:

$$[I + h\delta_\xi^b(A^+)^n + h\delta_\zeta C^n - h\mathrm{Re}^{-1}\bar{\delta}_\zeta J^{-1}M^n J - D_i|_\zeta]$$

$$\times [I + h\delta_\xi^f(A^-)^n + h\delta_\eta B^n - D_i|_\eta](Q^{n+1} - Q^n)$$

$$= -\Delta t\{\delta_\xi^b(F^+)^n + \delta_\xi^f(F^-)^n + \delta_\eta G^n + \delta_\zeta H^n + \mathrm{Re}^{-1}\delta_\zeta S^n\} - D_e a \qquad \text{(A2)}$$

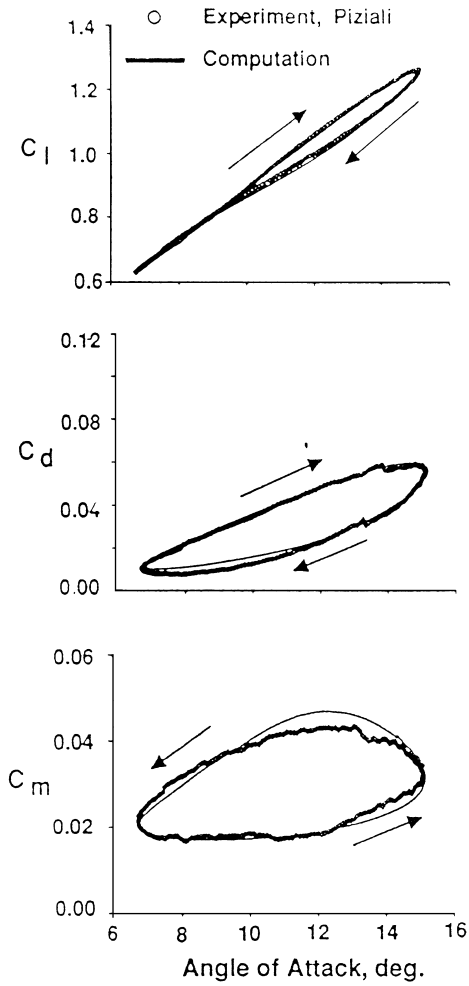

Fig. 66. Comparison of the computed load hystereses at 50% span location with the experiments; $M = 0.3, \alpha(t) = 15 + 4.2^\circ \sin(\omega t), k = 0.1$, NACA 0015 airfoil $\mathrm{Re_c} = 2 \times 10^6$ [from Ref. (44)].

where $F^+ = A^+ Q, F^- = A^- Q, F = F^+ + F^-, A^+ = P\Lambda^+ P^{-1}, A^- = P\Lambda^- P^{-1}$, and Λ^+, Λ^- contain only positive or negative eigenvalues, respectively, and Steger–Warming flux splitting defines

$$\Lambda^+ = \frac{\Lambda + |\Lambda|}{2}$$

$$\Lambda^- = \frac{\Lambda - |\Lambda|}{2} \tag{A3}$$

the explicit D_e and implicit D_i dissipation terms are added in the directions where central differences are used.

A.4. FLUX–DIFFERENCE SPLITTING

The following factorized, iterative, implicit, algorithm has been implemented with various flux difference upwind schemes such as Roe's scheme and Osher's scheme:

$$\begin{aligned}
&[I + h_\xi(\nabla_\xi^b \widehat{A_{i,j}^+} + \Delta_\xi^f \widehat{A_{i,j}^-})]^p \\
&\times [I + h_\eta(\nabla_\eta^b \widehat{B_{i,j}^+} + \Delta_\eta^f \widehat{B_{i,j}^-} - \mathrm{Re}^{-1}\delta_\eta \widehat{M_{i,j}})]^p \times (\tilde{Q}_{i,j}^{p+1} - \tilde{Q}_{i,j}^p) \\
&= -[(\tilde{Q}_{i,j}^p - Q_{i,j}^n) + h_\xi(\hat{F}_{i+1/2,j}^p - \hat{F}_{i-1/2,j}^p) \\
&+ h_\eta(\hat{G}_{i,j+1/2}^p - \hat{G}_{i,j-1/2}^p) - \mathrm{Re}^{-1} h_\eta(\hat{S}_{i,j+1/2}^p - \hat{S}_{i,j-1/2}^p)]
\end{aligned} \tag{A4}$$

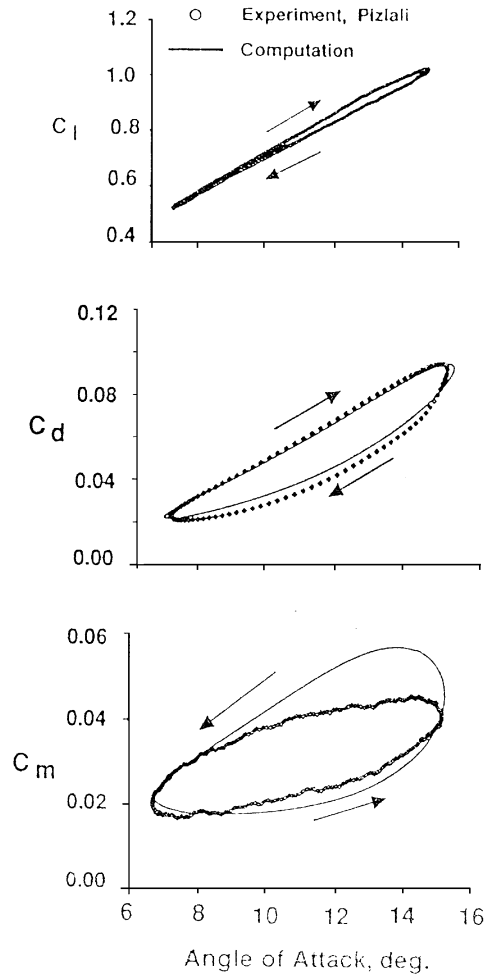

Fig. 67. Comparison of the computed load hystereses at 80% span location with the experiments; $M = 0.3, \alpha(t) = 15 + 4.2^\circ \sin(\omega t), k = 0.1$, NACA 0015 airfoil $\mathrm{Re_c} = 2 \times 10^6$ [from Ref. (41)].

In this equation, $h_\xi = \Delta\tau/\Delta\xi$, etc., $\tilde{A}^\pm = (\partial\tilde{F}/\partial\tilde{Q})$, etc., are the flux Jacobian matrices, and Δ, ∇, and δ are the forward, backward and central difference operators, respectively. The quantities $\widehat{A^\pm_{i,j}}\,\widehat{B^\pm_{i,j}}$ are Jacobian matrices from the linearization of the right-hand side, and $\hat{F}_{i+1/2,j}$, $\hat{G}_{i,j+1/2}$, and $\hat{S}_{i,j+1/2}$ are numerical fluxes.

High-order upwind-biased formulas may be used for the right-hand side numerical fluxes $\hat{F}_{i,k+1/2}$, and $\hat{G}_{i,k+1/2}$. The numerical fluxes for a second-order accurate upwind-biased scheme are given by

$$\begin{aligned}\hat{F}_{i+1/2,k} &= \tilde{F}_{i+1/2,k} + \tfrac{1}{2}[\Delta F^+_{i-1/2,j} - \Delta F^+_{i-3/2,j}] - \tfrac{1}{2}[\Delta F^-_{i+3/2,j} - \Delta F^-_{i+1/2,k}] \\ &= \tilde{F}(Q_{i,k}, Q_{i+1,j}) + \tfrac{1}{2}[\Delta F^+(Q_{i-1,j}, Q_{i,j}) - \Delta F^+(Q_{i-2,j}, Q_{i-1,j})] \\ &\quad - \tfrac{1}{2}[\Delta F^-(Q_{i+1,j}, Q_{i+2,j}) - \Delta F^-(Q_{i,j}, Q_{i+1,j})] \end{aligned} \tag{A5}$$

and for a third-order accurate upwind-biased scheme are given by

$$\begin{aligned}\hat{F}_{i+1/2,j} &= \tilde{F}_{i+1/2,j} + \tfrac{1}{6}[\Delta F^+_{i-1/2,j} + 2\Delta F^+_{i+1/2,j}] - \tfrac{1}{6}[\Delta F^-_{i+3/2,j} + 2\Delta F^-_{i+1/2,j}] \\ &= \tilde{F}(Q_{i,k}, Q_{i+1,k}) + \tfrac{1}{6}[\Delta F^+(Q_{i-1,j}, Q_{i,j}) + 2\Delta F^+(Q_{i,j}, Q_{i+1,j})] \\ &\quad - \tfrac{1}{6}[\Delta F^-(Q_{i+1,j}, Q_{i+2,j}) + 2\Delta F^-(Q_{i+1,j}, Q_{i,j})] \end{aligned} \tag{A6}$$

In the above equations, $\tilde{F}$ is the first-order accurate numerical flux.

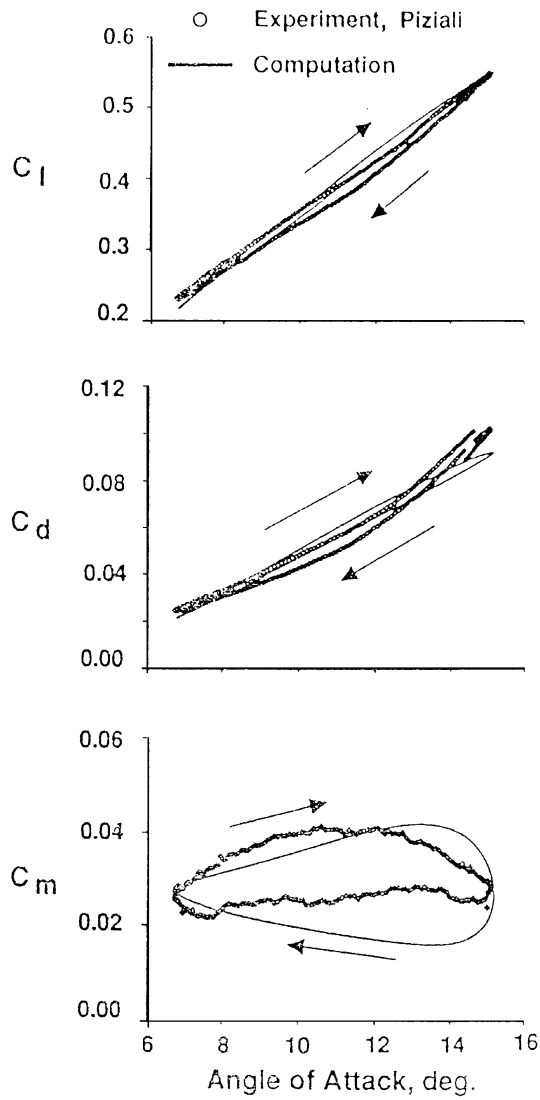

Fig. 68. Comparison of the computed load hystereses at 89% span location with the experiments; $M = 0.3, \alpha(t) = 15 + 4.2^\circ \sin(\omega t), k = 0.1$, NACA 0015 airfoil $\mathrm{Re}_c = 2 \times 10^6$ [from Ref. (41)].

A.4.1. Osher scheme

The first-order numerical flux for the Osher scheme[118] is evaluated as follows:

$$\tilde{F}^{(\mathrm{O})}_{i+1/2,j} = \frac{1}{2}\left[F_{i,j} + F_{i+1,j} - \int_{Q_i}^{Q_{i+1}} \{ F_q^+ - F_q^- \} \, \mathrm{d}Q \right] \tag{A7}$$

where $F_q = F_q^+ + F_q^-$, $F_q^\pm = (\partial F/\partial Q)^\pm$, and $\Delta F^\pm$ are the corrections to obtain high–order accuracy. Two intermediate points are introduced between i and $i+1$ in order to evaluate the integral of Equation (A7). These intermediate points define subpaths along which the integral is evaluated. Limiting of the high-order discretizations is obtained by modifying the fluxes $\Delta F^\pm$. The gradient of an entropy function $V(Q) = -\rho \log(p/\rho\gamma)$ is used to switch the order of accuracy at regions of extrema. Computations of two- and three-dimensional unsteady flows with the Osher scheme were performed recently by Ekaterinaris.[41,44]

A.4.2. Roe scheme

The first-order numerical flux $\tilde{F}$ for the Roe scheme can be obtained from the same integral of Equation A7 (which simplifies to)

$$\tilde{F}^{(\mathrm{R})}_{i+1/2,j} = \tfrac{1}{2}\left[F_{i,j} + F_{i+1,j} - \sum_k |\lambda_{(k)}| \partial W_k r^{(k)}\right] \tag{A8}$$

where $\lambda_{(k)}$ are the eigenvalues and $r^{(k)}$ are the eigenvectors of the Roe matrix and ∂W_k are wave amplitudes. The flux differences $\Delta F^{\pm}$ are evaluated by Roe's scheme as

$$\Delta F^{\pm}(Q_{i,j,k}, Q_{i+1,j,k}) = \tilde{A}^{\pm}(Q_{i+1/2,j,k}) \times (Q_{i+1,j,k} - Q_{i,j,k}) = \tilde{A}^{\pm}(\bar{Q}) \times (Q_{\mathrm{R}} - Q_{\mathrm{L}}) \tag{A9}$$

Roe's approximate Riemann solver assumes a linear wave decomposition and uses an average state $\bar{Q}$ defined as a function of the left and right states Q_{L} and Q_{R} to evaluate $F^{\pm}$. Roe-type flux-difference splitting requires explicit evaluation of the intermediate state $\bar{Q}$ for the construction of the flux-difference quantities. The intermediate state or average value for each cell $\bar{Q}$ is calculated using the Roe variables:

$$\begin{aligned}
\bar{\rho} &= \sqrt{\rho_{\mathrm{L}}} + \sqrt{\rho_{\mathrm{R}}} \\
\bar{u} &= (u_{\mathrm{L}}\sqrt{\rho_{\mathrm{L}}} + u_{\mathrm{R}}\sqrt{\rho_{\mathrm{R}}})/\bar{\rho} \\
\bar{v} &= (v_{\mathrm{L}}\sqrt{\rho_{\mathrm{L}}} + v_{\mathrm{R}}\sqrt{\rho_{\mathrm{R}}})/\bar{\rho} \\
\bar{w} &= (w_{\mathrm{L}}\sqrt{\rho_{\mathrm{L}}} + w_{\mathrm{R}}\sqrt{\rho R})/\bar{\rho} \\
\bar{h} &= (h_{\mathrm{L}}\sqrt{\rho_{\mathrm{L}}} + h_{\mathrm{R}}\sqrt{\rho_{\mathrm{R}}})/\bar{\rho} \\
\bar{h} &= e + p/\rho
\end{aligned} \tag{A10}$$

where the associated speed of sound is $\bar{c}^2 = (\gamma - 1)[\bar{h} - 0.5(u^2 + v^2)]$.

Flux limiting of the high-order flux corrections can be obtained with a minmod TVD scheme.[21] The flux-limited values of $\Delta F^{\pm}$ are

$$\begin{aligned}
\Delta F^{-}_{i+3/2} &= \mathrm{minmod}\left[\Delta F^{-}_{i+3/2}, \beta \Delta F^{-}_{i+1/2}\right] \\
\Delta F^{-}_{i+1/2} &= \mathrm{minmod}\left[\Delta F^{-}_{i+1/2}, \beta \Delta F^{-}_{i+3/2}\right] \\
\Delta F^{+}_{i+1/2} &= \mathrm{minmod}\left[\Delta F^{+}_{i+1/2}, \beta \Delta F^{+}_{i-1/2}\right] \\
\Delta F^{+}_{i-1/2} &= \mathrm{minmod}\left[\Delta F^{+}_{i-1/2}, \beta \Delta F^{+}_{i+1/2}\right]
\end{aligned} \tag{A11}$$

the minmod operator is defined as

$$\mathrm{minmod}[x, y] = \mathrm{sign}(x) \max[0, \min\{|x|, y\,\mathrm{sign}(x)\}] \tag{A12}$$

and the parameter β is in the range $1 \leqslant \beta \leqslant (3 - \phi)/(1 - \phi)$ where $\phi = \frac{1}{2}$ for the second-order scheme and $\phi = \frac{1}{3}$ for the third-order scheme.

Expansion shocks which violate the entropy condition but are admissible solutions of Roe's scheme are removed with the following modifications of the eigenvalues:

$$\lambda^{(k)}_{i+1/2} = \begin{cases} \lambda^{(k)}, & \lambda^{(k)} \geqslant \varepsilon \\ \dfrac{1}{2}\left[\varepsilon + \dfrac{\lambda^{(k)}}{\varepsilon}\right], & \lambda^{(k)} \leqslant \varepsilon \end{cases}$$

where $\varepsilon = \max[0, (\lambda_{i+1/2} - \lambda_i), (\lambda_{i+1} - \lambda_{i+1/2})]$.

Three-dimensional unsteady computations using the Roe scheme were performed by Ekaterinaris.[46] Evaluation of Roe's numerical flux is faster than the evaluation of the integral involved in Osher's flux evaluation. Osher's scheme assumes a "shock tube" solution across the interval where $A^{\pm}$ is piecewise continuous. Across the shock contact discontinuity and expansion fan the Osher scheme predicts the flux better. As a result,

Osher's scheme is superior to Roe's scheme at supersonic speeds. Roe's scheme, on the other hand, is twice as fast compared to Osher's scheme and predicts well the flux at transonic speeds. For unsteady computations it was found[43] that the Osher scheme allows larger time steps and the overall computing time becomes comparable to the one required by Roe's scheme.

Full linearization of the right-hand side for both Osher's and Roe's schemes requires a large computational effort. Therefore, linearization of the left-hand side is obtained by Steger–Warming[144] flux-vector splitting of the flux Jacobian matrices A and B. For both schemes, the errors introduced by the linearization and approximate factorization of the left hand side of the numerical algorithm may be minimized by performing Newton subiterations at each time-step during the unsteady calculations. The approximation to $\tilde{Q}^{n+1}$ at each subiteration is the quantity $\tilde{Q}^{p}$. When $p \geqslant 2$, during a given level of subiteration to convergence, $\tilde{Q}^{p} = \tilde{Q}^{n+1}$, but when $p = 1$ and no subiterations are performed, then $\tilde{Q}^{p} = \tilde{Q}^{n}$, and $\tilde{Q}^{p+1} = \tilde{Q}^{n+1}$. Numerical experiments have demonstrated[44] that because of the small time steps used, Newton subiterations do not improve the accuracy of the solution even though they improve convergence. It was also found that the two time-level numerical scheme does not increase the accuracy of the unsteady calculations.

The viscous fluxes $S_{i,k+1/2}$ are computed with central differences. In the normal practice of the thin-layer approximation for viscous terms, only the terms in the normal direction ($\hat{S}$) are retained because of the large flow gradients in that direction. Calculations performed retaining the viscous terms for the η-direction alone and keeping terms for both the ξ and η-directions showed very little difference between the solutions. Therefore, all calculations are performed by retaining the viscous terms only in the η-direction. The computational cost was not significantly increased for keeping explicit viscous terms in both directions. However, numerical experiments have demonstrated that implicit treatment of the streamwise viscous term, $\hat{\mathbf{M}}$ in addition to the normal viscous term $\hat{\mathbf{M}}$ (see Equations (A1) and (A4)), does not contribute to the accuracy of the solution but results in increased computational cost.

A.4.3. Numerical grid

Body fitted C-type computational grids were used in most calculations. The grid points were clustered at the body surface in the normal direction. For deep dynamic stall calculations the leading and trailing edge regions were also refined. The spacing of the first grid point at the surface in the normal direction varied from 0.00005 to 0.000005 chord lengths. The grid boundaries in most computations were typically located at 15–20 chords away from the airfoil in all directions. Further details about the grids used for the numerical solution of laminar and turbulent dynamic-stall flowfields can be found in the cited references. The unsteady solution was usually performed on a moving grid and the orientation of the moving frame with respect to the fixed frame changed at each instant of time. Therefore, after the grid was moved to the new location at each time step all metrics were recomputed.

A.4.4. Boundary conditions

The boundary conditions for the unsteady computations can be updated explicitly. For subsonic inflow–outflow, the flow variables at the boundaries can be evaluated using one-dimensional Riemann-invariant extrapolation. At the inflow boundary there is one incoming and three outgoing characteristics. Therefore, three variables, the density, the normal velocity, and the pressure are specified and the fourth variable, the axial velocity is extrapolated from the interior. At the outflow boundary there are one incoming and three outgoing characteristics and only one quantity, the pressure, is specified while the others are extrapolated from the interior. For the density, a simple first-order extrapolation is used. On the body surface a non-slip condition is applied for the velocities, and the contravariant velocity components in the body-fixed coordinate system are set equal to zero. It should be

noted that the surface velocity is non-zero because of the body motion through the unsteady metrics. For C-type grids averaging of the flow variables at the wake cut is used.

APPENDIX B: NUMERICAL SOLUTION OF INCOMPRESSIBLE FLOWS

B.1. VELOCITY–VORTICITY FORMULATION

The velocity–vorticity formulation of the incompressible Navier–Stokes equations was used for the solution of unsteady flows over airfoils undergoing dynamic stall. This formulation consists of the vorticity transport equation and an integral equation for velocity. Since the vorticity field is closely related to the viscous stress and vorticity is absent in the potential flow zone, the vorticity transport equation needs only to be solved in the viscous flow zone. In addition, attached boundary layer and detached recirculating flow regions in the viscous flow zone may be treated individually. The velocity vector in the viscous flow zone can be evaluated explicitly from the integral equation for velocity. The velocity–vorticity formulation thus confines the computations into the viscous flow zone only. The confinement of the computations and the zonal approach greatly reduce the computational demands and lead to an efficient zonal solution procedure.

The vorticity transport equation in a rotating reference frame attached to the solid body is

$$\frac{\partial \boldsymbol{\omega}}{\partial t} = -(V_{\mathrm{R}} \cdot \nabla_{\mathrm{R}})\boldsymbol{\omega} + \nabla_{\mathrm{R}}^2(v_e \boldsymbol{\omega}) \tag{B1}$$

where the subscript 'R' indicates that the velocity vector and the differentiations are defined in the rotating reference frame. The vorticity transport equation describes the kinetic transport of vorticity. All the vorticity in the fluid domain originates from the fluid boundary in contact with a solid, and spreads into the fluid domain by diffusion and is then transported away from the solid boundary by both convection and diffusion processes. These processes produce a region of non-zero vorticity around the solid body. However, in high Reynolds number flows, a large region of the flow domain is vorticity free and Equation (B1) needs to be solved only in the region containing vorticity. Furthermore, in high Reynolds number flows, the vortical region can conveniently be separated into attached and detached flow regions. In the attached flow region, the flow direction is tangential to the solid surface and the diffusion of vorticity along the flow direction is negligible compared to its convection. In this region, the boundary-layer simplification which neglects the streamwise diffusion of vorticity is justified.

The relationship between the vorticity and velocity fields at any given instant of time constitutes the kinematic aspect of the problem. Wu[164] has shown that Equation (B1) can be recast into an integral representation for the velocity vector in terms of the vorticity field and the velocity boundary conditions:

$$\mathbf{V}(\mathbf{r}) = -\frac{1}{2\pi}\int_R \frac{\boldsymbol{\omega}_0 \times (-\mathbf{r})}{|-\mathbf{r}|^2}\,\mathrm{d}R_0 + \frac{1}{2\pi}\int_B \frac{(\mathbf{V}_0 \cdot \mathbf{n}_0)(-r) - (\mathbf{V}_0 \times \mathbf{n}_0)\times(-\mathbf{r})}{|-\mathbf{r}|^2}\,\mathrm{d}B_0 \tag{B2}$$

where $\mathbf{r}$ is the position vector, the subscript '0' denotes the variables and the integration in the $\mathbf{r}_0$ space, R is the flow domain, B is the boundaries of the flow domain and $\mathbf{n}$ is the unit normal vector on B directed away from the domain R. In particular, the flow domain for the airfoil problem is doubly connected and B consists of B_s, the solid boundary and B_∞, the far-field boundary. It should be noted that the far-field boundary conditions are applied analytically at the limit as r_0 goes to infinity.

As mentioned earlier, Equation (B1) needs to be solved only in the region containing vorticity. Thus, the velocity values during the numerical solution are needed only in this region. Since the velocity vector at any point in the flowfield can be evaluated explicitly by Equation (B2), computations are conveniently confined only to the vortical flow zone. The vorticity free potential flow zone is excluded from the computations.

Equation (B1) is parabolic in time and elliptic in space. At any instance of time, a boundary value problem is solved and the vorticity values on the inner and outer boundaries need to be prescribed. The outer boundary is taken to be outside the region containing vorticity. However, if the outer boundary cuts through the vortical wake, then the gradient of vorticity in the direction normal to the boundary is assumed to be zero, which allows vortices to pass through the downstream boundary at the local velocity.

The inner boundary is the solid surface, B_s, and the vorticity is generated continuously at this surface. In Ref. (165), it has been shown that the solid boundary vorticity values can be determined through the kinematic relationship between the instantaneous velocity and vorticity fields. It should be noted that the kinematic relationship, Equation (B2), is valid in both the solid region S and the fluid region R. Therefore, the vorticity field throughout S and R must be such that the velocity in S as computed by Equation (B2) should agree with the prescribed solid body motion. Equation (B2) applied on B_s and the principle of conservation of vorticity give rise to the relations suitable for the evaluation of the surface vorticity distribution:

$$\frac{1}{2\pi}\int_{B_s^+}\frac{\boldsymbol{\omega}_{s_0}\times(-\mathbf{r}_s)}{|-\mathbf{r}_s|^2}\,dR = -\mathbf{V}(r_s,t) - \frac{1}{2\pi}\int_{R-B_s^+}\frac{\boldsymbol{\omega}_0\times(-\mathbf{r}_s)}{|-\mathbf{r}_s|^2}\,dR_0 + \frac{1}{2\pi}\int_B\frac{(\mathbf{V}_0\cdot\mathbf{n}_0)(-\mathbf{r}_s)-(\mathbf{V}_0\times\mathbf{n}_0)\times(-\mathbf{r}_s)}{|-\mathbf{r}_s|^2}\,dB_0 \tag{B3}$$

where B_s^+ is a boundary adjacent to B_s where the surface vorticity distribution is evaluated, ω_s is the surface vorticity and $\mathbf{r}_s$ is a point on B_s. With prescribed $\mathbf{V}(\mathbf{r}_s, t)$ and having evaluated the interior vorticity distribution in $R - B_s^+$, the surface vorticity distribution, ω_s, can be evaluated through Equation (B3). Note that Equation (B3) is a vector equation and either component can be used to solve for ω_s.

B.2. PSEUDO-COMPRESSIBILITY METHOD

An implicit time-integration method of the Navier–Stokes equations is used in the artificial compressibility formulation. Steady-state solutions of Equation (22) do not require time accuracy. Therefore, the pseudo-time derivative can be discretized by a first-order, implicit formula as follows:

$$\left[\frac{I}{\Delta\tau}+\left(\frac{\partial R}{\partial Q}\right)^m\right]\Delta Q = -R^m \tag{B4}$$

where

$$R = (\hat{F}-\hat{F}_v)_\xi + (\hat{G}-\hat{G}_v)_\eta$$

and $\Delta Q = Q^{m+1} - Q^m$. For steady-state solutions, Equation (38) is marched implicitly in time until convergence is obtained. The left-hand side of Equation (38) can be approximately factorized and the Beam–warming algorithm may be used for time integration. Rogers *et al.*[131] used the Gauss–Seidel line-relaxation method for steady-state and unsteady incompressible flow solutions with the artificial compressibility or pseudo-compressibility method. This method was originally proposed by Chakravarthy[21] and MacCormack.[102]

Extension of the pseudocompressibility method to time–accurate solutions, as suggested in Ref. (110), can be obtained as follows. The time derivatives in the momentum equations are differenced using the following second-order, three-time level formula:

$$\frac{3\mathbf{u}^{n+1}-4\mathbf{u}^n+\mathbf{u}^{n-1}}{2\Delta t} = -R^{n+1} \tag{B5}$$

These equations are solved for a divergence-free velocity field at the $n+1$ time level by introducing a pseudo-time level which is denoted by the superscript m in the

following artificial compressibility relation:

$$\frac{\partial p}{\partial \tau} = -\beta \nabla \cdot \mathbf{u}^{n+1,m+1} \tag{B6}$$

Iterative solution of this equation is performed so that $\mathbf{u}^{n+1,m+1}$ approaches $\mathbf{u}^{n+1}$ as $\nabla \cdot \mathbf{u}^{n+1,m+1}$ approaches zero.

The delta form of the linearized solution algorithm, for both steady-state and time-accurate solutions, is given by

$$\left[\frac{I_{\mathrm{tr}}}{J} + \left(\frac{\partial R}{\partial Q}\right)^{n+1,m}\right] \times (Q^{n+1,m+1} - Q^{n+1,m})$$

$$= -R^{n+1,m} - \frac{I_m}{\Delta t}(1.5Q^{n+1,m} - 2Q^n + 0.5Q^{n-1}) \tag{B7}$$

where $I_{\mathrm{tr}} = \mathrm{diag}\,[\Delta t/\Delta\tau, 1.5, 1.5, 1.5]/\Delta t$ and $I_m = \mathrm{diag}[0, 1, 1, 1, 1]$. For steady-state solutions the internal iteration index is dropped and only the term R remains on the right-hand side of Equation (B7).

Addition of the pressure time derivative in the continuity equation introduces artificial waves. Therefore, a space discretization method capable of following and properly propagating these artificial waves through the computational domain must be chosen. In addition, these waves must be carried out of the computational domain using appropriate boundary conditions. Space discretization must be performed with a scheme which provides some dissipative mechanism which automatically suppresses the oscillations caused by the non-linear convective fluxes. Central difference space discretization requires additional artificial dissipation[83] to avoid odd–even coupling caused by the non-linear inviscid terms. Upwind space differencing, on the other hand, enables to follow the waves introduced by artificial compressibility and inherently has a dissipative mechanism which automatically suppresses oscillations. Roe[129] upwind flux differencing suppresses oscillations and is independent of externally specified parameters, as opposed to central difference schemes with added artificial dissipation. Even though upwind schemes require in general more computation time per time step they converge faster. As a result, savings in the overall computing time are obtained.

Roe's flux-difference splitting[129] approximates the convective flux derivative by

$$\frac{\partial \hat{F}}{\partial \xi} \approx \frac{\tilde{F}_{i+1/2} - \tilde{F}_{i-1/2}}{\Delta \xi} \tag{B8}$$

where $\tilde{F}_{i+1/2}$ is a numerical flux given by

$$\tilde{F}_{i+1/2} = \tfrac{1}{2}[\hat{F}(Q_{i+1}) + \hat{F}(Q_i) - f_{i+1/2}] \tag{B9}$$

In this equation the first two terms yield the second-order, central-difference scheme and the term $f_{i+1/2}$ represents an upwinding dissipative term depending on the flux difference of the positive and negative traveling waves. First-order upwinding is obtained by

$$f_{i+1/2} = \Delta F^{+}_{i+1/2} - \Delta F^{-}_{i+1/2} \tag{B10}$$

In practice, a first-order scheme is too diffusive to allow solutions with a reasonable number of grid points. Therefore, here the following third- and fifth-order schemes are used. A third-order scheme is obtained when the term $f_{i+1/2}$ is computed as

$$f_{i+1/2} = -\tfrac{1}{3}[\Delta F^{+}_{i-1/2} - \Delta F^{+}_{i+1/2} + \Delta F^{-}_{i+1/2} - \Delta F^{-}_{i+3/2}] \tag{B11}$$

and the fifth-order scheme is obtained for

$$f_{i+1/2} = -\tfrac{1}{30}[-2\Delta F^{+}_{i-3/2} + 11\Delta F^{+}_{i-1/2} - 6\Delta F^{+}_{i+1/2} - 3\Delta F^{+}_{i+3/2}$$
$$+ 2\Delta F^{-}_{i+5/2} - 11\Delta F^{-}_{i+3/2} + 6\Delta F^{-}_{i+1/2} + 3\Delta F^{-}_{i-1/2}] \tag{B12}$$

where the flux difference is computed as

$$\Delta F^{\pm}_{i+1/2} = A^{\pm}(\bar{Q}) \times (Q_{i+1} - Q_i) \tag{B13}$$

In Equation (B13) $\bar{Q}$ are the Roe average variables, which for incompressible flow become $\bar{Q} = (Q_{i+1} + Q_i)/2$, and A^+, A^- are the parts of the flux Jacobian matrix $A = \partial \hat{F}/\partial \hat{Q}$ with only positive and only negative eigenvalues, respectively, as follows:

$$A^{\pm} = X \Lambda^{\pm} X^{-1} \tag{B14}$$

Here X and X^{-1} are the right and left eigenvectors of the flux Jacobian matrix A and $\Lambda^{\pm}$ is a diagonal matrix containing both positive and negative eigenvalues on the main diagonal. The nonlinear inviscid flux derivatives $\partial \hat{F}/\partial \xi$, etc., may be also discretized using central differences. In this case, a numerical dissipation term similar to the term added in the compressible flow case must be used to damp non-linear oscillations.

APPENDIX C: TURBULENCE MODELS

Turbulence models used for dynamic-stall computations are summarized. Turbulent flow in light and deep dynamic-stall flows was modeled by algebraic models. These models are easy to implement and they are included in many codes, they do not cause numerical difficulties and they are still used for dynamic-stall predictions. The algebraic models and the Johnson–King turbulence model are presented first in Section C.1. Recently developed one-equation turbulence models have shown superior performance compared to algebraic models for dynamic-stall flows where nonequilibrium flow effects are important. These turbulence models are presented in Section C.2. Finally, two-equation turbulence models used for dynamic-stall computations are presented in Section C. 3.

C.1. ALGEBRAIC MODELS

The algebraic models are the simplest of all turbulence models. They use the Boussinesq eddy-viscosity approximation and Prandtl's mixing length hypothesis in their formulation. These models give the Reynolds stress tensor as a product of an eddy viscosity and the mean rate of strain tensor. The eddy viscosity is usually computed in terms of a mixing length and in contrast to the molecular viscosity depends upon the computed flowfield. The algebraic turbulence models are built on the mixing length hypothesis which is a rough approximation of turbulent flows. Therefore, they are unlikely to possess a very wide range of applicability. It is surprising that despite their theoretical shortcomings the mixing length models do an excellent job of reproducing experimental measurements of certain dynamic-stall flows. In the next sections, two algebraic models based on the modifications and improvements of mixing length hypothesis introduced by Van Driest, Clauser and Klebanoff are described. A recently developed algebraic model derived from the Renormalization Group theory of turbulence, the algebraic RNG model, which has shown improvements in predicting dynamic stall compared to other algebraic models, is also presented.

C.1.1. Cebeci–Smith (C–S) model

The Cebeci–Smith[18] model is a two-layer model. The turbulent eddy viscosity μ_T, of this model is given by separate expressions for the inner and outer layers as follows:

$$\mu_T \begin{cases} \mu_{T_i}, & y \leqslant y_m \\ \mu_{T_o}, & y \geqslant y_m \end{cases}$$

where y_m is the normal distance location for which $\mu_{T_i} = \mu_{T_o}$. The value of the inner layer eddy viscosity is computed by

$$\mu_{T_i} = \rho l^2 \left(\frac{\partial u}{\partial y}\right)$$
$$l = \kappa y[1 - e^{-(y/A)}] \tag{C1}$$

and the outer layer eddy viscosity μ_{T_o} is given by

$$\mu_{T_o} = \alpha \rho U_e \delta^* F_{Kleb}(y; \delta)$$
$$F_{Kleb}(y; \delta) = [1 + (y/\delta)^6]^{-1} \tag{C2}$$

where U_e is the velocity at the boundary-layer edge, $\delta^* = \int_0^\delta (1 - u/U_e)\,dy$ is the displacement thickness, and δ is the boundary layer thickness. F_{Kleb} is the Klebanoff intermittency function, and the parameters of the model are

$$\kappa = 0.40, \quad \alpha = 0.0168, \quad N = (1 - 11.8p^+)^{(1/2)}, \quad p^+ = \frac{\nu U_e}{u_\tau^3}\frac{dU_e}{dx}\, A = 26\left(\frac{\nu}{N}\right)u_\tau^{-1}$$

where $u_\tau = \sqrt{\tau_w/\rho}$ is the frictional velocity and $\tau_w = \mu(\partial u/\partial y)_w$ where the subscript w denotes the value at the wall and $\nu = \mu/\rho$ is the kinematic viscosity.

C.1.2. Baldwin–Lomax (B–L) model (3)

This is a two-layer, zero-equation model which was formulated in order to circumvent the complications involved in the Cebeci–Smith model, caused by the need for boundary-layer properties, such as δ, δ^* and U_e, which are difficult to determine, especially for separated flows. It is the most commonly used turbulence model available in most CFD codes. Its strengths and weaknesses are well known in the CFD community; it predicts accurately steady flows with little or no separation and performs poorly if there is large flow separation, either shock-induced or otherwise. It uses an inner- and outer-layer formulation for determining the turbulent viscosity with a smooth transition that spreads over the two regions. It uses a classical mixing-length hypothesis for the inner layer with a van Driest damping function to force the eddy viscosity at the wall to zero. In the outer layer, the length scale is fixed by the location where the product of distance from the solid wall and vorticity reaches a maximum in the boundary layer. The Klebanoff intermittency factor is used to drive the eddy viscosity to zero in the outer flow away from the wall.

The eddy viscosity of the Baldwin–Lomax model[4] is also given by two separate expressions as follows

Inner layer:

$$\mu_{T_i} = \rho l^2 |\omega| l = \kappa y\,[1 - e^{-(y^+/A^+)}] \tag{C3}$$

Outer layer

$$\mu_{T_o} = \rho \alpha C_{cp} F_{wake} F_{Kleb}(y)$$
$$F_{wake} = \min\,[y_{max} F_{max}, C_{wk} y_{max} U_{dif}^2 / F_{max}]$$
$$F_{max} = \tfrac{1}{\kappa}[\max(l|\omega|)] \tag{C4}$$

where ω is the vorticity magnitude, y_{max} is the value of y at which $l|\omega|$ is maximum, U_{dif} is the difference between U_{max} in the layer and U at $y = y_{max}$, and the closure coefficients are

$$\kappa = 0.41, \quad \alpha = 0.0168, \quad A^+ = 26, \quad C_{cp} = 1.6, \quad C_{Kleb} = 0.3, \quad C_{wk} = 1.0$$

The intermittency function differs from the Cebeci–Smith model and is given by $F_{Kleb} = [1 + (C_{Kleb} y/y_{max})^6]^{-1}$.

The main difference between the Baldwin–Lomax and the Cebeci–Smith models is in the outer layer formulation, where C_{cp} and F_{wake} replaces U and δ^*. Thus, the Baldwin–Lomax model avoids the need to search for the boundary-layer edge and establishes the outer-layer length scale in terms of the computed vorticity or more precisely the point within the viscous layer where the moment of vorticity is maximum. This method, however, incurs uncertainties for complex flows where more than one maximum occurs. A successful modification of the Baldwin–Lomax model which avoids this difficulty and yields better accuracy for the computation of leading edge vortex-dominated flows was introduced by Degani and Schiff.[36]

C.1.3. RNG model

This is another algebraic eddy viscosity model, proposed recently for the closure of the Reynolds-averaged Navier–Stokes equations. It is based on the renormalization group (RNG) theory of turbulence.[169] The model, although free from uncertainties related to the experimental determination of empirical modeling constants, still requires specification of an integral length scale of turbulence, similar to the B–L model, which reduces the generality of the model. In this model the integral scale is assumed to be proportional to the boundary-layer thickness δ, and the eddy viscosity is obtained by

$$\nu = \nu_\ell \left[1 + H \left\{ \frac{\hat{a}}{\nu_\ell^3} \phi \left(\frac{1}{y} + \frac{1}{0.225\delta} \right)^{-4} - C_c \right\} \right]^{1/3} \tag{C5}$$

where $\nu = \nu_t + \nu_\ell$, the subscripts t and ℓ refer to the turbulent and laminar components, respectively, and δ is the boundary-layer thickness. It is determined as $\delta = 1.2y_{1/2}$ where $y_{1/2}$ is the normal distance from the wall at which the function $F(y)$ [see Equation (C4)] attains its half-amplitude.[86] H is the Heaviside step function and ϕ is the dissipation rate, which is determined by assuming production equals dissipation for equilibrium flows. The parameter $\hat{a} = 0.0192$ corresponds to the von Karman constant $\kappa = 0.372$ and the parameter $C_c = 75$. The turbulent eddy viscosity is then obtained by solving Equation (C5) at every point in the computational domain. In estimating the eddy viscosity with this model for airfoil flows the model is applied only to the pressure and suction side of the airfoil and the wake region is computed with the B–L model.

Algebraic models are the simplest to implement because they do not involve conceptual difficulties and usually do not cause problems with their numerical implementation and the overall convergence and stability of the algorithm. Because they are so easy to use they are included as options in most fluid dynamic codes. These models, however, work well only for the flows for which they have been fine tuned. As a result, dynamic stall computations for essentially attached flows performed with these models were quite successful. There is very little hope, however, for extrapolating beyond the established data base for which the algebraic models are calibrated. Therefore, computations performed with these models for massively separated flows failed most times to show even qualitative agreement. For these flows higher-order models presented in the following sections yield better agreement with experiments.

C.2. HALF-EQUATION MODEL

The above models, viz., the C–S, B–L and RNG models, are termed equilibrium models meaning that the eddy viscosity instantaneously adjusts to the local flow without any history effects. The next model presented is a non-equilibrium model in which the calculated eddy viscosity accounts for the upstream history of the flow. It requires the solution of an ordinary differential equation for the maximum Reynolds shear stress upon which the eddy viscosity depends. It is termed, therefore, a half-equation model as opposed to models which involve a complete field partial differential equation for some parameter of turbulence. It was formulated by Johnson and King in order to improve the predictions of shock

separated flows. From the time Johnson and King first introduced their half-equation turbulence model,[87] there have been several modifications and/or enhancements to improve their original model for separated flows. The original version[87] of this model is briefly described in the following sections.

The Johnson–King[87] model takes into account the convection and diffusion effects on the Reynolds shear stress $\overline{-u'v'}$ in the streamwise direction. The eddy viscosity is given by

$$v_t = v_{t_o}\left[1 - \exp\left(-\frac{v_{t_i}}{v_{t_o}}\right)\right] \tag{C6}$$

where v_{t_i}, v_{t_o} describe the eddy viscosity variation in the inner and outer part of the boundary layer. The inner eddy viscosity is computed as

$$v_{t_i} = D^2\,\kappa y\sqrt{(\overline{-u'v'})^{\max}}\,D = 1 - \mathrm{e}^{-(y/A^+)} \tag{C7}$$

where the constant $A^+ = 15$ rather than 26. The outer eddy viscosity is given by

$$v_{t_o} = \sigma(x)[0.0168U_e\delta^*\gamma] \tag{C8}$$

where δ^* is the boundary layer displacement thickness, γ is the Klebanoff intermittency function given by $\gamma = [1 + 5.5(y/\delta)^6]^{-1}$, and $\sigma(x)$ is obtained from the solution of an ordinary differential equation which describes the development of $\overline{-u'v'}|_{\max}$ along the path of the maximum shear stress. The effects of convection and diffusion on the Reynolds shear stress development are obtained from the solution of the following ordinary differential equation:

$$\frac{\mathrm{d}g}{\mathrm{d}x} = \frac{a_1}{2\bar{u}_m L_m}\left\{\left(1 - \frac{g}{g_{eq}}\right) + \frac{C_{dif}L_m}{a_1\,\delta[0.7 - (y/\delta)_m]}\left|1 - \sqrt{\frac{v_{t_o}}{v_{t_o,eq}}}\right|\right\} \tag{C9}$$

Here C_{dif} and a_1 are modeling constants, $\bar{u}_m$ is the maximum average mean velocity, and

$$g = [\overline{-u'v'}_m]^{-1/2}, \quad g_{eq} = [\overline{-u'v'}_{m,eq}]^{-1/2}$$

where L_m is the dissipation length evaluated as

$$L_m = \begin{cases} 0.40y & \text{for } y_m/\delta \leqslant 0.225 \\ 0.09\delta & \text{for } y_m/\delta \geqslant 0.225 \end{cases} \tag{C10}$$

The boundary-layer thickness, δ, is determined as $\delta = 1.2y_{1/2}$ where $y_{1/2}$ is the normal distance from the wall at which the vorticity function $F(y)$ [see Equation (C4)] attains its half-amplitude. The equilibrium shear stress g_{eq} in Equation (C9) is determined from the following equilibrium eddy viscosity distribution:

$$v_{t,eq} = v_{t_o,eq}\left[1 - \exp\left(-\frac{v_{t_i,eq}}{v_{t_o,eq}}\right)\right] v_{t_i,eq} = D^2\,\kappa y\sqrt{(\overline{-u'v'})_{m,eq}}\,v_{t_o,eq} = 0.0168U_e\delta^*\gamma \tag{C11}$$

where U_e is the velocity at the edge of the boundary layer.

An implicit Euler method is used for the numerical solution of Equation (C9) and the maximum shear stress at each iteration level is updated as follows:

$$\sigma(x)^{n+1} = \sigma(x)^n\,\frac{v_{t_o}^{n+1}}{v_{t_o}^n} \tag{C12}$$

In practice, solutions with the Johnson–King turbulence model are obtained as follows. The flowfield is initialized with a laminar or a turbulent solution using the Baldwin–Lomax turbulence model for the entire flowfield. Then the Johnson–King model is applied. To initiate the solution, $\sigma(x)$ in Equation (C8) is set to unity and is allowed to change according to Equation (C12). It should be noted that the Johnson–King model reduces to the Cebeci–Smith model previously presented in this section when $\sigma(x)$ is identically equal to one.

C.3. ONE–EQUATION MODELS

An attractive feature of one- and two-equation models is that they can be utilized in a more straightforward manner compared to algebraic models in both structured and unstructured flow solvers which are becoming increasingly more popular. The accuracy and the numerical robustness of these models should be further demonstrated. Among the most widely used one-equation models are the Baldwin–Barth[3] (B–B) and the Spalart–Allmaras[140] (S–A) models. The B–B model was derived from the two–equation k–ε model[90] by introducing some simplifying assumptions. The Spalart–Allmaras model was developed based on dimensional analysis and empirical criteria. An advantage of the above field–equation turbulence models compared to the algebraic and half–equation models is that they do not require evaluation of ambiguous length scales. One-equation models require numerical solution of only one partial differential equation; therefore, they are less computationally intensive compared to two-equation models. The standard versions of the Baldwin–Barth and Spalart–Allmaras turbulence models are described next.

C.3.1. Baldwin-Barth (B–B) model

The eddy viscosity of the Baldwin–Barth one-equation model[3] is given by $v_t = vc_\mu f_\mu R_T = vc_\mu f_3 \tilde{R}_T$, here R_T is the turbulent Reynolds number and $\tilde{R}_T$ the modified turbulent Reynolds number. The quantity $\tilde{R}_T$ is the solution of the following field equation:

$$\frac{D(v\tilde{R}_T)}{Dt} = (c_{\varepsilon_2} f_2 - c_{\varepsilon_1})\sqrt{v\tilde{R}_T P} + \left(v + \frac{v_t}{\sigma_\varepsilon}\right)\nabla^2(v\tilde{R}_T) - \frac{1}{\sigma_\varepsilon}(\nabla v_t)\cdot\nabla(v\tilde{R}_T) \tag{C13}$$

This is a partial differential equation for the field quantity $R_T = k^2/v\varepsilon = \tilde{R}_T f_3(\tilde{R}_T)$, and

$$\frac{1}{\sigma_\varepsilon} = (c_{\varepsilon_2} - c_{\varepsilon_1})\sqrt{c_\mu}/\kappa^2$$

$$v_t = c_\mu(v\tilde{R}_T)D_1 D_2$$

$$\mu_t = \rho v_t$$

$$f_\mu = D_1 D_2$$

$$D_1 = 1 - \exp(-y^+/A^+)$$

$$D_2 = 1 - \exp(-y^+/A_2^+)$$

$$P = v_t\left(\frac{\partial U_i}{\partial x_j} + \frac{\partial U_j}{\partial x_i}\right)\frac{\partial U_i}{\partial x_j} - \frac{2}{3}v_t\left(\frac{\partial U_i}{\partial x_j}\right)$$

$$f_2(y^+) = \frac{c_{\varepsilon_1}}{c_{\varepsilon_2}} + \left(1 - \frac{c_{\varepsilon_1}}{c_{\varepsilon_2}}\right)\left(\frac{1}{\kappa y^+} + D_1 D_2\right)\left\{\sqrt{D_1 D_2} + \frac{y^+}{\sqrt{D_1 D_2}}\left(\frac{1}{A^+}\exp(-y^+/A^+)D_2 + \frac{1}{A_2^+}\exp(-y^+/A_2^+)D_1\right)\right\}$$

where $y^+ = u_\tau y/v$ and u_τ is the skin friction velocity. The constants of the model are

$$\kappa = 0.41, \quad c_{\varepsilon_1} = 1.2, \quad c_{\varepsilon_2} = 2.0, \quad c_\mu = 0.09, \quad A^+ = 26, \quad A_2{}^+ = 10$$

This model is applied to the entire flowfield to compute the eddy viscosity.

C.3.2. Spalart–Allmaras (S–A) model

The second one-equation model recently used for the numerical solution of dynamic-stall flowfields is the Spalart–Allmaras (S–A) model.[140] The eddy viscosity is obtained from the

solution of the following partial differential equation for $\tilde{\nu}$:

$$\frac{D\tilde{\nu}}{Dt} = c_{b1}(1 - f_{t2})\tilde{S}\tilde{\nu} + \frac{1}{\sigma}[\nabla\cdot((\nu + \tilde{\nu})\nabla\tilde{\nu}) + c_{b2}(\nabla\tilde{\nu})^2] - \left[c_{w1}f_w - \frac{c_{b1}}{\kappa^2}f_{t2}\right]\left[\frac{\tilde{\nu}}{d}\right]^2 + f_{t1}\Delta U^2 \tag{C14}$$

where S is the vorticity magnitude and $\tilde{S} = S + \tilde{\nu}/\kappa^2 d^2)$ f_{v2}, $f_{v2} = 1 - \chi/(1 + \chi f_{v1})$, $f_{v1} = 1 - \chi^3/(1 + \chi^3 + c_{v1})$, $c_{v1} = 7.1$ and d is the distance to the closest wall. The other functions of the model are

$$f_{t1} = c_{t1}g_t \exp\left(-c_{t2}\frac{\omega_{tr}^2}{\Delta U^2}[d^2 + g_t^2 d_t^2]\right)$$

$$f_{t2} = c_{t3}\exp(-c_{t4}\chi^2)$$

$$g_t = \min(0.1, \Delta U/\omega_{tr}\Delta x)$$

where $\chi = \tilde{\nu}/\nu$ and ω_{tr} is used here to denote the vorticity at the wall at the boundary layer trip point. The constants of the model are

$$c_{b1} = 0.1355, \quad c_{b2} = 0.622, \quad \sigma = 2/3$$

$$c_{w1} = \frac{c_{b1}}{\kappa^2} + \frac{1 + c_{b2}}{\sigma}, \quad c_{w2} = 2.0, \quad c_{w3} = 0.3$$

$$\kappa = 0.41, \quad f_w = g\left(\frac{1 + c_{w3}^6}{g^6 + c_{w3}^6}\right)^{1/6}$$

$$g = r + c_{w2}(r^6 - r), \quad r = \frac{\nu_t}{S\kappa^2 d^2}$$

$$c_{t1} = 1.0, \quad c_{t2} = 2.0, \quad c_{t3} = 1.1, \quad c_{t4} = 2.0$$

The eddy viscosity is given as

$$\nu_t = \tilde{\nu} f_{v1}$$

and the Reynolds shear stress are given by $-\overline{u_i u_j} = 2\nu_t \sigma_{ij}$.

C.4. TWO–EQUATION MODELS

The most popular non-algebraic turbulence models are two-equation eddy-viscosity models. These models solve two transport equations, one for the turbulent kinetic energy k and another one related to the turbulent length- (or time-) scale. Among the two-equation models, the k–ε model is the most widely used today. The original Jones and Launder k–ε model[90] and its variations have been very successful in a large variety of different flow situations, but they also have a number of shortcomings. From the standpoint of aerodynamics, the most disturbing is the lack of sensitivity to adverse pressure gradients. Another shortcoming of the k–ε model is associated with the numerical stiffness of the equations when integrated through the viscous sublayer.

The k–ω model has been developed by Wilcox[162] to overcome the shortcomings of the k–ε model. This model solves one equation for the turbulent kinetic energy k and a second equation for the specific turbulent dissipation rate (or turbulence frequency) ω. The k–ω model performs significantly better under mild adverse pressure-gradient conditions than the k–ε model. Another strong point of the model is the simplicity of its formulation in the viscous sublayer. The model does not employ damping functions and has straightforward boundary conditions. This leads to significant advantages in numerical stability. The k–ω model has been validated extensively[108] for many flow cases with and without adverse pressure gradient. For all cases it was found to perform equally well or better than the k–ε model. The major shortcoming of the k–ω model is that the results of the model depend strongly on the freestream values, ω_f, that are specified outside the shear layer.

The free-stream dependency of the original Wilcox k–ω model has been investigated in detail by Menter,[108] and it has been shown that the magnitude of the eddy viscosity can be changed by more than 100% just by using different values for ω_f. This is clearly unacceptable and corrections are necessary to ensure unambiguous solutions. The standard k–ω model developed by Wilcox has been modified in Ref. (108) so that the computed solutions are insensitive to the free-stream values of ω_f. This modified model is called Baseline (BSL) k–ω model. The BSL k–ω model was further modified[109] in order to improve the predictions of separated flows with strong adverse pressure gradient. This model is called shear stress transport (SST) k–ω model. This model has been tested in Ref. (44) for a wide class of steady and unsteady separated flows and has shown good agreement with experiments. Computations of dynamic-stall flows with the SST k–ω model are shown in section 6.2.2. The basic equations for the two equation models are presented in the following section. More detailed discussion for the two equations models can be found in the original references and in the book by Wilcox.[163]

C.4.1. k–ε model

The eddy viscosity of the standard k–ε model is obtained from the turbulent kinetic energy, k, and the dissipation rate, ε, as

$$\mu_T = \rho C_\mu k^2/\varepsilon$$

where C_μ is a constant and k, ε are obtained from the solution of the following partial differential equations:

$$\rho\frac{\partial k}{\partial t} + \rho u_i\frac{\partial k}{\partial x_i} = \tau_{ij}\frac{\partial u_j}{\partial x_i} - \rho\varepsilon + \frac{\partial}{\partial x_i}\left[(\mu + \mu_T/\sigma_k)\frac{\partial k}{\partial x_i}\right]$$

$$\rho\frac{\partial \varepsilon}{\partial t} + \rho u_i\frac{\partial \varepsilon}{\partial x_i} = C_{\varepsilon_1}\frac{\varepsilon}{k}\tau_{ij}\frac{\partial u_j}{\partial x_i} - C_{\varepsilon_2}\rho\frac{\varepsilon^2}{k} + \frac{\partial}{\partial x_i}\left[(\mu + \mu_T/\sigma_\varepsilon)\frac{\partial \varepsilon}{\partial x_i}\right] \tag{C15}$$

with the following closure coefficients:

$$C_{\varepsilon_1} = 1.44, \quad C_{\varepsilon_2} = 1.92, \quad \sigma_k = 1.0, \quad \sigma_\varepsilon = 1.3$$

The k–ε model is capable of being integrated to the wall. However, it demonstrates difficulty with its numerical treatment of the near-wall region for flows more complex than a flat plate in zero pressure gradient. The numerical difficulties are caused by the numerical stiffness of the k–ε model. Therefore, k–ε formulations in many cases use wall functions and set the first computational point off the surface at relatively large distance. For this surface region the flow is assumed to be in equilibrium with the remaining flowfield and it is defined algebraically without requiring numerical solution. A zonal approach can be also used with the k–ε model, where the flow adjacent to the surface is computed with a mixing length formulation or with another turbulence model and the k–ε model equations are used as above. A successful implementation of the k–ε model was obtained when the Wilcox k–ω model is used as a sublayer model and the k–ε model for the rest of the flowfield.

C.4.2. Original k–ω model

The original k–ω model[162] is given by

$$\frac{D\rho k}{Dt} = \tau_{ij}\frac{\partial u_i}{\partial x_j} - \beta^*\rho\omega k + \frac{\partial}{\partial x_j}\left[(\mu + \sigma_k^W\mu_t)\frac{\partial k}{\partial x_j}\right]$$

$$\frac{D\rho\omega}{Dt} = \frac{\gamma^W}{\nu_t}\tau_{ij}\frac{\partial u_i}{\partial x_j} - \beta\rho\omega^2 + \frac{\partial}{\partial x_j}\left[(\mu + \sigma_\omega^W\mu_t)\frac{\partial \omega}{\partial x_j}\right] \tag{C16}$$

The constants of the original Wilcox model are

$$\sigma_k^{\mathrm{W}} = 0.5, \quad \sigma_\omega^{\mathrm{W}} = 0.5, \quad \beta^{\mathrm{W}} = 0.0750, \quad \beta^* = 0.09,$$

$$\kappa = 0.41, \quad \gamma^{\mathrm{W}} = \beta^{\mathrm{W}}/\beta^* - \sigma_\omega^{\mathrm{W}}\kappa^2/\sqrt{\beta^*}$$

The k–ω model has been tested for many simple flows[163] and has shown significant improvements compared to algebraic, one-equation and the standard k–ε model.

C.4.3. BSL k–ω model

The (BSL) model is identical to the k–ω model of Wilcox[162] for the inner region of a boundary layer (up to approximately $\delta/2$) and gradually changes to the standard k–ε model in the outer wake region. In order to enable computations with one set of equations, the k–ε model was first transformed into a k–ω formulation. The blending between the two regions is performed by a blending function that gradually changes from one to zero in the desired region. No *a priori* knowledge of the flowfield is necessary to perform the blending. The function also ensures that the k–ε formulation is selected for free shear layers. The performance of the new (BSL) model is very similar to that of the Wilcox k–ω model for adverse pressure gradient boundary-layer flows (and therefore better than that of the k–ε model), but without the undesirable free-stream dependency. For free shear layers the new model is basically identical to the k–ε model, which predicts spreading rates more accurately than the k–ω model. The Baseline (BSL) k–ω model is

$$\frac{\mathrm{D}\rho k}{\mathrm{D}t} = \tau_{ij}\frac{\partial u_i}{\partial x_j} - \beta^*\rho\omega k + \frac{\partial}{\partial x_j}\left[(\mu + \sigma_k\mu_t)\frac{\partial k}{\partial x_j}\right]$$

$$\frac{\mathrm{D}\rho\omega}{\mathrm{D}t} = \frac{\gamma}{\nu_t}\tau_{ij}\frac{\partial u_i}{\partial x_j} - \beta\rho\omega^2 + \frac{\partial}{\partial x_j}\left[(\mu + \sigma_\omega\mu_t)\frac{\partial\omega}{\partial x_j}\right] + 2(1 - F_1)\rho\sigma_\omega\frac{1}{\omega}\frac{\partial k}{\partial x_j}\frac{\partial\omega}{\partial x_j} \qquad \text{(C17)}$$

where the constants of the model are computed as $\phi = F_1\phi^{\mathrm{W}} + (1 - F_1)\phi^{\mathrm{K}}$ where F_1 is a blending function and ϕ^{W} and ϕ^{K} the constants for the original k–ω and the k–ε model, respectively. The following standard values for the k–ε model are used

$$\sigma_k^{\mathrm{K}} = 1.0, \quad \sigma_\omega^{\mathrm{K}} = 0.856, \quad \beta^{\mathrm{K}} = 0.0828$$

$$\beta^* = 0.09, \quad \kappa = 0.41, \quad \gamma^{\mathrm{K}} = \beta^{\mathrm{K}}/\beta^* - \sigma_\omega^{\mathrm{K}}\kappa^2/\sqrt{\beta^*}$$

corresponding to the constants $C_{\varepsilon 1} = 1.44$, $C_{\varepsilon 2} = 1.92$ of the k–ε model.

C.4.4. SST k–ω model

Although the original and the new BSL k–ω model perform better in adverse pressure gradient flows than the k–ε model, they still underpredict the amount of separation for severe adverse pressure gradient flows.[109] In an attempt to improve matters, the eddy-viscosity formulation of the BSL model is modified to account for the transport effects of the principal turbulent shear stress. The motivation for this modification comes from the Johnson–King (J–K) model[87] which has proven to be highly successful for adverse pressure gradient flows. The J–K model is based on the assumption that the turbulent shear stress is proportional to the turbulent kinetic energy in the logarithmic and wake regions of a turbulent boundary layer. Johnson and King solve an equation for the maximum turbulent shear stress at each downstream station and limit the eddy viscosity in order to satisfy this proportionality. In the framework of two-equation models, the turbulent kinetic energy is already known and it is therefore only necessary to limit the eddy viscosity to account for the same effect. The resulting model is called shear stress transport (SST) model.

For the SST k–ω model, the constants ϕ^{W} of the BSL model are replaced by the constants ϕ^{S} as follows:

$$\sigma_k^{\mathrm{S}} = 0.85, \quad \sigma_\omega^{\mathrm{S}} = 0.5, \quad \beta^{\mathrm{S}} = 0.0750, \quad \alpha = 0.31,$$

$$\beta^* = 0.09, \quad \kappa = 0.41, \quad \gamma^{\mathrm{S}} = \beta^{\mathrm{S}}/\beta^* - \sigma_\omega^{\mathrm{S}}\kappa^2/\sqrt{\beta^*}$$

where the same convention $\phi = F_1\phi^{\mathrm{S}} + (1 - F_1)\phi^{\mathrm{K}}$ is used and the eddy viscosity is given by

$$v_t = \frac{a_1 k}{\max(\alpha\omega; \Omega F_2)}$$

Ω is the vorticity magnitude and $F_2 = \tanh(\arg_2)$ with $\arg_2 = \max(2\sqrt{k}/0.09\omega y; 500v/y^2\omega)$.

One- and two-equation models can be solved simultaneously with the flow equations using the same numerical algorithm and the same space discretization method. They can also be lagged by one timestep and solved after the mean flowfield is obtained. In this case, the numerical solution of the turbulence model can be obtained with a different scheme than the one used for the mean flow. Numerical tests have shown that simultaneous solution of the turbulence model and the flowfield does not increase the stability and robustness of the overall scheme, at least for subsonic and transonic flow computations. Therefore, for the sake of the flow solver generality it is preferred to keep the one- and two-equation turbulence models separate from the governing equations algorithm. Many modern CFD codes include more than one turbulence model lagged by one time step from the flow algorithm. Various full Reynolds stress models used so far for the computation of simple flows are not considered to be necessary at the present stage for dynamic-stall computations. These models cannot be used as yet for complex unsteady flows because of their mathematical complexity, computational cost and lack of experience in aerodynamic flows.

REFERENCES

1. Anderson, D. A., Tannehill, J. C. and Pletcher, R. H. (1984) *Computational Fluid Mechanics and Heat Transfer*. McGraw-Hill, New York.
2. Arnal, D. (1984) Description and prediction of transition in two-dimensional incompressible flow. AGARD Report 709, Paper No. 2.
3. Baldwin, B. S. and Barth, T. J. (1990) A one-equation turbulence transport model for high Reynolds number wall-bounded flows. NASA TM 102847.
4. Baldwin, B. S. and Lomax, H. (1978) Thin layer approximation and algebraic model for separated turbulent flows. AIAA Paper 78-257.
5. Basu, B. C. and Hancock, G. J. (1978) The unsteady motion of a two-dimensional airfoil in incompressible inviscid flow, *J. Fluid Mech.* **87**, 159–168.
6. Bertoloti, F. P. (1991) Linear and nonlinear stability of boundary layers with streamwise varying properties. Ph.D. thesis, The Ohio State University, Colombus, OH.
7. Beam, R. M. and Warming, R. F. (1978) An implicit factored scheme for the compressible Navier–Stokes equations. *AIAA J.* **16**, 393–401.
8. Bradshaw, P. (1996) Turbulence modeling with application to turbomachinery. *Prog. Aerospace Sci.*, **32**, 575–624.
9. Bradshaw, P., Cebeci, T. and Whitelaw, J. H. (1981) *Engineering Calculation Methods for Turbulent Flows*. Academic Press, New York.
10. Carr, L. W. (1988) Progress in analysis and prediction of dynamic stall, *J. Aircraft* **25** (1), 6–17.
11. Carr, L. W. and Chandrasekhara, M. S. (1996) Compressibility effects on dynamic stall. *Prog. Aerospace Sci.* **32**, 523–573.
12. Carta, F. O. and Lorber, P. F. (1987) Experimental study of the aerodynamics of incipient torsional stall flutter, *J. Propulsion Power* **3** (2), 164–170.
13. Cebeci, T. (1989) Essential ingredients of a method for low Reynolds-number airfoils, *AIAA J.* **27**(5), 1680–1688.
14. Cebeci, T. (ed.) (1990) *Numerical and Physical Aspects of Aerodynamic Flows*, Vol. IV. Springer, Berlin.
15. Cebeci, T. and Bradshaw, P. (1977) *Momentum Transfer in Boundary Layers*. Hemisphere, New York.
16. Cebeci, T. and Carr, L. W. (1983) Calculation of boundary layer near the stagnation point of an oscillating airfoil. NASA TM 8435.
17. Cebeci, T., Chen, H. H., Arnal, D. and Huang, T. T. (1991) Three-dimensional linear stability approach to transition on wings and bodies of revolution, *AIAA J.* **29**(12), 2077–2885.
18. Cebeci, T. and Smith, A. M. O. (1974) *Analysis of Turbulent Boundary Layers*. Academic Press, New York.

19. Cebeci, T., Platzer, M. F., Jang, H. M. and Chen, H. H. (1993) An inviscid-viscous interaction approach for the calculation of dynamic stall initiation of airfoils. *ASME J. Turbomachinery*, **115**(4), 714–723.
20. Chaderjian, N. M. and Schiff, L. B. (1996) Numerical simulation of forced and free-to-roll delta-wing oscillations. *J. Aircraft* **33**(1), 93–99.
21. Chakravarthy, S. R. (1985) Relaxation methods for unfactored implicit upwind schemes. AIAA Paper 84-0165.
22. Chakravarthy, S. R. and Osher, S. (1985) A new class of high accuracy TVD schemes for hyperbolic conservation laws. AIAA Paper 85–0363.
23. Chandrasekhara, M. S., Ahmet, S. and Carr, L. (1990) Schlieren studies of compressibility effects on dynamic stall of airfoils in transient motion. AIAA Paper 90–3038.
24. Chandrasekhara, M. S. and van Dyken, R. D. (1993) LDV measurements in dynamically separated flows, *SPIE Proc. Laser Anemometry Adv. Appl.* **2052**, 305–312.
25. Chang, C. L., Malik, M. R., Erlbacher, M. Y. and Hussailni, M. Y. (1991) Compressible stability of three-dimensional boundary layers using parabolized stability equations. AIAA Paper 91-1636.
26. Chen, K. K. and Thyson, N. A. (1951) Extension of Emmons spot theory to flows on blunt bodies. *AIAA J.* **18**(3), 490–498.
27. Chorin, A. J. (1967) Numerical methods for solving incompressible viscous flow problems. *J. Comput. Phys.* **2**, 12–26.
28. Chorin, A. J. (1968) Numerical solution of the Navier–Stokes equations. *Math. Comput.* **22**, 745–762.
29. Choudhuri, P. G. and Knight, D. D. (1996) Effects of compressibility, pitch rate, and Reynolds number of unsteady incipient leading-edge boundary layer separation over a pitching airfoil. *J. Fluid Mech.* **308**, 195–217.
30. Choudhuri, P. G., Knight, D. D. and Visbal, M. R. (1994) Two-dimensional unsteady leading-edge separation on a pitching airfoil. *AIAA J.*, **32**(4), 673–681.
31. Chyu, W. J. and Davis, S. S. (1981) Numerical studies of unsteady transonic flow over an oscillating airfoil. AGARD-CP-374, Paper No. 3, pp. 1–22.
32. Clarkson, J. D., Ekaterinaris, J. A. and Platzer, M. F. (1993) Computational investigation of airfoil stall flutter. In H. M. Atassi (ed.), *Unsteady Aerodynamics, Aeroacoustics and Aeroelasticity of Turbomachines and Propellers*, pp. 415–432. Springer, Berlin.
33. Choi, D. H. and Kang, D. J. (1991) Calculation of separation bubbles using a partially parabolized Navier–Stokes procedure, *AIAA J.* **29**(8), 1266–1272.
34. Currier, J. and Fung, K. Y. (1991) An analysis of the onset of dynamic stall. AIAA Paper 91-0003.
35. Darzin, P. G. and Reid, W. H. (1981) *Hydrodynamic Stability*. Cambridge Univ. Press, Cambridge.
36. Degani, D. and Schiff, L. B. (1986) Computation of turbulent supersonic flows around pointed bodies having crossflow separation. *J. Comput. Phys.* **66**(1), 173–196.
37. Dhawan, S. and Narasimha, R. (1958) Some properties of boundary layer flow during transition from laminar to turbulent motion. *J. Fluid Mech.* **3**, 418–436.
38. Dindar, M. and Kaynak, U. (1992) Effect of turbulence modeling on dynamic stall of a NACA-0012 Airfoil, AIAA Paper 92–0027.
39. Edwards, J. W. and Thomas, J. L. (1989) Computational methods for unsteady transonic flows, unsteady transonic aerodynamics. In D. Nixon, (ed.), *Progress in Astronautics and Aeronautics*, Vol. 120, pp. 211–261
40. Ekaterinaris, J. A. (1989) Compressible studies on dynamic stall. AIAA Paper 89-0024.
41. Ekaterinaris, J. A. (1995) Numerical investigation of dynamic stall of an oscillating wing. *AIAA J.* **33**(10), 1803–1808.
42. Ekaterinaris, J. A., Chandrasekhara, M.S. and Platzer, M. F. (1995) Analysis of low Reynolds number airfoils. *J. Aircraft* **32**(3), 625–630.
43. Ekaterinaris, J. A., Cricelli, A. S. and Platzer, M. F. (1994) A zonal method for unsteady, viscous, compressible airfoil flows. *J. Fluids Struct.* **8**, 107–123.
44. Ekaterinaris, J. A. and Menter, F. R. (1994) Computation of oscillating airfoil flows with One- and Two-equation turbulence models. *AIAA J.* **32**(12), 2359–2365.
45. Ekaterinaris, J. A. and Platzer, M. F. (1996) Numerical investigation of stall flutter, *ASME J. Turbomachinery* **118**, 197–203.
46. Ekaterinaris, J. A. and Schiff, L. B. (1995) Navier–Stokes solutions for an oscillating double-delta Wing. *J. Aircraft* **32**(2), 228–234.
47. Ekaterinaris, J. A. Sorensen, N. N. and Rasmussen, F. (1997) Numerical investigation of airfoil dynamic stall in simultaneous harmonic oscillatory and translatory motion. *J. Solar Energy Engineering*, **120**, 75–83.
48. Emmons, H. W. (1962) Laminar turbulent transition in a boundary layer. *J. Aerospace Sci.* **18**, 490–498.
49. Ericsson, L. E. and Reding, J. P. (1972) Analytic predictions of dynamic stall characteristics. AIAA Paper 72-0682.
50. Ericsson, L. E. and Reding, J. P. (1976) Dynamic stall analysis in the light of recent numerical and experimental results. *J. Aircraft* **13**(4), 248–255.
51. Ericsson, L. E. and Reding, J. P. (1980) Dynamic stall at high frequency and large amplitude. *J. Aircraft* **17**(3), 136–142.
52. Ericsson, L. E. and Reding, J. P. (1987) Fluid dynamics of unsteady separated flow. Part II. Lifting surfaces, *Prog. Aerospace Sci.* **24**, 249–356.
53. Favier, D., Belleudy, J. and Christian, M. (1992) Influence of coupling incidence and velocity variations on the airfoil dynamic stall. 48th AHS Annual Forum.
54. Filippone, A. (1995) Interaction of potential flow model with the Navier–Stokes equations for rotor aerodynamics. Ph.D. thesis, Denmark Technical Univ., AFM Report 95-07.
55. Fletcher, C. A. J. (1991) *Computational Techniques for Fluid Dynamics*. Springer, Berlin.
56. Freymuth, P. (1988) Propulsive vortical singularities of plunging and pitching airfoils. *AIAA J.* **26**(7), 881–883.
57. Fung, Y. C. (1969) *An Introduction to the Theory of Aeroelasticity*, Dover, New York.

58. Fung, K. Y. and Carr, L. W. (1991) Effects of compressibility on dynamic stall. *AIAA J.* **26**(2), 306–308.
59. Galbraith, R. A. McD, Gracey, M. W. and Gilmur, R. (1992) Collected data for test on a NACA-0012 airfoil, Vol. II: pressure data from oscillatory tests. Dept. of Aerospace Eng. Report 9208, University of Glasgow.
60. Garrick, I. E. (1937) Propulsion of a flapping and oscillating airfoil, NACA Technical Report No. 567.
61. Gangwani, S. T. (1982) Prediction of dynamic stall and unsteady airloads for rotor blades. *J. Amer. Helicopter Soc.* 57–64.
62. Geissler, W. and Sobieczky, H. (1995) Dynamic stall control by variable airfoil Chamber. AGARD-CP-552, Paper No. 6, 1–10.
63. Geissler, W. and Sobieczky, H. (1995) Unsteady-flow control on rotor airfoils. AIAA Paper 95-0189.
64. Ghia, K. N., Yang, J. Oswald, G. A. and Ghia, U. (1991) Study of dynamic stall mechanism using simulation of two-dimensional Navier–Stokes equations. AIAA Paper, 91-0546.
65. Ghia, K. N., Yang, Y., Oswald, G. A. and Ghia, U. (1992) Study of the role of unsteady separation in the formation of dynamic stall vortex. AIAA Paper 92-0196.
66. Giesing, J. P. (1968) Nonlinear two-dimensional unsteady potential flow with lift. *J. Aircraft* **5**(2), 135–143.
67. Godunov, S. K. (1959) A difference scheme for numerical computation of discontinuous solution of Hydrodynamic equations, *Math Spornik* **47**, 271–306. Translated US Joint Publ. Res. Service (1966) JPRS 7226.
68. Gostelow, J. P., Melwani, N. and Walker, G. J. (1996) Effects of streamwise pressure gradient on turbulent spot development. *J. Turbomachinery*, **118**, 737–743.
69. Gormont, R. E. (1973) A mathematical model of unsteady aerodynamics and radial flow for application to helicopter rotors. U.S. Army AMRDL Eustis Directorate Report TR-72-67.
70. Grohsmeyer S. P., Ekaterinaris, J. A. and Platzer, M. F. (1991) Numerical investigation of the effect of leading edge geometry on dynamic stall of airfoils. AIAA Paper 91-1798, 22nd Fluid Dynamic Conf., June 1991.
71. Guruswamy, G. P. (1992) Vortical flow computations of a flexible blended wing-body configuration, *AIAA J.* **30**(10), 2497–2503.
72. Hancock, G. J. and Mabey, D. G. (1990) Unsteady aerodynamics of controls. AGARD-CP-465.
73. Harlow, F. H. and Welch, J. E. (1985) Numerical calculation of Time-dependent viscous incompressible flow with free surface, *Phys. Fluids* **8**, 2182–2189.
74. Harris, F. D., Tarzanin, F. J. and Fisher, R. K., Jr (1970) Rotor high-speed performance; theory vs. test. *J. Amer. Helicopter Soc.* **15**(3), 35–44.
75. Herbert, Th. (1991) Boundary-layer transition analysis and prediction revisited. AIAA Paper 91-0737.
76. Herbert, Th. (1997) Parabolized stability equations. *Ann. Rev. Fluid Mech.* **29**, 245–283.
77. Herbert, Th. and Bertoloti, F. P. (1990) Stability analysis of nonparallel boundary layers. Bull. Am. Phys. Soc. **32**, 2079–2080.
78. Herbert, Th., Stuckert, G. K. and Esfahanian, V. (1993) Effects of free-stream turbulence on boundary-layer transition. AIAA Paper 93-0488.
79. Hess J. L. and Smith A. M. O. (1966) Calculation of potential flow about arbitrary bodies. *Prog. Aerospace Sci.* **8**.
80. Hirsch, C. (1991) *Numerical Computation of Internal and External Flows*, Vols I and II. Wiley, New York.
81. Hixon, R. and Sankar, L. N. (1992) Application of a generalized minimal residual method to 2D unsteady flows. AIAA Paper 92-0422.
82. Iyer, V., Spall, R. and Dagenhart, J. R. (1994) Computational study of transition front on a swept wing leading edge. *J. Aircraft* **31**(1), 72–78.
83. Jameson, A., Schmidt, W. and Turkel, E. (1981) Numerical solutions of the Euler equations by finite volume methods using Runge–Kutta time stepping schemes. AIAA Paper 81-1259.
84. Jameson, A. and Venkatakrishnan, V. (1985) Transonic flows about oscillating airfoils using the Euler equations. AIAA Paper 85-1514.
85. Jang, H. M. (1990) A viscous-inviscid interaction method for unsteady flows. Ph.D. Thesis, University of Michigan.
86. Johnson, D. A. (1992) Nonequilibrium algebraic turbulence model considerations for transonic airfoils and wings. AIAA Paper 92-0439.
87. Johnson, D. A. and King, L. S. (1985) A mathematically simple turbulence closure model for attached and separated turbulent boundary layers, *AIAA J.* **23**, 1684–1692.
88. Jones, K. D., Dohring, C. M. and Platzer, M. F. (1996) Wake structures behind plunging air foils. AIAI Paper 96-0078.
89. Jones, K. D. and Platzer, M. F. (1997) A fast method for the prediction of dynamic stall onset on turbomachinery blades, ASME Paper 97-GT-101.
90. Jones, W. P. and Launder B. E. (1973) The calculation of low-reynolds-number-phenomena with a two-equation model of turbulence. *Int. J. Heat Mass Transfer* **16**, 1119–1130.
91. von Karman, T. and Burgers, J. M. (1934) General aerodynamic theory perfect fluids, In W. F. Durand (Ed.), Aerodynamic Theory, Vol. II, p. 308.
92. Kim, J. and Moin, P. (1985) Application of a fractional time-step method to incompressible Navier–Stokes equations. *J. Comput. Phys.* **59**, 308–323.
93. Kim, M. J. and Mook, D. T. (1986) Application of continuous vorticity panels to general unsteady incompressible two-dimensional lifting flows. *J. Aircraft* **23**(6), 464–471.
94. Ko, S. and McCroskey, W. J. (1995) Computations of unsteady separating flows over an oscillating airfoil. AIAA Paper 95-0312.
95. Landon, R. H. (1982) NACA-0012 oscillatory and transient pitching, AGARD Report 702.
96. Leishman, J. G. and Beddoes, T. S. (1989) A semi-empirical model for dynamic stall. *J. Amer. Helicopter Soc.* **34**(3).
97. Lin, C. C. (1955) *Theory of Hydrodynamic Stability*. Cambridge Univ. Press, Cambridge.
98. Lorber, P. F. (1992) Compressibility effects on the dynamic stall of a three-dimensional wing, AIAA Paper 92–0191.

99. Lorber, P. F. and Carta, F. O. (1988) Airfoil dynamic stall at constant pitch rate and high Reynolds Number, *Journal of Aircraft*, **25** (3), 548–556.
100. Lorber, P. F., Carta, F. O. and Covino, A. F. (1992) An oscillating three-dimensional wing experiment: compressibility, sweep, rate, waveform and geometry effects on unsteady separation and dynamic stall, UTRC Report R92-958325-6, November 1992 and AIAA Paper 91-1795, June 1991.
101. Mabey, D. G. (1989) Physical phenomena associated with unsteady flow, unsteady transonic aerodynamics. In D. Nixon, (Ed.), *Progress in Astronautics and Aeronautics*, Vol. 120, pp. 1–55.
102. MacCormack, R. W. (1985) Current status of numerical solutions of the Navier–Stokes equations, AIAA Paper 85-0032.
103. McCroskey, W. J. (1981) The phenomenon of dynamic stall. NASA TM-81264.
104. Mack, L. M. (1984) Boundary layer stability theory. AGARD Report No. 709.
105. Malik, M. R. (1982) COSAL—A black-box compressible stability analysis code for transition prediction in three-dimensional boundary layers. NASA CR-165925.
106. Malkiel, E. and Mayle, R. E. (1996) Transition in a separation bubble. *J. Turbomachinery* **118**, 752–759.
107. Mehta, U. B. (1977) Dynamics stall of an oscillating airfoil, AGARD CP 227, Paper No. 23, 1–32.
108. Menter, F. R. (1992) Performance of popular turbulence models for attached and separated adverse pressure gradient flows. *AIAA J*. **30**(8), 2066–2072.
109. Menter, F. R. (1993) Zonal two equation k–ω turbulence models for aerodynamic flows, AIAA Paper 93-2906.
110. Merkle, C. L. and Athavale, M. (1987) Time-accurate unsteady incompressible flow algorithm based on artificial compressibility. AIAA Paper 87-1137.
111. Michel, R. (1957) Etude de la Transition sur les Profiles d'aile; Establissement d'un Critere de Determination de Point de Transition et Calcul de la Trainee du Profile Incompressible. ONERA Rept. 1/1578A.
112. Miles, J. W. (1949) Quasi-stationary thin airfoil theory. *J. Aeronaut. Sci.* **16**(3).
113. Morkovin, M. V. (1978) Instability transition to turbulence and predictability. AGAR-Dograph No. 236.
114. Morkovin, M. V. (1983) Understanding transition to turbulence in shear layers. Report AFOSR-FR-83, Illinois Institute of Technology, Chicago, IL.
115. Munk, M. M. (1922) General theory of thin wing sections, NACA Report No. 142.
116. Newsome, R. W. (1994) Navier–Stokes simulation of wing-tip and wing-juncture interaction for a pitching wing. AIAA Paper, 94-2259.
117. Okong'o, N. and Knight, D. D. (1997) implicit unstructured Navier–Stokes simulations of leading edge separation over a pitching airfoil. AIAA paper 97–0657.
118. Osher, S. and Solomon, F. (1982) Upwind difference schemes for hyperbolic systems of conservation laws. *Math. Comput*. **38**(158), 339–374.
119. Patterson, M. T. and Lorber, P. F. (1990) Computational and experimental studies of compressible dynamic stall. *J. Fluids Struct*. **4**, 259–285.
120. Piziali, R. A. (1993) An experimental investigation of 2D and 3D oscillating wing aerodynamics for a range of angle of attack including stall. NASA Technical Memorandum 4632.
121. Rai, M. M. (1989) Unsteady three-dimensional Navier–Stokes simulations of turbine rotor-stator interaction, Part I–Methodology, Part II–Results. *J. Propulsion Power*, **5**(3), 307–319.
122. Rai, M. M. and Moin, P. (1991) Direct numerical simulation of transition and turbulence in spatially evolving boundary layers. AIAA Paper 91-1607.
123. Reed, H. L, Saric W. S. and Arnal, D. (1996) Linear stability theory applied to boundary layers. *Ann. Rev. Fluid Mech.* **28**, 389–428.
124. Reisenthal, P. H. (1995) Further results on the Reynolds number scaling of incipient leading edge stall. AIAA Paper 95-0780.
125. Reshotko, E. (1976) Boundary layer stability and transition. *Ann. Rev. Fluid Mech.* **8**, 311–349.
126. Reu, T. and Ying, S. X. (1992) Hybrid grid approach to study dynamic stall. *AIAA J*. **30**(11), 2670–2676.
127. Riester, P. J. (1993) A computational and experimental investigation of incompressible oscillatory airfoil flow and flutter problems. M.S. thesis, Naval Postgraduate School, Monterey, CA.
128. Rizetta D. P. and Visbal, M. R. (1993) Comparative numerical study of two turbulence models for airfoil static and dynamic stall. *AIAA J*. **31**, 784–786.
129. Roe, P. L. (1981) Approximate Riemann solvers, parameter vectors, and difference schemes. *J. Comput. Phys.* **43**, 357–372.
130. Rogers, S. E. and Kwak, D. (1988) An upwind difference scheme for time–accurate incompressible Navier–Stokes equations. AIAA Paper 88–2883.
131. Rogers, S. E., Kwak, D. and Kiris, C. (1991) Steady and unsteady solutions of the incompressible Navier–Stokes equations. *AIAA J*. **29**(4), 603–610.
132. Rumsey, C. L. and Anderson, W. K. (1988) Some numerical and physical aspects of unsteady Navier–Stokes computations over airfoils using dynamics meshes. AIAA Paper 88-0329.
133. Salari, K. and Roache, P. J. (1990) The influence of sweep on dynamic stall produced by a rapidly pitching wing. AIAA Paper 90–0581.
134. Sankar, L. N. and Tassa, W. (1981) Compressibility effects of dynamic stall of a NACA-0012 airfoil. *AIAA J*. **19**(5), 557–568.
135. Sankar, L. N. and Tung, W. (1985) Numerical solution of unsteady viscous flow past rotor sections. AIAA Paper 85-0129.
136. Sanz, W. and Platzer, M. F. (1995) On the Navier–Stokes calculation of separation bubbles with a new transition model. International Gas Turbine Congress, ASME Paper 96-GT-487.
137. Schlichting, H. (1979) *Boundary Layer Theory*, pp. 459–465. McGraw-Hill, New York.
138. Smilg, B. (1949) The instability of pitching oscillations of an airfoil in subsonic incompressible potential flow. *J. Aeronaut. Sci.* **16** (11).
139. Solomon, W. J., Walker, G. J. and Gostelow, J. P. (1996) Transition length prediction for flows with rapidly changing pressure gradients. *J. Turbomachinery* **118**, 744–751.

140. Spalart P. R. and Allmaras, S. R. (1992) A one-equation turbulence model for aerodynamic flows. AIAA Paper 92-0439.
141. Spall, R. and Malik, M. R. (1992) Linear stability of three-dimensional boundary layers over axisymmetric bodies at incidence. *AIAA J*. **30**(4), 905–913.
142. Srinivasan, G. R., Beader, J. D., Obayashi, S. and McCroskey, W. J. (1992) Flowfield of a lifting rotor in Hover: a Navier–Stokes simulation, *AIAA J*. **30**(10), 2371–2378.
143. Srinivasan, G. R., Ekaterinaris, J. A. and McCroskey, W. J. (1995) Dynamic stall of an oscillating wing, Part 1: evaluation of turbulence models. *Comput. Fluids* **24**(7), 833–861.
144. Steger, J. L. and Warming, R. F. (1981) Flux vector splitting of the inviscid gas dynamic equations with applications to finite-difference methods. *J. Comput. Phys.* **40**, 263–293.
145. Summa, J., Strash, D. and Yoo, S. (1992) Zonal flow analysis method for two-dimensional airfoils. *AIAA Journal*, **30**(2), 548–549.
146. Teng N. H. (1987) The development of a computer code for the numerical solution of unsteady inviscid incompressible flow over an airfoil. M.S. thesis, Naval Postgraduate School.
147. Tran, C. T. and Petot, D. (1981) Semi-empirical model for the dynamic stall of airfoils in view of the application to the calculation of responses of a helicopter blade in forward flight. *Vartica*, Vol. 5, No. 1, 35–53.
148. Tulapurkara, E. G. (1996) Turbulence models for the computation of flows past airplanes. *Prog. Aerospace Sci.* **28**, 1–95.
149. Tuncer, I. C, Wu, J. C. and Wang, C. M. (1990) Theoretical and numerical studies of oscillating airfoils, *AIAA J*., **28**(9), 1615–1624.
150. Tuncer, I. H., Ekaterinaris, J. A. and Platzer, M. F. (1995) Viscous–inviscid interaction method for unsteady low-speed airfoil flows. *AIAA J*. **33**(1), 151–154.
151. Turner, M. A. (1994) Computational investigation of Wake-induced airfoil flutter in incompressible flow and active flutter control. M.S. thesis, Naval Postgraduate School, Monterey, CA.
152. Tyler, J. C. and Leishman, J. G. (1992) Analysis of pitch and plunge effects on unsteady airfoil behavior, *J. Amer. Helicopter Soc.* 69–83.
153. Van Dyken, R. D. and Chandrasekhara, M. S. (1992) Leading-edge velocity field of an oscillating airfoil in compressible dynamic stall. AIAA Paper 92-0193.
154. Van Dyken, R. D., Ekaterinaris, J. A., Chandrasekhara, M. S. and Platzer, M. F. (1996) Analysis of compressible light dynamic stall flow at transitional reynolds numbers, *AIAA J*. **34**(7), 1420–1427.
155. Veldman, A. E. P. (1981) A new, quasi-simultaneous method to calculate interacting boundary layers. *AIAA J*. **19**(1), 79–85.
156. Venkatakrishnan, V. and Mavriplis, D. J. (1996) *J. Comput. Phys.* **127**, 380–397.
157. Visbal, M. R. (1988) Effect of compressibility on dynamic stall of a pitching airfoil. AIAA Paper 88-0132.
158. Visbal, M. R. and Shang, J. S. (1989) Investigation of the flow structure around a rapidly pitching airfoil. *AIAA J*. **27**(8), 1044–1055.
159. Wang, C. M. (1995) Numerical vorticity confinement for vortex solid body interaction problems. *AIAA J*., **33**(8), 1447–1453.
160. Warren, E. S., Harris, J. E. and Hassan, H. A. (1995) Transition model for high speed flow. *AIAA J*. **33**(8), 1391–1397.
161. White, F. M. (1974) *Viscous Fluid Flow*. McGraw-Hill, New York.
162. Wilcox, D. C. (1988) Reassessment of the scale-determining equation for advanced turbulence models. *AIAA J*. **26**(11), 1299–1310.
163. Wilcox, D. C. (1993) *Turbulence Modeling for CFD*. DCW Industries Inc.
164. Wu, J. C. (1980) Theory of aerodynamic force and moment in viscous flows. AIAA Paper 80-0011.
165. Wu, J. C. (1984) Fundamental solutions and numerical methods for flow problems. *Int. J. Numer. Methods Fluids* **4**, 185–201.
166. Wu, J. C. and Sankar, N. L. (1989) Evaluation of three turbulence models for the prediction of steady and unsteady airloads. AIAA Paper 89-0609.
167. Wu, J. C., Wang, C. M. and Gulcat, U. (1984) Zonal solution of unsteady viscous flow problems. AIAA Paper 84-1637.
168. Wu, J. C., Wang., C. M. and Tuncer, I. C. (1986) Unsteady aerodynamics of rapidly pitching airfoils. AIAA Paper 86-1105.
169. Yakhot, V. and Orzag, S. A. (1986) Renormalization group analysis of turbulence. 1—basic theory. *J. Scientific Comput.* **1**, 1–36.
170. Yang, H. Q. and Przekwas, A. J. (1993) Dynamic stall on a three-dimensional rectangular wing. AIAA Paper 93-0637.
171. Yao, Z. X., Garcia-Fogeda, P., Liu, D. D. and Shen, G. (1989) Vortex/wake flow studies for airfoils in unsteady motions. AIAA Paper 89-2225.
172. Young, T. W., Warren, E. S., Harris, J. E. and Hassan, H. A. (1993) A new approach for the calculation of transitional flows, *AIAA J*. **31**(4), 629–636.